

This is to certify that the
dissertation entitled

AN ACOUSTIC INTENSITY-BASED METHOD AND ITS
AEROACOUSTIC APPLICATIONS

presented by

CHAO YU

has been accepted towards fulfillment
of the requirements for the

Ph.D. degree in MECHANICAL ENGINEERING



Major Professor's Signature

26 November 2008

Date

**AN ACOUSTIC INTENSITY-BASED METHOD AND ITS AEROACOUSTIC
APPLICATIONS**

By

Chao Yu

A DISSERTATION

**Submitted to
Michigan State University
in partial fulfillment of the requirements
for the degree of**

DOCTOR OF PHILOSOPHY

Mechanical Engineering

2008

ABSTRACT

AN ACOUSTIC INTENSITY-BASED METHOD AND ITS AEROACOUSTIC APPLICATIONS

By

Chao Yu

Aircraft noise prediction and control is one of the most urgent and challenging tasks worldwide. A hybrid approach is usually considered for predicting the aerodynamic noise. The approach separates the field into aerodynamic source and acoustic propagation regions. Conventional CFD solvers are typically used to evaluate the flow field in the source region. Once the sound source is predicted, the linearized Euler Equations (LEE) can be used to extend the near-field CFD solution to the mid-field acoustic radiation. However, the far-field extension is very time consuming and always prohibited by the excessive computer memory requirements. The FW-H method, instead, predicts the far-field radiation using the flow-field quantities on a closed control surface (that encloses the entire aerodynamic source region) if the wave equation is assumed outside. The surface integration, however, has to be carried out for each far-field location. This would be still computationally intensive for a practical 3D problem even though the intensity in terms of the CPU time has been much decreased compared with that required by the LEE methods. For an accurate far-field prediction, the other difficulty of using the FW-H method is that the complete control surface may be infeasible to accomplish for most practical applications.

Motivated by the need for the accurate and efficient far-field prediction techniques, an Acoustic Intensity-Based Method (AIBM) has been developed based on an acoustic input from an OPEN control surface. The AIBM assumes that the sound propagation is governed by the modified Helmholtz equation on and outside a control surface that encloses all the nonlinear effects and noise sources. The prediction of the acoustic radiation field is carried out by the inverse method with an input of acoustic pressure derivative and its simultaneous,

co-located acoustic pressure. The reconstructed acoustic radiation field using the AIBM is unique due to the unique continuation theory of elliptic equations. Hence the AIBM is more stable and the reconstructed acoustic pressure is less dependent on the locations of the input acoustic data. The solution of the modified Helmholtz equation in the frequency domain is approximated by finite linear combination of basis functions. The coefficients associated with the basis functions are obtained by matching the assumed general solution to the given input data over an open control surface. The details on the optimization method, the instability issue and the numerical implementation of the AIBM have been discussed in the dissertation.

To verify the AIBM model, several acoustic radiation examples are solved, e.g. multiple sources radiation. The analytical acoustic pressure and its normal derivative on a partial spherical control surface are used as the input for the AIBM. The reconstructed acoustic field is obtained then compared with the analytical acoustic field. Excellent agreement is achieved and demonstrated. Some affecting factors on the AIBM, e.g. input locations and the signal-to-noise ratio, are also investigated. In addition, the potential of AIBM in broadband noise prediction is examined in vortex/trailing edge interaction problem. Furthermore, a series of real world model problems are chosen to demonstrate the capability and potential of AIBM in CAA applications. Two important aircraft noises: turbofan noise and airframe noise, are studied in detail. Both the permeable surface FW-H equation method and the AIBM are used to evaluate the radiated field. The prediction results obtained from the AIBM and the FW-H integral method are compared with the solution from the CFD/CAA method. The accuracy and efficiency of both the AIBM and the FW-H integral method are analyzed.

In summary, the “open surface” AIBM makes up the drawbacks of traditional “closed surface” approaches. It provides an effective alternative for the far-field acoustic prediction of practical aeroacoustic problems.

Acknowledgments

I would like to express my gratitude to my advisers Prof. Zhuang, for all good advices and encouragement during the work and Prof. Zhou, for sharing his great mathematics knowledge and leading causes in my dissertation.

I am grateful for Prof. Radcliffe, Prof. Wright and Prof. Jaber, who not only gave me advice, but also kept track of all the details of my research work. I want to acknowledge their help for serving as my dissertation defense committee and their time in reviewing my dissertation.

Many thanks to Prof. Thiele from TU-Berlin, Berlin, Germany for providing me the research collaboration opportunity with the scientists and specialists worldwide.

I would also like to thank Prof. Li of Beihang University (BUAA), Beijing, China for giving me valuable advice and discussions on aeroacoustic inverse problems and Mr. Lin of BUAA for his assistance on CAA solutions of the duct intake problem.

Also I want to thank my colleagues in the Computational Fluid Dynamics Research Laboratory for creating a stimulating working atmosphere.

Finally, I would like to acknowledge the financial support of this work from the National Science Foundation (NSF-ITR-0325760), TU-Berlin Research Scientist Grant (IP-10022152) and Graduate Office Fellowship.

Contents

List of Tables	vi
List of Figures	vii
Nomenclature	x
1 Introduction	1
1.1 Traditional Techniques for Noise Prediction	2
1.1.1 Numerical Simulation Methods	2
1.1.2 Acoustic Analogy	4
1.1.3 Aeroacoustic Hybrid Prediction Methods	4
1.1.4 Inverse Acoustic Methods	5
1.2 Acoustic Intensity-Based Method (AIBM)	7
1.3 Organization of the Dissertation	8
2 Aeroacoustic Governing Equations	10
2.1 Introduction	10
2.2 Wave Equation	10
2.3 Helmholtz Equation	14
3 Acoustic Intensity-Based Method for Acoustic Far-Field Prediction	15
3.1 Introduction	15
3.2 Mathematical and Numerical Formulations	16
3.2.1 Mathematical Formulation	16
3.2.2 Numerical Formulation	19
3.2.3 Numerical Implementation	20
3.3 Numerical Results and Discussions	23
3.3.1 Verification and Advantages of AIBM	23
3.3.2 Effect of Signal-to-Noise Ratio (SNR)	27
3.3.3 Application to Multi-Frequency Acoustic Radiation Problem	35
4 2D AIBM with Subsonic Mean Flow	44
4.1 Introduction	44
4.2 Mathematical Formulations	45
4.2.1 A Single Frequency	45
4.2.2 Multiple Frequencies	51

4.3	Numerical Examples and Discussions	54
4.3.1	Monopole in a Uniform Flow	54
4.3.2	Sound Radiation by a Flow Around a NACA Airfoil	59
4.3.3	Sound Scattering	63
5	3D AIBM with Subsonic Mean Flow	72
5.1	Introduction	72
5.2	Mathematical Formulations	73
5.2.1	Basic Formulation for AIBM	73
5.2.2	Improved Formulation for AIBM	74
5.2.3	Simplified 2.5D Formulation for AIBM	75
5.2.4	Numerical Implementation	76
5.3	Results and Discussions	77
5.3.1	Multiple Sources in a Uniform Flow	77
5.3.2	Acoustic Scattering	83
5.3.3	Acoustic Radiation from an Axisymmetric Duct Intake	87
6	Conclusions	97
6.1	Conclusion	97
6.2	Suggestions for Future Work	99
	Appendix A: Associated Legendre Polynomial	101
	Appendix B: Spherical Hankel Function	103
	Bibliography	104

List of Tables

- 3.1 The strengths and distributions of the 2D acoustic sources 26
- 5.1 The strengths and distributions of the 3D acoustic sources 79

List of Figures

3.1	Acoustic radiation field with input acoustic data locations.	18
3.2	Schematic diagram of acoustic sources and each input segment's location. . .	25
3.3	Comparisons of reconstructed acoustic radiation pressure with analytical solution at $r = 50\text{m}$ for different γ	28
3.4	Effects of SNRs on reconstructed acoustic radiation pressure at $r = 10\text{m}$. . .	32
3.5	Comparisons of reconstructed acoustic radiation pressure $P(r, \theta)$ contours for SNR=100 with analytical solution.	33
3.6	Schematic diagram of 2D vortex filament moving around the edge of a semi-infinite plane and input acoustic data points on specified segments. . .	37
3.7	Spectrum of acoustic radiation pressure time history of 2D vortex model at $r = 75\text{m}$, $\theta = \pi/4$, $M_a = 0.01$ and $d = 1\text{m}$	39
3.8	Acoustic radiation pressure and directivity calculated from the input data with frequency range of 0.05 - 0.2Hz.	40
3.9	Acoustic radiation pressure and directivity calculated from the input data with frequency range of 0.05 - 0.45Hz.	41
3.10	Acoustic radiation pressure and directivity calculated from the input data with frequency range of 0.05 - 1.45Hz.	42
3.11	Acoustic radiation pressure time history ($r = 100\text{m}$, $\theta = \pi/5$).	43
4.1	Schematic diagram of sound propagation field and locations of acoustic measurements.	47
4.2	Schematic diagram of a monopole radiation in a uniform flow and locations of acoustic measurements.	56
4.3	Far-field directivity ($r = 100\text{m}$) comparison of a monopole radiation in a $M_a = 0.5$ flow.	57
4.4	Pressure contours of a monopole radiation in a $M_a = 0.5$ flow.	58

4.5	Instantaneous pressure perturbations of the flow around the NACA 0018 airfoil along with the location of the FW-H surface.	60
4.6	Far-field directivity ($r = 100\text{m}$) of the flow around the NACA 0018 airfoil.	61
4.7	Pressure contours of the sound propagation generated by the flow around the NACA 0018 airfoil.	62
4.8	Schematic diagram of the sound scattering by a cylinder.	64
4.9	Frequency spectrum for the sound scattering, $r = 6.125$	65
4.10	Pressure time history reconstruction with different frequency range at $r = 7.25$ and $\theta = 0^\circ$	66
4.11	Pressure time history reconstruction with different frequency range at $r = 7.25$ and $\theta = 90^\circ$	67
4.12	Pressure time history reconstruction with different frequency range at $r = 7.25$ and $\theta = 180^\circ$	68
4.13	Instantaneous pressure contours of the sound scattering at $t=15$: CAA (top), AIBM (bottom).	69
4.14	Instantaneous pressure contours of the sound scattering at $t=11$: CAA (top), AIBM (bottom).	70
4.15	Instantaneous pressure contours of the sound scattering at $t=9$: CAA (top), AIBM (bottom).	71
5.1	Schematic diagram of multiple sources in a uniform flow.	78
5.2	Comparisons of the predicted pressure solutions with the analytical solutions: along x-axis (top), along y-axis(bottom).	81
5.3	3D instantaneous pressure contours for the sound radiation of multiple sources: Analytical (top), AIBM (bottom).	82
5.4	Schematic diagram of acoustic scattering by a sphere.	84
5.5	Instantaneous pressure contours of the sound scattering in the plane $y = 0$: CAA (top), AIBM (bottom).	85
5.6	Comparisons of the predicted pressure solutions with the CAA solutions: along x-axis (top), along y-axis (bottom).	86
5.7	Schematic diagram of acoustic radiation through an axisymmetric duct intake.	89

5.8	A comparison of the directivity along the x-direction with $z = 6.5\text{m}$ and $y = 0$ for the duct mode of $m=2$ and $n=1$	90
5.9	Instantaneous pressure contours in the plane $\theta = 0$ for the duct mode of $m=2$ and $n=1$: CAA (top), AIBM (bottom).	92
5.10	Pressure amplitude contours in the plane $\theta = 0$ for the duct mode of $m=3$ and $n=1$: CAA (top), AIBM (bottom).	93
5.11	Comparison of the predicted pressure solution with the CAA solution at $z = 15\text{m}$ and $y = 0$ for the duct mode of $m = 2$ and $n = 1$	94
5.12	Comparison of the predicted directivity with the CAA solution at $z = 15\text{m}$ and $y = 0$ for the duct mode of $m = 3$ and $n = 1$	95
5.13	3D reconstructed pressure contours for the duct mode of $m=4$ and $n=1$: CAA (top), AIBM (bottom).	96

Images in this dissertation are presented in color

Nomenclature

A_0	Acoustic source strength
c	Speed of sound
G_n	n -th order generalized Hankel function of the second kind
H_n	n -th order Hankel function of the second kind
i	$\sqrt{-1}$
\mathbf{i}	Unit vector in x direction
k	Wave number, ω/c
M	Number of measurements (inputs)
M_a	Mach number
(m, n)	Dust acoustic mode
\mathbf{n}	Unit normal vector, (n_x, n_y, n_z)
N	Terms of approximation in the asymptotic formulations
p	Acoustic pressure in the time domain
p_j	Acoustic pressure from a monopole sound source
P	Acoustic pressure in the frequency domain
P_e	Exact acoustic pressure in the frequency domain
P_N	Approximated acoustic pressure in the frequency domain
P_n^m	Associated Legendre polynomial
r, θ	Polar coordinates
r, θ, ϕ	Spherical coordinates
$\hat{r}, \hat{\theta}$	Modified polar coordinates
$\hat{r}, \hat{\theta}, \hat{\phi}$	Modified spherical coordinates

r_c	Radius of the control surface (minimum sphere)
RN	Random noise, or random pressure perturbation
s	Entropy
\mathbf{u}	Unsteady velocity vector
\mathbf{U}	Free-stream velocity vector, (U, V, W)
U_m	Maximum speed of the vortex motion
\mathbf{x}	Cartesian coordinates associated with observation point, (x, y, z)
$\hat{\mathbf{x}}$	Modified Cartesian coordinates, $(\hat{x}, \hat{y}, \hat{z})$
t	Time associated with the arrival of sound wave at observation point

Greek

α	Shifted angle
β	$\sqrt{1 - M_a^2}$
γ	Angle between the two measurement segments
Γ	Spherical boundary containing all the acoustic sources
Γ_1	Part of Γ
Φ	Velocity potential function
ρ	Density
ω	Angular frequency

Mathematics

\cdot	Dot product or scalar product
∇^2	Laplacian operator

Superscripts

'	Fluctuating quantities
---	------------------------

Subscripts

0	Value of quantity in steady free stream
---	---

Chapter 1 Introduction

As one of the most important pollutions, aircraft noise draws intensive attention worldwide. As early as the 1970s, the United States has issued the Federal Aviation Regulation (FAR) Part 36 Noise Standards [1] to limit the transportation aircraft noise. From then on, noise level has been one of the crucial guidelines on navigability. In the 1990s, the International Civil Aviation Organization (ICAO) announced more stringent Noise Standards for Aircraft Type Certification (NSATC) [2], which further spurred the “green aircraft” development initiated by the National Aeronautics and Space Administration (NASA) and the aircraft manufacturers.

In the 1970s, NASA commenced the Aircraft Noise Prediction Program (ANOPP) [3] and conducted more than ten years of study on new technology and comprehensive prediction methods for aircraft noise. In 1992, NASA, in partnership with Federal Aviation Administration (FAA) and the U.S. industry giants Boeing, Pratt & Whitney and GE, developed the Advanced Subsonic Technology (AST) program [4] on both airframe and engine noise reduction. The initial goal was to achieve 10 dB reductions in each flight phase: take-off, sideline, and approach in 20 years, relative to 1992’s technology. Soon after, in 1997, NASA further raised the three pillar noise stretch goals, which are reducing the perceived noise level of future aircraft by 10 dB in ten years and 25 dB in 20 years relative to 1997. In Europe, similar research is also expanded around aircraft noise supported by European Union and European industry companies (Airbus, Roll-Royce etc.), e.g. TurboNoiseCFD program aimed at jet engine noise, and the RAIN program on airframe noise [5].

Despite significant progress having been made in reducing aircraft noise over the past decade, further improvements are required because of increasing community noise expo-

sure caused by the growth in aircraft fleet. To develop low noise aircraft and control the noise at the design stage, developing accurate and efficient noise prediction tools is undoubtedly important. In this chapter, the traditional computational techniques for aerodynamic noise prediction and underlying theories are briefly reviewed. Then, a new advanced method, Acoustic Intensity-Based Method (AIBM), is introduced and afforded particular attention. Finally, the structure of the dissertation is outlined.

1.1 Traditional Techniques for Noise Prediction

Half a century ago, Lighthill [6] first proposed the “aerodynamic noise” concept in his research on quiet jet engines. His Lighthill acoustic analogy also became the foundation of aeroacoustics. Nowadays varieties of techniques have been developed to predict aerodynamic noise either theoretically or numerically. In this section, four important methodologies are presented and reviewed. These are numerical simulation techniques, i.e. Computational Fluid Dynamics (CFD) and Computational Aeroacoustics (CAA), acoustic analogy methods, aeroacoustic hybrid techniques, which combines the advantages of numerical methods and acoustic analogy methods, and inverse acoustic methods.

1.1.1 Numerical Simulation Methods

In this section, three most commonly used CFD and CAA techniques for aerodynamic noise simulation have been reviewed.

Direct numerical simulation (DNS) is a simulation in CFD in which the Navier-Stokes equations are numerically solved without any turbulence model [7]. DNS resolves the whole range of spacial and temporal flow scales from the smallest dissipative scales to the largest integral scale. Therefore, the computational cost of DNS is very high, even at low

Reynolds numbers. For the Reynolds numbers encountered in most industrial applications, the computational resources required by a DNS would exceed the capacity of the most powerful computers currently available. However, DNS is a useful tool in fundamental research in turbulence. It provides a standard tool for evaluating different acoustic prediction model [8].

Unsteady Reynolds-averaged Navier-Stokes (RANS) equations are a set of time-averaged equations, which are derived from Navier-Stokes equations, dealing with turbulent flows. These equations can be used to provide approximate averaged solutions to the Navier-Stokes equations. In aerodynamic noise simulation, RANS can simulate the noise of the largest flow features. However RANS suppresses the acoustic field and under predicts dynamic loads [9].

Another alternative computational technique, Large-eddy simulation (LES), resolves only the dynamically important flow scales and models the effects of small scales using a sub-grid scale (SGS) model. LES requires less computational effort than DNS but more effort than RANS. The main advantage of LES over computationally cheaper RANS approaches is the increased level of detail it can deliver. While RANS methods provide "averaged" results, LES is able to predict instantaneous flow characteristics and resolve turbulent flow structures. LES is a suitable compromise of DNS and RANS in accuracy and cost.

Generally these numerical simulation techniques, DNS, RANS and LES methods offer attractive alternatives. But they are not always affordable even with today's high-performance computers and parallel computing technology. Hybrid approaches are usually considered for predicting aerodynamic noise, in which the field is divided into aerodynamic source and acoustic propagation regions. For example, LES/FW-H and RANS/FW-H hybrid methods.

1.1.2 Acoustic Analogy

In 1952, the famous Lighthill theory [6] of sound generation by turbulence was brought forward and soon became the birthstone of aeroacoustics. Lighthill's equation was accurately derived from compressible Navier-Stokes equations without any assumptions. With the "analogy" idea of representing a complicated fluid mechanical process that acts as an acoustic source by an acoustically equivalent source term [10], the Navier-Stokes equations have been rearranged into the form of an inhomogeneous wave equation. Within this equation, all the noise effects on the right hand were described as noise source terms including pressure and velocity fluctuation as well as stress tensor and force terms.

Lighthill's equation is limited to radiation in free space when it was first developed. In 1955, Curle [11] expanded a more general equation based on Lighthill's analogy using Kirchhoff method. The Curle equation takes still solid boundary effects into consideration. In 1969, Ffowcs Williams and Hawkings [12] further expanded Curle equation introducing general functions and developed FW-H equation. FW-H equation is valid for aeroacoustic sources in a relative motion with respect to a solid surface. Nowadays, FW-H equation is known as an effective acoustic far-field prediction method, in which Farassat's Formulation 1A [13–15] is commonly used.

1.1.3 Aeroacoustic Hybrid Prediction Methods

The hybrid prediction technique based on CFD and FW-H with penetrable surface has advanced considerably. And much experience has been gained in its use. The technique separates the field into aerodynamic source and acoustic propagation regions. Conventional CFD solvers are typically used to evaluate the flow-field solution in the near field to provide the aerodynamic sound source. Once the sound source is predicted, the linearized

Euler Equations (LEE) or the integral methods based on Lighthill's analogy [6] are used for the prediction of the acoustic wave propagation. The LEE methods assume the flow field to be a time-averaged mean flow and a time-dependent small disturbance. The extension of the near field CFD solution to the mid-field acoustic radiation can be achieved using the LEE methods. However, the evaluation of the far-field radiation is prohibited by excessive computer memory requirements. The integral methods (i.e. Kirchhoff method [16] or permeable surface FW-H equation method [12]), instead, predict the far-field radiating sound using the flow field quantities on a closed control surface (that encloses the entire aerodynamic source region) if the wave equation is assumed outside. The surface integration, however, has to be carried out for each far-field location. This would be still computationally intensive for a practical three-dimensional problem even though the intensity in terms of the CPU time has been much decreased compared to that required by the LEE methods. For an accurate far-field prediction, the other difficulty of using these integral methods for some aeroacoustic problems is that the control surface must completely enclose the aerodynamic source region. This may be infeasible or impossible to accomplish for some practical cases.

1.1.4 Inverse Acoustic Methods

In order to reduce aeroacoustic noise effectively, it is crucial to understand the characteristics of the aerodynamic noise sources. These characteristics, however, are not known analytically for aeroacoustic applications. With an inverse approach, the acoustic measurements in the radiated field have been used for the characterization and identification of the unsteady aerodynamic sources. In the past decade, the inverse aeroacoustic problems have been investigated with various objectives. Grace and Atassi [17, 18] first introduced the inverse method into unsteady aerodynamics and aeroacoustics. They developed an inversion model of gust/plate interaction based on solving the Helmholtz equation. The unsteady

pressure on a zero-thickness plate was successfully reconstructed using the acoustic measurement in the radiated field. Li and Zhou [19] then proposed an inversion model for the reconstruction of steady pressure distribution on a propeller surface based on the three-dimensional FW-H equation. In the work of Luo and Li [20] and Li *et al.* [21] on the gust cascade interaction and rotor wake/stator interaction, it has been shown that the accuracy of the reconstruction of the unsteady pressure distribution on the cascade and stator surfaces from the far-field acoustic measurement is excellent when the signal-to-noise ratio is not very low. Recently Gerrard *et al.* [22] have developed an inverse aeroacoustic model of subsonic axial flow fans, which can determine the circumferential blade loading variations from far-field acoustic measurements. Holland and Nelson [23] applied the inverse methods to study the distributed acoustic sources by exploiting known correlation structures among the sources. Later on, Nelson and Yoon [24] used the inverse methods to deduce the acoustic source strength from radiated field measurements.

Near-field Acoustic Holograph (NAH) is one important family of inverse acoustic methods. Several prominent inverse acoustic methods have been developed for NAH [25–34]. These methods can be classified into three categories: (1) Fourier acoustics, (2) the inverse boundary element methods (IBEM), and (3) the Helmholtz equation least squares (HELSS) method. Among these traditional inverse methods, the acoustic pressure measurement by itself is considered as the input of the inverse methods. The solution of these inverse methods, therefore, is not unique unless the input acoustic pressure is provided over a surface enclosing all the acoustic sources, i.e., a closed surface [35–37]. As a result, the effectiveness of these methods weakens when the input acoustic pressure is only available over a portion of a closed surface (i.e., open surface).

As a general rule, the more complete the input around a sound source, the more accurate the solution of the inverse problem. However, the far-field acoustic measurement over a surface enclosing the sound sources under consideration is often infeasible or impossible,

in particular for the far-field measurement. In addition, very large numbers of the field measurements are also inconceivable. Therefore, there is a need to improve the accuracy and consistency of the inverse methods especially in the case where the input acoustic data is only available over an open surface.

1.2 Acoustic Intensity-Based Method (AIBM)

Recently, with the advent of new signal processing techniques and the advances in transducer technology, acoustic intensity measurement devices have been improved to make them more reliable, accurate, and compact [45]. Using these devices, the acoustic intensity as well as simultaneous, co-located acoustic pressure can be evaluated. The acoustic pressure derivative can thus be derived along a given axis, e.g., the axis of a microphone pair.

Motivated by the need for an accurate and efficient prediction of the far-field acoustic radiation, an Acoustic Intensity-Based Method (AIBM) has been developed based on an acoustic input from an open control surface in a two-dimensional and three-dimensional configurations [38–43]. The AIBM assumes that the sound propagation is governed by the modified Helmholtz equation on and outside a control surface that encloses all the nonlinear effects and noise sources. The prediction of the acoustic radiation field is carried out by the inverse method with an input of the acoustic pressure derivative and its simultaneous, co-located acoustic pressure over a portion of the control surface. The reconstructed acoustic radiation field using the AIBM is unique due to the unique continuation theory of elliptic equations. Hence the AIBM is more stable and the reconstructed acoustic pressure is less dependent on the locations of the input acoustic data. The solution of the modified Helmholtz equation in the frequency domain is approximated by a finite linear combination of basis functions. The coefficients associated with the basis functions are obtained by matching the assumed

general solution to the given input data over an open control surface. The details on the optimization method, the instability issue and the numerical implementation of the AIBM will be discussed in the following chapters.

The “open surface” AIBM makes up the drawbacks of traditional “closed surface” approaches. It provides an effective alternative for the far-field acoustic prediction of practical aeroacoustic problems.

1.3 Organization of the Dissertation

The dissertation is organized centering at the development and application of AIBM approach. In Chapter 2, the acoustic governing equations are derived starting at the fluid mechanics conservation laws. In Chapter 3 through Chapter 5, the mathematical model, verification examples and application problems are discussed in detail.

In Chapter 3, AIBM has been proposed and modeled without considering the effect of mean flow. The mathematical and numerical formulations are first developed in a 2D configuration. Three numerical examples of acoustic radiations from either single or multi-frequency acoustic sources are presented for the verification. The advantages of the AIBM over a traditional inverse method, HELS, are demonstrated. Furthermore, the sensitivity of the AIBM to random noises with various signal-to-noise ratios (SNR) is examined.

In Chapter 4, AIBM is extended to problems with subsonic uniform flows in the 2D configuration. Firstly, The mathematical formulation for sound propagations in uniform flows is described. In addition, examples are given for the verification and demonstration of the AIBM’s capability and potential in aeroacoustic applications. The results of the AIBM are also compared with that from the FW-H integral method.

In Chapter 5, 3D AIBM with subsonic uniform flows is developed. The model is verified

by examples of the propagation of multiple acoustic sources in a uniform flow and the acoustic scattering of a time dependent source by a sphere. The effectiveness of AIBM in aeroacoustic applications is demonstrated by the accuracy and efficiency of the predicted acoustic radiations from an axisymmetric duct intake by a hybrid CAA/AIBM approach. The AIBM is much more efficient than the other methods for the far-field acoustic prediction and can use the input acoustic data from an open surface instead of a closed FW-H surface.

In the last chapter, the concluding remarks are drawn through the study in this dissertation. And the potential future work is also suggested.

Chapter 2 Aeroacoustic Governing Equations

2.1 Introduction

For acoustic propagation problems, the viscosity and thermal conductivity have little effects on the sound wave propagation. Hence the motion of the propagation media is always determined by solving Euler's equations instead of Navier-Stokes (N-S) equations. In this chapter, the linearized aerodynamic equations for an inviscid flow are firstly derived. Then the wave equation is derived with small disturbances assumption. Furthermore the Helmholtz equation, the governing equation in the frequency domain, has been obtained by performing Fourier transformation from the wave equation.

As regards of the symbols, the boldface type (**u**) denotes a vector and the same letter (*u*) in italic type is used to denote its components. The detailed physical meaning of the symbols and operators used in this chapter are listed in the Nomenclature.

2.2 Wave Equation

From the conservation laws in fluid mechanics, we can obtain the fundamental equations describing the fluid motion. These equations are called N-S equations for viscous flow or Euler's equations for inviscid flow. The wave equation for a uniform mean flow can be derived based on the fundamental fluid mechanics equations.

Assuming a sound wave propagating in an inviscid flow and there is no external force or quantity source, the governing equations (Euler's equations) are expressed as below

[10,44].

Mass conservation:

$$\frac{\partial \rho}{\partial t} + \nabla \cdot (\rho \mathbf{u}) = 0 \quad \text{or} \quad \frac{\partial \rho}{\partial t} + \frac{\partial \rho}{\partial x_i} \cdot (\rho u_i) = 0 \quad (2.1)$$

Momentum conservation:

$$\rho \left(\frac{\partial \mathbf{u}}{\partial t} + \mathbf{u} \cdot \nabla \mathbf{u} \right) = -\nabla p \quad \text{or} \quad \rho \left(\frac{\partial u_i}{\partial t} + u_j \cdot \frac{\partial u_i}{\partial x_j} \right) = -\frac{\partial p}{\partial x_i} \quad (2.2)$$

Energy conservation (isentropic flow):

$$\frac{\partial s}{\partial t} + \mathbf{u} \cdot \nabla s = 0 \quad \text{or} \quad \frac{\partial s}{\partial t} + u_j \cdot \frac{\partial s}{\partial x_j} = 0 \quad (2.3)$$

Equation of State:

$$p = p(\rho, s), \quad dp = c^2 d\rho + \left(\frac{\partial p}{\partial s} \right)_\rho ds \quad (2.4)$$

where the speed of sound c is defined as $c^2 = \left(\frac{\partial p}{\partial \rho} \right)_s$.

Introducing the acoustic perturbations,

$$p = p_0 + p', \quad \rho = \rho_0 + \rho', \quad \mathbf{u} = \mathbf{u}_0 + \mathbf{u}', \quad s = s_0 + s', \quad c^2 = c_0^2 + c'^2 \quad (2.5)$$

where $p_0, \rho_0, \mathbf{u}_0, s_0, c_0$ and $p', \rho', \mathbf{u}', s', c'$ are for the uniform and perturbation variables, respectively. And they satisfy

$$\left| \frac{\mathbf{u}'}{c} \right| \ll 1, \quad \left| \frac{p'}{p_0} \right| \ll 1, \quad \left| \frac{\rho'}{\rho_0} \right| \ll 1, \quad \left| \frac{s'}{s_0} \right| \ll 1, \quad \left| \frac{c'^2}{c_0^2} \right| \ll 1 \quad (2.6)$$

For steady flow,

$$\rho_0 \mathbf{u}_0 \cdot \nabla \mathbf{u}_0 = -\nabla p_0, \quad \nabla \cdot \rho_0 \mathbf{u}_0 = 0, \quad \mathbf{u}_0 \cdot \nabla s_0 = 0, \quad \mathbf{u}_0 \cdot \nabla p_0 = c^2 \mathbf{u}_0 \cdot \nabla \rho_0 \quad (2.7)$$

Substituting above relations into Equation (2.1) - Equation (2.4), we can get [10,44]

$$\frac{\partial \rho'}{\partial t} + \nabla \cdot (\rho_0 \mathbf{u}' + \rho' \mathbf{u}_0) = 0 \quad (2.8)$$

$$\rho_0 \left(\frac{\partial \mathbf{u}'}{\partial t} + \mathbf{u}_0 \cdot \nabla \mathbf{u}' + \mathbf{u}' \cdot \nabla \mathbf{u}_0 \right) + \rho' \mathbf{u}_0 \cdot \nabla \mathbf{u}_0 = -\nabla p' \quad (2.9)$$

$$\frac{\partial s'}{\partial t} + \mathbf{u}_0 \cdot \nabla s' + \mathbf{u}' \cdot \nabla s_0 = 0 \quad (2.10)$$

$$\frac{\partial p'}{\partial t} + \mathbf{u}_0 \cdot \nabla p' + \mathbf{u}' \cdot \nabla p_0 = c_0^2 \left[\frac{\partial \rho'}{\partial t} + \mathbf{u}_0 \cdot \nabla \rho' + \mathbf{u}' \cdot \nabla \rho_0 + \left(\frac{p'}{p_0} - \frac{\rho'}{\rho_0} \right) \mathbf{u}_0 \cdot \nabla \rho_0 \right] = 0 \quad (2.11)$$

These are the Linearized Aerodynamic Equations. They govern the propagation of small disturbances through a steady flow. If the disturbances and their gradients are not small, we can no longer apply these equations to simulate the propagation.

For a uniform fluid,

$$\mathbf{u}_0 = \text{const}, \quad \rho_0 = \text{const}, \quad p_0 = \text{const}, \quad \text{and} \quad s_0 = \text{const} \quad (2.12)$$

Taking the time derivative on Equation (2.8) and the divergence on Equation (2.9), we get

$$\frac{\partial^2 \rho'}{\partial t^2} + \rho_0 \nabla \cdot \frac{\partial \mathbf{u}'}{\partial t} + \mathbf{u}_0 \cdot \nabla \frac{\partial \rho'}{\partial t} = 0 \quad (2.13)$$

$$\rho_0 \left(\nabla \cdot \frac{\partial \mathbf{u}'}{\partial t} + \nabla \cdot (\mathbf{u}_0 \cdot \nabla) \mathbf{u}' \right) = -\nabla^2 p' \quad (2.14)$$

Then, subtracting Equation (2.13) from Equation (2.14), it yields

$$-\frac{\partial^2 \rho'}{\partial t^2} + \rho_0 \nabla \cdot (\mathbf{u}_0 \cdot \nabla \mathbf{u}') - \mathbf{u}_0 \cdot \nabla \frac{\partial \rho'}{\partial t} = -\nabla^2 p' \quad (2.15)$$

From Equation (2.8), we know,

$$\frac{\partial \rho'}{\partial t} = -\nabla \cdot (\rho_0 \mathbf{u}' + \rho' \mathbf{u}_0) = -\rho_0 \nabla \cdot \mathbf{u}' - \mathbf{u}_0 \cdot \nabla \rho' \quad (2.16)$$

Combining above two equations, we can get

$$\frac{\partial^2 \rho'}{\partial t^2} + (\mathbf{u}_0 \cdot \nabla)^2 \rho' + 2\mathbf{u}_0 \cdot \nabla \frac{\partial \rho'}{\partial t} = \nabla^2 p' \quad (2.17)$$

Considering the isentropic state equation,

$$p' = c_0^2 \rho' \quad (2.18)$$

Finally, the wave equation with a uniform mean flow is obtained.

$$\nabla^2 p' - \frac{1}{c_0^2} \left(\frac{\partial}{\partial t} + \mathbf{u}_0 \cdot \nabla \right)^2 p' = 0 \quad \text{or} \quad \left(\frac{\partial}{\partial t} + \mathbf{u}_0 \cdot \nabla \right)^2 - c_0^2 \nabla^2 p' = 0 \quad (2.19)$$

All of the small disturbance quantities describing the acoustic field satisfy the wave equation. For the notational convenience, we will use p (in the time domain) or P (in the frequency domain) to represent acoustic pressure instead of p' in the rest of this dissertation.

2.3 Helmholtz Equation

In the frequency domain, the acoustic field is governed by the Helmholtz equation which can be obtained by Fourier transformation from the wave equation. Assuming the mean flow Mach number is zero, the Helmholtz equation can be written as

$$\nabla^2 P + k^2 P = 0, \quad (2.20)$$

where P is the acoustic pressure in the frequency domain. When p is a simple harmonic function of time, p and P can be related as $p = P e^{-i\omega t}$. $k = \omega/c_0$ is the wave number, where ω is the angular frequency and c_0 is the speed of sound.

If the standard polar coordinates are used in a two-dimensional configuration, Equation (2.20) can be written as

$$\frac{\partial^2 P}{\partial r^2} + \frac{1}{r} \frac{\partial P}{\partial r} + \frac{1}{r^2} \frac{\partial^2 P}{\partial \theta^2} + k^2 P = 0, \quad (2.21)$$

In three dimension spherical coordinates, Equation (2.20) is in the following form.

$$\frac{1}{r^2} \frac{\partial}{\partial r} \left(r^2 \frac{\partial P}{\partial r} \right) + \frac{1}{r^2 \sin \theta} \frac{\partial}{\partial \theta} \left(\sin \theta \frac{\partial P}{\partial \theta} \right) + \frac{1}{r^2 \sin^2 \theta} \frac{\partial^2 P}{\partial \phi^2} + k^2 P = 0 \quad (2.22)$$

If a mean flow is considered, that is $M_a \neq 0$, modifications need to be made to the above equations. The detailed derivation for the solution in this case is given in Chapter 4 when needed.

Chapter 3 Acoustic Intensity-Based Method for Acoustic Far-Field Prediction

3.1 Introduction

Recently, the new signal processing techniques in transducer technology has been advanced dramatically. Using these devices, the acoustic intensity as well as simultaneous, co-located acoustic pressure can be evaluated. The acoustic pressure derivative can thus be derived along a given axis of a microphone pair. Motivated by the advances in acoustic measurement technology and the Helmholtz Equation Least Squares (HELs) method [32], an Acoustic Intensity-Based Method (AIBM) is proposed for the accurate reconstruction of the acoustic radiation pressure in the far field. The method uses the acoustic pressure derivative and its simultaneous pressure as the input acoustic data for the computations.

Because of the addition of the acoustic pressure gradient in the input acoustic data, the solution of the AIBM becomes unique with the input given over an open surface [35]. However, the solution is not stable since it is a Cauchy problem for Helmholtz equation [46]. Mathematically, this instability comes from the highly oscillatory modes. By carefully removing these modes, the AIBM, compared with the traditional inverse methods, could provide a measurable improvement in terms of accuracy and consistency of the reconstructed acoustic pressure. The objectives of the study in this chapter are two-fold (1) developing, numerically implementing and verifying the AIBM and (2) demonstrating the advantages, effectiveness and potential of the AIBM for engineering applications.

The chapter is organized as follows. The mathematical and numerical formulations of the AIBM are discussed in Section 3.2. The exact mathematical solution of the Helmholtz equation is approximated by finite linear combinations of basis functions. The numerical formulation and implementation are developed to effectively determine the coefficients of these basis functions by the method with an input of acoustic pressure and its derivative of a given direction. In Section 3.3, three numerical examples of acoustic radiations from either single or multi-frequency acoustic source are presented and verified. The advantages of the AIBM over a traditional inverse method are demonstrated. Furthermore, the sensitivity of the AIBM to random noises with various signal-to-noise ratios in the input acoustic data is examined and analyzed. The concluding remarks are drawn in Section 3.4.

3.2 Mathematical and Numerical Formulations

3.2.1 Mathematical Formulation

The acoustic pressure field P in the frequency domain is governed by the Helmholtz equation

$$\nabla^2 P + k^2 P = 0, \quad \text{in } \Omega = R^2 \setminus \Omega_{in}, \quad (3.1)$$

where Ω_{in} is a bounded domain in R^2 containing all acoustic sources, $k = \omega/c$ is the wave number with the angular frequency ω and the speed of sound c . If the standard polar coordinates are used in a two-dimensional configuration, Equation (3.1) can be written as

$$\frac{\partial^2 P}{\partial r^2} + \frac{1}{r} \frac{\partial P}{\partial r} + \frac{1}{r^2} \frac{\partial^2 P}{\partial \theta^2} + k^2 P = 0, \quad \text{in } \Omega = R^2 \setminus \Omega_{in}. \quad (3.2)$$

With the Sommerfeld radiation condition $\lim_{r \rightarrow \infty} r^{1/2} [\partial_r P(r, \theta) - ikP(r, \theta)] = 0$, the solu-

tion of Equation (3.2) can be written as [47, 48]

$$P(r, \theta) = \sum_{n=0}^{\infty} (a_n \cos n\theta + b_n \sin n\theta) H_n(kr), \quad (3.3)$$

where H_n is the n th-order Hankel function of the second kind. In order to obtain a solution from Equation (3.3), it is necessary to determine the coefficients a_n and b_n . These coefficients are determined by matching the assumed form of the solution to the input acoustic pressure in the HELS method [32]. Strictly speaking the solution is unique only if the input acoustic pressure is made on a boundary Γ that encloses all the acoustic sources in the domain Ω . The acoustic pressure measurement on the boundary Γ is usually impractical or infeasible for engineering applications. In practice, the input acoustic pressure is only available on a number of segments of the boundary, Γ_1 (an open surface, see Figure 3.1).

Although the AIBM could be implemented in various inverse acoustic methods, it is formulated here similar to that of the HELS [32]. It will be demonstrated later that when the input acoustic data is given over an open surface the AIBM strengthens the HELS method, and improves its mathematical well-posedness and practical applicability.

In the AIBM, both the acoustic pressure and its co-located derivative (normal to Γ_1) on the boundary Γ_1 are considered as the input acoustic data for the reconstruction of acoustic radiation pressure in the domain Ω . With the pressure derivative boundary condition as an additional input, the uniqueness of the reconstructed acoustic pressure solution is guaranteed from the unique continuation theory of elliptic equations [35–37]. In the AIBM, the partial boundary value problem for acoustic radiation pressure is defined as

$$\begin{cases} \nabla^2 P + k^2 P = 0, & \text{in } \Omega = R^2 \setminus \Omega_{in}, \\ P|_{\Gamma_1} = P, \quad \partial_{\mathbf{n}} P|_{\Gamma_1} = P_{\mathbf{n}}, & \lim_{r \rightarrow \infty} r^{1/2} [\partial_r P(r, \theta) - ikP(r, \theta)] = 0, \end{cases} \quad (3.4)$$

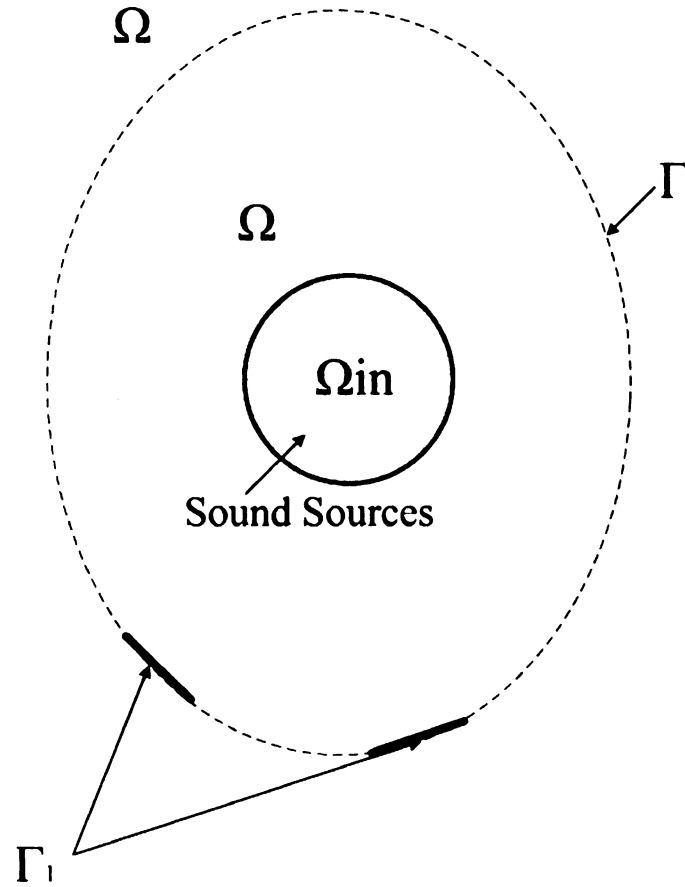


Figure 3.1: Acoustic radiation field with input acoustic data locations.

where \mathbf{n} is the outward normal to the boundary Γ_1 , P and $P_{\mathbf{n}}$ are the input acoustic pressure on Γ_1 and the pressure derivative normal to Γ_1 , respectively. The solution can then be expressed as Equation (3.3) on and outside the control surface, which encloses all the acoustic sources under consideration. It is worth mentioning that the boundary Γ_1 where the input acoustic data is provided needs to be outside of the control surface.

Although this partial boundary value problem is unique, it is not stable. Small variations in the input data may lead to large differences in the solution $P(r, \theta)$. In the following section, the numerical techniques and schemes are described for solving this partial boundary value problem. The stability conditions and other restrictions of the numerical formulation and implementation are discussed in details.

3.2.2 Numerical Formulation

In the current study, the numerical solution of Equation (3.4) is being sought by the following three steps:

Step 1: Instead of using the infinite summation in Equation (3.3), the exact solution of Equation (3.4) is approximated by a finite summation, i.e.,

$$P(r, \theta) \sim a_0 H_0(kr) + \sum_{n=1}^N (a_n \cos n\theta + b_n \sin n\theta) H_n(kr), \quad (3.5)$$

where N is a suitable integer. The choice for N will be discussed later in the section. In the AIBM, the solution P is achieved by obtaining the coefficients a_n and b_n . The coefficients are numerically determined by matching the assumed form of the solution to the input acoustic data over the boundary Γ_1 . One obvious restriction of N is that the number of coefficients ($2N + 1$) to be determined must be less than the number of the input data over Γ_1 .

Step 2: In order to determine the coefficients a_n and b_n numerically, an accurate and efficient method must be developed to evaluate each H_n . When kr is relatively large, the first Q terms in the asymptotic expansion of $H_0(kr)$ [47] are used in the current numerical calculation

$$H_0(kr) \sim H_{0,Q}(kr) = \sqrt{\frac{2}{\pi kr}} e^{-i(kr - \frac{\pi}{4})} \left[1 + \sum_{q=1}^{Q-1} (-1)^q \frac{(1/2)_q (1/2)_q}{q! (2ikr)^q} \right], \quad kr \rightarrow \infty, \quad (3.6)$$

where $(1/2)_q = 1/2(1+1/2)\dots(q-1+1/2)$. It can be shown that the accuracy established in the above approximation is of order $O\left(\frac{Q!}{(2kr)^Q}\right)$. It is also noted that the error generated by the approximation becomes unacceptable when Q is much larger than $2kr$. Since the accuracy of the method depends on a good approximation of the Hankel functions, the restriction of $Q \leq 1.5kr$ is used. For the approximation of other H_n , the recurrence relation

for H_n is employed. Because of the initial error of $O(1/r^Q)$, N has to be restricted to prevent the propagation of the errors for H_n . From a careful analysis, N should be less than $2kr$ to ensure that the error for H_n is also in the order of $O(1/r^Q)$. In addition, since the partial boundary value problem, Equation (3.4), is unstable due to the presence of functions for large index n in Equation (3.5), a proper limit on the upper bound of n is needed to control the solution instability.

When kr is relatively small, one can use the expansion of $H_0(kr)$ for $r \rightarrow 0$, or a higher order numerical integration method to evaluate $H_0(kr)$. Other H_n can be obtained again by the recurrence relation.

In the current numerical calculation, a relatively large kr (i.e., $kr = 6$) is considered and the above asymptotic expansion formulation is used. Thus, the definition of the control surface in terms of the numerical solution of P needs to be extended beyond enclosing all the acoustic sources. For a given wave number k , the radius of the control surface, r_c , is given by, e.g., $r_c \geq 6/k$. The numerical solution is valid on and outside the control surface.

Step 3: After the evaluation of the Hankel functions, a suitable optimization method is used to determine the coefficients a_n and b_n in Equation (3.5) for the partial boundary value problem (Equation (3.4)). The simplest method is the least squares technique. Because of the underlying partial differential equation and the particular basis functions used in this calculation, some numerical techniques are introduced to improve the condition numbers of the numerical schemes.

3.2.3 Numerical Implementation

If the input acoustic data, P and $P_{\mathbf{n}}$, are known at M discrete points $(r_1, \theta_1), \dots, (r_M, \theta_M)$ over the boundary Γ_1 , the linear system for the coefficients a_n and b_n is given by the

following $2M$ equations

$$a_0 H_{0,Q}(kr_j) + \sum_{n=1}^N (a_n \cos n\theta_j + b_n \sin n\theta_j) H_{n,Q}(kr_j) = P(r_j, \theta_j), \quad (3.7)$$

$$a_0 \partial_{\mathbf{n}} H_{0,Q}(kr_j) + \sum_{n=1}^N \partial_{\mathbf{n}} [(a_n \cos n\theta_j + b_n \sin n\theta_j) H_{n,Q}(kr_j)] = P_{\mathbf{n}}(r_j, \theta_j), \quad (3.8)$$

where $j = 1, \dots, M$. The above system can be expressed in a matrix form as $Ax = B$, where

$$x = [a_0, \dots, a_N, b_1, \dots, b_N]^T, \quad (3.9)$$

$$B = [P(r_1, \theta_1), \dots, P(r_M, \theta_M), P_{\mathbf{n}}(r_1, \theta_1), \dots, P_{\mathbf{n}}(r_M, \theta_M)]^T, \quad (3.10)$$

and $A = (A_1, A_2)^T$, A_1 corresponds to P and A_2 corresponds to $P_{\mathbf{n}}$. The vector coefficients x can be determined by minimizing $\|Ax - B\|$ directly for a choice of norm $\|\cdot\|$. However, when $r_1 = r_2 = \dots = r_M$, i.e, the input acoustic data is prescribed on a circular segment, it is well known that $\partial_{\mathbf{n}} H_{n,Q}(kr) = \partial_r H_{n,Q}(kr) = ikH_{n,Q}(kr) + O(1/(kr))$ and therefore the matrix $A_2 \sim ikA_1$ for a large r . In many cases, this will result a large condition number for the system $Ax = B$, and more importantly, this proportionality between A_2 and A_1 will not allow us to take the full advantage of the additional input acoustic data $P_{\mathbf{n}}$.

To overcome this difficulty, the original system is first modified as follows

$$c A_1 kr (A_2 - ikA_1)x = c Pkr (P_{\mathbf{n}} - ikP). \quad (3.11)$$

Then, to further improve the condition number for the linear system, the coefficients vector x is replaced by the vector y defined as

$$y = (a_0 H_0, a_1 H_1, \dots, a_N H_N, b_1 H_1, \dots, b_N H_N)^T. \quad (3.12)$$

The new linear system for the vector y has a much simpler matrix form

$$c D_1 D_2 y = c P k r (P_{\mathbf{n}} - ikP), \quad (3.13)$$

where

$$D_1 = \begin{pmatrix} 1 & \cos \theta_1 & \dots & \cos N\theta_1 & \sin \theta_1 & \dots & \sin N\theta_1 \\ 1 & \cos \theta_2 & \dots & \cos N\theta_2 & \sin \theta_2 & \dots & \sin N\theta_2 \\ \vdots & \vdots & \vdots & \vdots & \vdots & \vdots & \vdots \\ 1 & \cos \theta_M & \dots & \cos N\theta_M & \sin \theta_M & \dots & \sin N\theta_M \end{pmatrix} \quad (3.14)$$

$$D_2 = \begin{pmatrix} E_0 & E_1 \cos \theta_1 & \dots & E_N \cos N\theta_1 & E_1 \sin \theta_1 & \dots & E_N \sin N\theta_1 \\ E_0 & E_1 \cos \theta_2 & \dots & E_N \cos N\theta_2 & E_1 \sin \theta_2 & \dots & E_N \sin N\theta_2 \\ \vdots & \vdots & \vdots & \vdots & \vdots & \vdots & \vdots \\ E_0 & E_1 \cos \theta_M & \dots & E_N \cos N\theta_M & E_1 \sin \theta_M & \dots & E_N \sin N\theta_M \end{pmatrix} k r \quad (3.15)$$

and $E_j = \frac{H'_j(kr)}{H_j(kr)} - ik$, E_j can be obtained easily from a recurrence relation [47].

The least squares method that minimizes the standard L^2 norm $\|Dy - B\|$ is used to determine the vector y , which in turn gives values of the coefficients a_n and b_n . In the current numerical study, it is observed that although some regularization methods may be needed to improve the stability of the system for large N , they are not necessary for relatively small N . Based on the analysis given in section 2.2 (b) ($N \leq 2kr$), N is initialized within a given range of 2 - 12. The reconstructed solutions of acoustic radiation pressure for various N are compared with the input acoustic data given on the boundary Γ_1 . The total error at all the input points is then computed for each N . The optimum N within the given range is determined from the minimum overall error. The reconstruction of the acoustic field is

then carried out using the optimum N .

It should be pointed out that without the addition of the pressure gradient to the input acoustic data the reconstructed acoustic pressure could not be unique if only $P|_{\Gamma_1}$ is specified. For example, let Ω_{in} be the unit disk centered at the origin and all the acoustic sources are enclosed by the unit circle, the acoustic pressure should then satisfy the following equation

$$a_0 H_0(k) + \sum_{n=1}^{\infty} (a_n \cos n\theta + b_n \sin n\theta) H_n(k) = P(1, \theta), \quad \theta \in [0, \pi] \quad (3.16)$$

if the upper half boundary of the unit circle ($0 \leq \theta \leq \pi$) is considered as the boundary Γ_1 . It is well known that a_n and b_n are not unique from the Fourier analysis. Especially $P_{\mathbf{n}}$ has always a cosine expansion for $\theta \in [0, \pi]$, *i.e.*, $b_1 = b_2 = \dots = 0$. It is therefore impossible to predict solutions for $\theta \in (\pi, 2\pi)$.

3.3 Numerical Results and Discussions

Numerical examples are considered in this section for the purposes of: (1) verifying the AIBM and indicating the advantages of the method, (2) discussing the effects of the signal-to-noise ratio, and (3) demonstrating the potential of using the AIBM to reconstruct the acoustic radiation field for engineering applications.

3.3.1 Verification and Advantages of AIBM

The example used here is formulated by the acoustic radiation from a combination of one monopole, one dipole, and two quadrupoles in a two-dimensional domain. The acoustic pressure generated by a dipole and quadrupole source can be expressed as a summation of the pressure generated by a monopole, *i.e.*, $P(r, \theta) = \sum_{j=1}^J (A_0)_j H_0(kR_j)$, where A_0 is

the strength of the monopole and R is the distance between a field point and the monopole source. A dipole ($J = 2$) consists of two monopole sources separated by a small distance compared with the wavelength of acoustic radiation. In the frequency domain the strengths of these two monopoles are of equal amplitude but opposite sign. A quadrupole ($J = 4$) is made of two opposite dipole. The strengths and locations of these acoustic sources used in this example are given in Table 3.1. The acoustic sources are enclosed in the circle of radius $r = 1$ m. The wavenumber of the sources is considered as $k = 2\text{m}^{-1}$ and the control surface is then chosen as the circle of radius $r_c = 3$ m (see discussions on the size of the control surface in section 3.2). The label $P(r, \theta)$ used in the figures of this chapter denotes the real part of the acoustic pressure in the frequency domain. The units used for r and θ are the meter and the radian, respectively. The reconstruction of acoustic radiation pressure is carried out on and outside the control surface. The input acoustic data is given at two circular (or straight line) segments. The schematic diagram of the acoustic sources and each input segment's location is given in Figure 3.2. The starting and ending point coordinates of the two segments are chosen as $(6\text{m}, 63\pi/128)$, $(6\text{m}, 65\pi/128)$ and $(6\text{m}, 63\pi/128 + \gamma)$, $(6\text{m}, 65\pi/128 + \gamma)$ in the polar coordinates. It is noted that the input data is given over an open surface and the circular arc length of each segment is only $1/128$ of the circumference of the circle. Each segment is then discretized uniformly into ten grid points where the analytical acoustic pressure and its derivative normal to the segments are given as the input acoustic data. The angle γ shown in Figure 3.2 is a measure of the dimensionless distance between the two segments of the input, with $\gamma = \pi$ being the farthest, i.e., the segments are at the opposite sides of the control surface. Different values of γ are considered to examine the sensitivity of the reconstructed acoustic radiation pressure against various input locations of an open surface.

In order to determine if the addition of the pressure gradient in the input acoustic data would improve the accuracy and consistency of the inverse method, two sets of the input acoustic data are considered. The first set of the input consists of the analytical acoustic

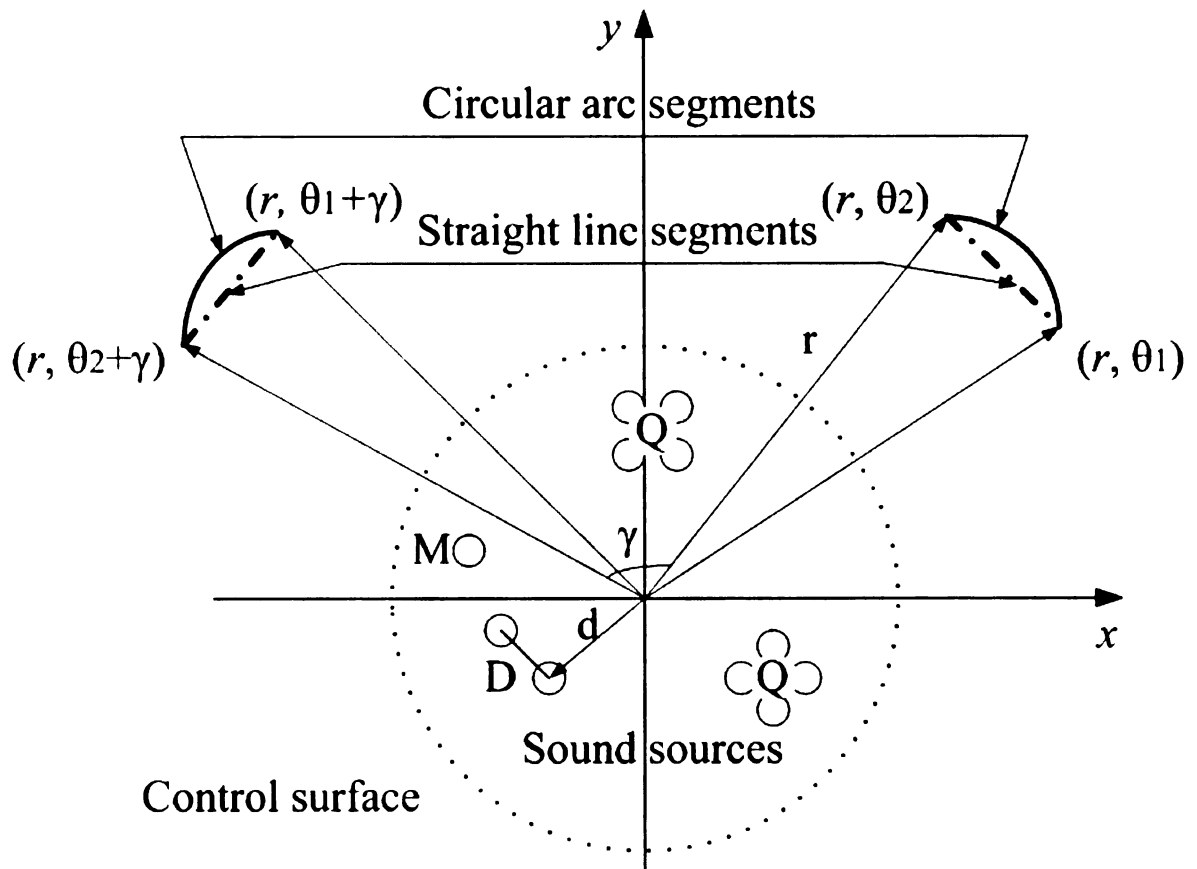


Figure 3.2: Schematic diagram of acoustic sources and each input segment's location.

Table 3.1: The strengths and distributions of the 2D acoustic sources

	$A_0(W/m^2)$	$x(m)$	$y(m)$
Quadrupole I	1.00	0.30	0.60
	-1.00	-0.10	0.60
	1.00	-0.10	0.20
	-1.00	0.30	0.20
Quadrupole II	-1.20	0.49	-0.12
	1.20	0.20	-0.20
	-1.20	0.28	-0.49
	1.20	0.57	-0.41
Dipole	-0.80	-0.54	-0.16
	0.80	-0.78	-0.45
Monopole	0.90	-0.58	-0.58

pressure and its normal derivative, *i.e.*, the AIBM, and the second set of the input consists of only the analytical acoustic pressure, which is referred as the AIBM_without. Since in this study both the AIBM and AIBM_without are implemented using the least squares method, it allows us to examine the sole effect of the addition of the pressure derivative in the input acoustic data.

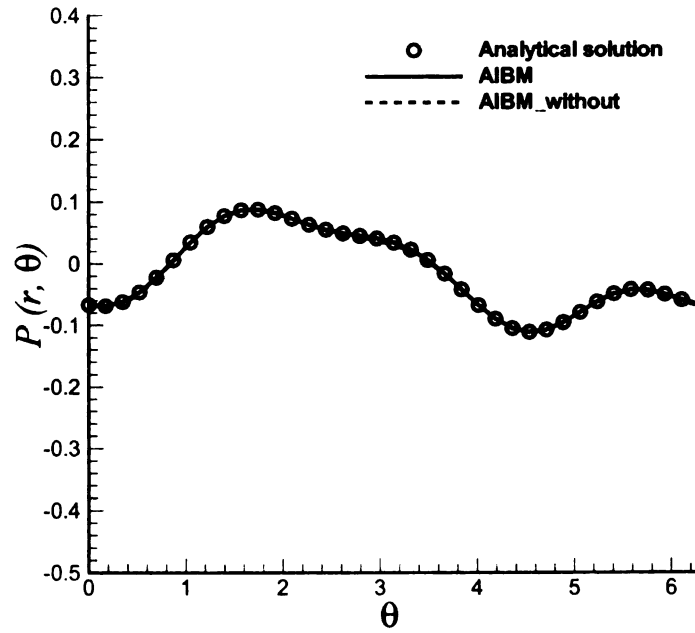
The reconstructed acoustic radiation pressure at $r=50m$ is compared with the analytical solution for four different values of γ in Figure 3.3. Since the reconstructed pressure calculated using the input acoustic data from the two straight line segments are identical to that using the input from the two circular segments, only the results based on the input from the circular segments are shown in Figure 3.3. It can be seen clearly that the reconstructed acoustic pressure obtained from the AIBM_without deteriorates in some regions as γ deviates from π . On the other hand, the reconstructed acoustic pressure from the AIBM

agrees reasonably well with the analytical solution for $\gamma = 0.8\pi$ and 0.6π . The results demonstrate that the reconstructed acoustic pressure using the AIBM is less dependable on the input location of the acoustic data. The AIBM gives more consistent, reliable and accurate reconstruction of acoustic radiation pressure when the input acoustic data is available over an open surface. However, for the case of $\gamma = 0.4\pi$, the solution of the AIBM starts to deviate from the analytical solution. As γ decreases further, the effectiveness of the AIBM becomes hindered. As a general rule, the more complete the input around an acoustic source, the more accurate the reconstructed acoustic pressure solution. If the input is given on a single segment over an open surface, a considerable extent of the segment is needed in order to achieve acoustic pressure reconstructions with acceptable accuracy. If the input is available on multiple segments over an open surface around an acoustic source, then a better accuracy of the reconstructed solution will be obtained when the segments are on the opposite sides of the control surface, although the exact location of the acoustic source may not be known.

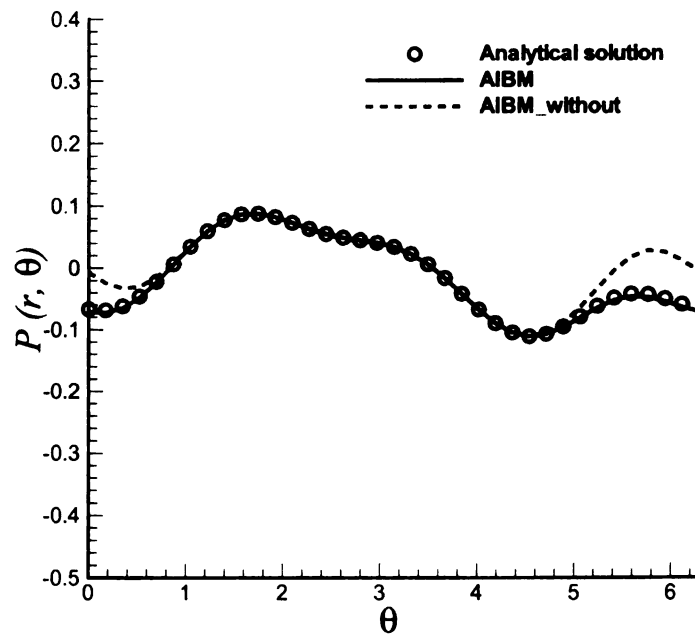
It is also worth mentioning that for an input given over a closed surface, the reconstructed acoustic pressure solution is unique without the addition of the pressure gradient to the input acoustic data. The advantage of the AIBM over the AIBM_{without} diminishes. The formulation used for the AIBM_{without} is identical to that of the HELS [32]. Therefore, by including the pressure gradient in the input of the HELS, the mathematical well-posedness of the HELS will be improved and the method will be enhanced.

3.3.2 Effect of Signal-to-Noise Ratio (SNR)

Until now the analytical solution has been used as the input acoustic data for the calculation. In practice, however, the input data is usually experimentally measured. The acoustic measurements are unfortunately prone to random errors. It is therefore desirable to have the reconstructed acoustic radiation pressure less sensitive to random noises. In the following,



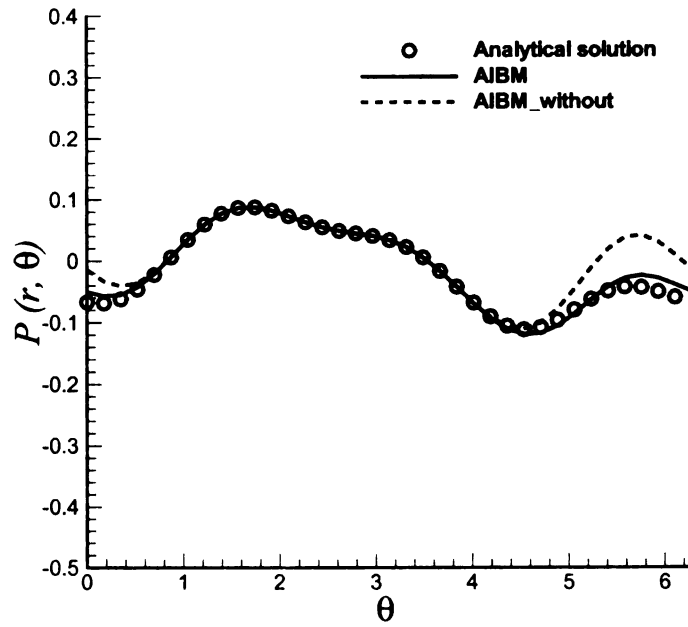
(a) $\gamma = 1.0\pi$



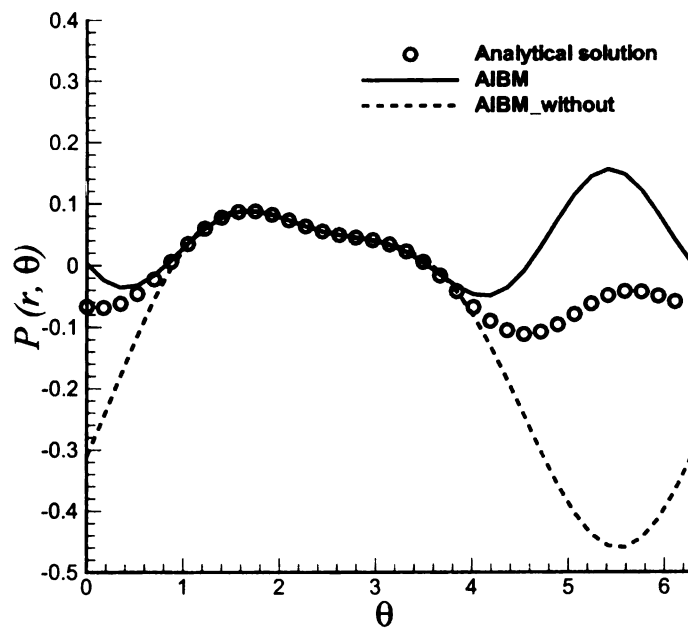
(b) $\gamma = 0.8\pi$

Figure 3.3: Comparisons of reconstructed acoustic radiation pressure with analytical solution at $r = 50\text{m}$ for different γ .

Figure 3.3 continued



(c) $\gamma = 0.6\pi$



(d) $\gamma = 0.4\pi$

the effect of the SNR is investigated in a two-dimensional configuration using an acoustic source similar to a monopole but with an amplitude proportional to a sine function.

Assuming the sound source is located at (x_0, y_0) , i.e., $x_0 = 0.8\text{m}$, $y_0 = 0.6\text{m}$, the exact solution is constructed in the following form

$$P_c(r, \theta) = \sin \alpha H_1(kR), \quad (3.17)$$

where $R = \sqrt{(x - x_0)^2 + (y - y_0)^2}$. α is the shifted angle and is given by $\tan \alpha = (x - x_0)/(y - y_0)$. Like the previous example, the acoustic source is enclosed in the circle of $r = 1\text{m}$. The wavenumber and the radius of the control surface are given as $k = 2\text{m}^{-1}$ and $r_c = 3\text{m}$, respectively. The input acoustic data consists of the exact acoustic pressure solution with an added random noise $RN(r, \theta)$.

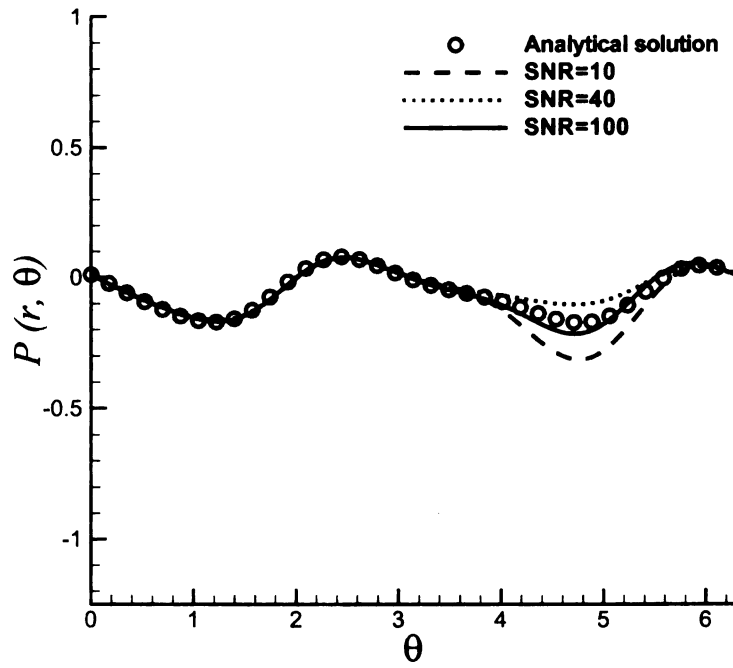
$$P = P_e + RN \quad (3.18)$$

The location of the input is chosen as the upper half circle of radius $r = 6\text{m}$ (an open surface). The SNR is defined as

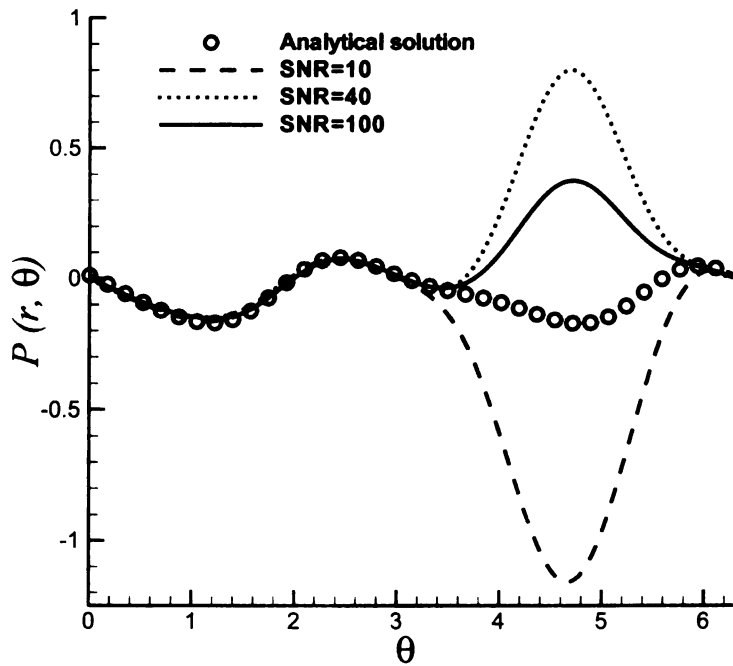
$$\text{SNR} = \sqrt{\frac{\sum_{m=1}^M |P_e(r, \theta_m)|^2}{\sum_{m=1}^M |RN(r, \theta_m)|^2}} \quad (3.19)$$

where m represents each uniformly distributed grid point ($M = 200$) over the upper half circle, and the random noise has zero mean and the identity covariance matrix. The reconstructed acoustic radiation pressure from the AIBM and AIBM_without is compared with the analytical solution in Figure 3.4 for different SNRs. The results demonstrate that the accuracy of the reconstructed acoustic pressure with the SNR up to 10 is overall acceptable for the AIBM. However, without the addition of the acoustic pressure gradient in the input acoustic data, the reconstructed acoustic pressure from the AIBM_without is unac-

ceptable even for the SNR as large as 100. In order to have an overview of the reconstructed acoustic radiation field, the acoustic pressure contours of the analytical solution and the reconstructed solutions from the two inverse methods are given in Figure 3.5. Since the input acoustic data is given over the upper half circle, as expected the reconstructed acoustic pressure for the upper half domain is very accurate using both inverse methods. The contour plots also show that the reconstructed pressure contours in the lower half domain of the AIBM_{without} are completely different from the analytical solution even with SNR=100. On the other hand, the accuracy of the reconstructed acoustic pressure in the lower half domain of the AIBM is very good for the same SNR. The results indicate that by including the pressure gradient in the input acoustic data, the AIBM can handle random noises much more effectively. As it is shown in Figure 3.4, with up to 10% random noises (SNR=10), the reconstructed acoustic radiation pressure using the AIBM agrees with the analytical solution reasonably well.

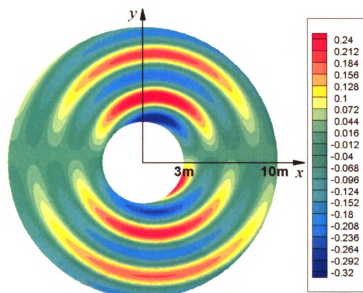


(a) AIBM

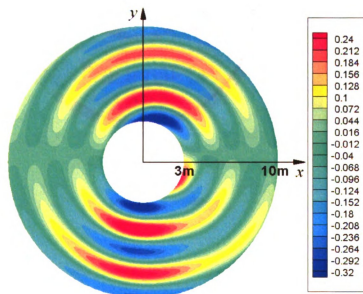


(b) AIBM_without

Figure 3.4: Effects of SNRs on reconstructed acoustic radiation pressure at $r = 10\text{m}$.



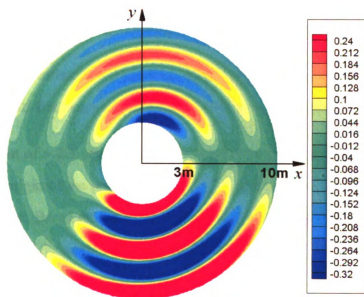
(a) Analytical Solution



(b) AIBM

Figure 3.5: Comparisons of reconstructed acoustic radiation pressure $P(r, \theta)$ contours for SNR=100 with analytical solution.

Figure 3.5 continued



(c) AIBM.without

3.3.3 Application to Multi-Frequency Acoustic Radiation Problem

The acoustic radiation from 2D vortex filament moving around the edge of a semi-infinite plane is a simplified model for the radiation of flow-airfoil interaction problem in relation to the airframe noise study. Ffowcs William & Hall [49] initially developed the general theory of the scattering of aerodynamic noise by flow-surface interaction. Shortly after, Crighton [50] developed the simplified 2D vortex model and derived the analytical acoustic solution in the form of the potential function using the singular perturbation method. Since then, the model has been used [51] to verify the effectiveness of the numerical methods of solving the Ffowcs Williams and Hawkings (FW-H) integral equation.

In the current study, the vortex model is used to show the capability and potential of applying the AIBM for multi-frequency acoustic radiation problems in general.

A schematic diagram of a 2D vortex moving around a semi-infinite half plane is shown in Figure 3.6. The origin of the polar (or Cartesian) coordinates is located at the edge of the semi-infinite plane. Based on the analysis given by Crighton [50], the first term in the asymptotic expansion of the analytical potential function as $U_m \rightarrow 0$ is given by

$$\Phi(r, \theta, t) = \frac{4^{\frac{3}{4}} U_m d^2}{[M_a^2(r - tc)^2 + 4]^{\frac{1}{4}}} \frac{\sin \frac{1}{2}\theta}{r^{\frac{1}{2}}}, \quad \theta \in (-\pi, \pi), \quad (3.20)$$

where c is the speed of sound, d is the shortest distance between the vortex and the edge (see Figure 3.6), U_m is the maximum speed of vortex motion, and the Mach number M_a is defined as $M_a = U_m/c$. These variables are considered as $c = 344\text{m/s}$, $d = 1\text{m}$ and $M_a = 0.01$ in the current numerical investigation. It can be easily shown that the acoustic pressure derived from the above potential function satisfies the wave equation and the solid wall boundary condition, $\partial p/\partial y = 0$ at the top and bottom surfaces of the plane. Since the acoustic radiation of the vortex model problem is not in a free space, the general

approximated solution (Equation (3.5)) for the Helmholtz equation needs to be modified to satisfy the solid wall boundary condition and can be written as

$$P(r, \theta) = \sum_{n=0}^N \left[a_n \cos n\theta H_n(kr) + b_n \sin \left(n + \frac{1}{2} \right) \theta H_{n+\frac{1}{2}}(kr) \right]. \quad (3.21)$$

As it can be seen from Equation (3.20), the acoustic radiation of the vortex model problem is not a single frequency problem. The FFT of the acoustic pressure time history at a field point with the polar coordinates $(75\text{m}, \pi/4)$ is shown in Figure 3.7. The continuum spectrum demonstrates the multi-frequency nature of the acoustic radiation. It can also be shown mathematically that the pressure time history of any given point in the field has the same frequency spectrum although the amplitude may vary. Since the AIBM is a frequency domain method, the reconstructed acoustic pressure field for each frequency component needs to be calculated. A superposition of the contribution from each frequency gives the total acoustic pressure field in the frequency domain. The reconstructed acoustic pressure field in the time domain can then be obtained by an inverse FFT. In order to accurately reconstruct the acoustic pressure, all the dominant frequency components need to be included in the calculation. The input acoustic data for the AIBM consists of the analytical acoustic pressure at four uniformly distributed points on each of the two circular segments ($r = 50\text{m}$) as shown in Figure 3.6.

The reconstructed acoustic pressure time history at a field point with the polar coordinates $(100\text{m}, \pi/5)$ and the directivity pattern at the radius of $r = 100\text{m}$ are calculated by the AIBM and compared with the respective analytical solutions in Figures 3.8 - 3.10 for three selected ranges of the frequency components. The poor agreement between the analytical and the reconstructed acoustic pressure shown in Figure 3.8 is expected since the input acoustic data includes only a small portion (0.05 to 0.2Hz) of the dominant frequency components. As the frequency range widens to include more dominant frequency components (0.05 to 0.45Hz), the accuracy of the reconstructed acoustic solutions using the AIBM im-

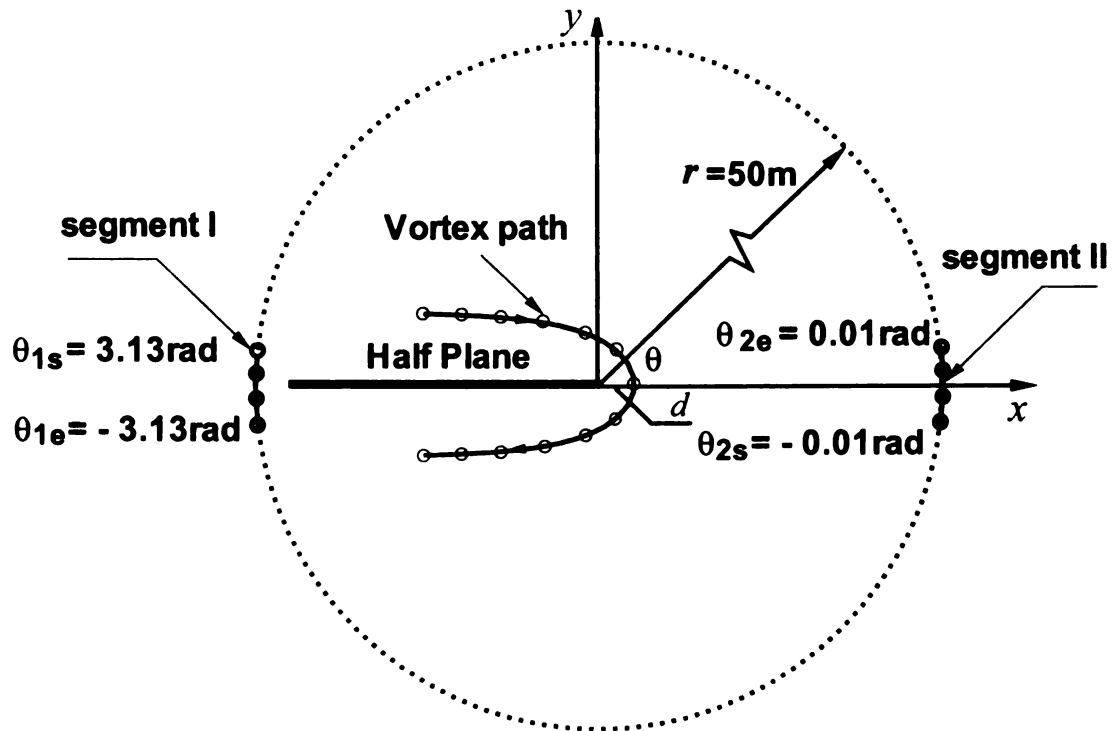


Figure 3.6: Schematic diagram of 2D vortex filament moving around the edge of a semi-infinite plane and input acoustic data points on specified segments.

proves significantly (see Figure 3.9). Finally, an excellent agreement is achieved between the analytical and the AIBM solutions if the frequency range widens further to include all frequency components from 0.05 to 1.45Hz in the input acoustic data (see Figure 3.10).

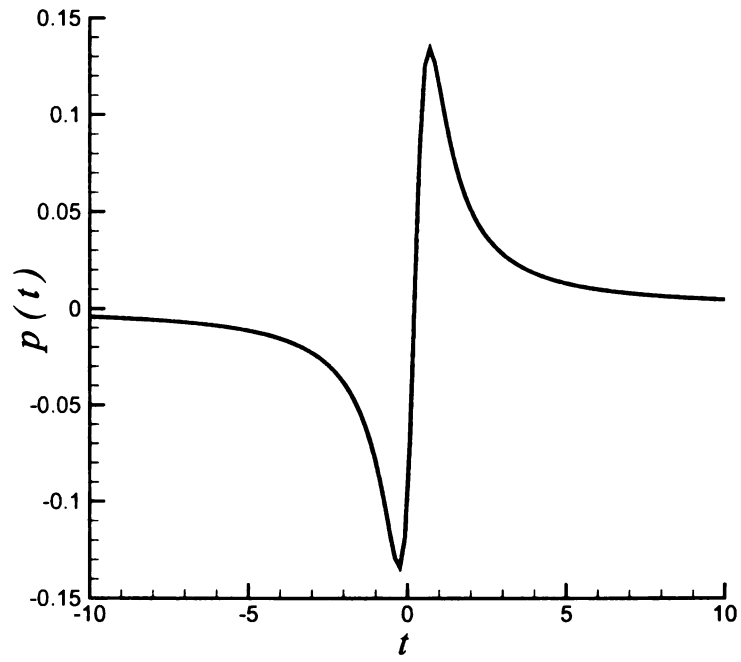
After the verification of the AIBM for the reconstruction of acoustic radiation pressure generated by the multi-frequency model problem, it is important to examine the sensitivity of the reconstructed acoustic pressure to the SNR to ensure the potential of the AIBM for engineering applications. Since the acoustic radiation of the vortex model problem involves multi-frequency components, a random noise is added to the input acoustic data in the time

domain. For a given set of the input acoustic data, the SNR is defined as

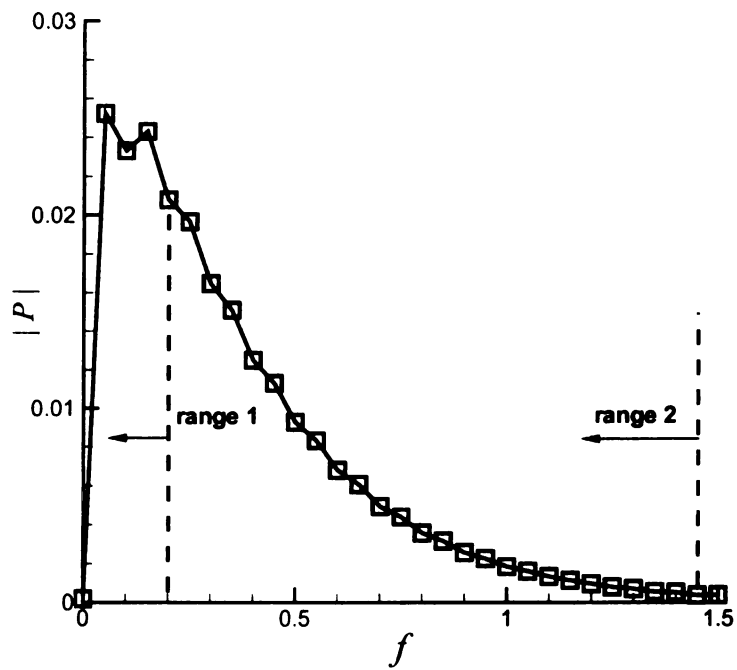
$$\text{SNR} = \left[\frac{\sum_{i=1}^M \sum_{j=1}^N p^2(t_j, \mathbf{x}_i)}{M \cdot N \cdot \sigma} \right]^{1/2} \quad (3.22)$$

where M and N are the numbers of the input locations (points) and the time discretization over a period of measurement time (or data collection time), σ is the variance of the random noise. The mean of the random noise is zero. It is noted from Equation (3.22) that the SNR is defined based on the average of the input acoustic data in the time domain. Since the magnitude of the input data varies, the SNR could be larger or smaller than defined for an input at a specific location.

Using the input locations shown in Figure 3.6, the effect of the SNR on the acoustic radiation pressure time history at a given point in the field is shown in Figure 3.11 for different SNRs. As it is shown, a very good agreement between the reconstructed solution and the analytical solution is obtained for the case of SNR=10. As the SNR decreases to 5, the error of the reconstructed acoustic pressure increases as expected, particularly in the region where the amplitude of the analytical pressure is small as expected. Nevertheless, the results demonstrate that the AIBM can effectively handle the input acoustic data with up to 20% random noise.

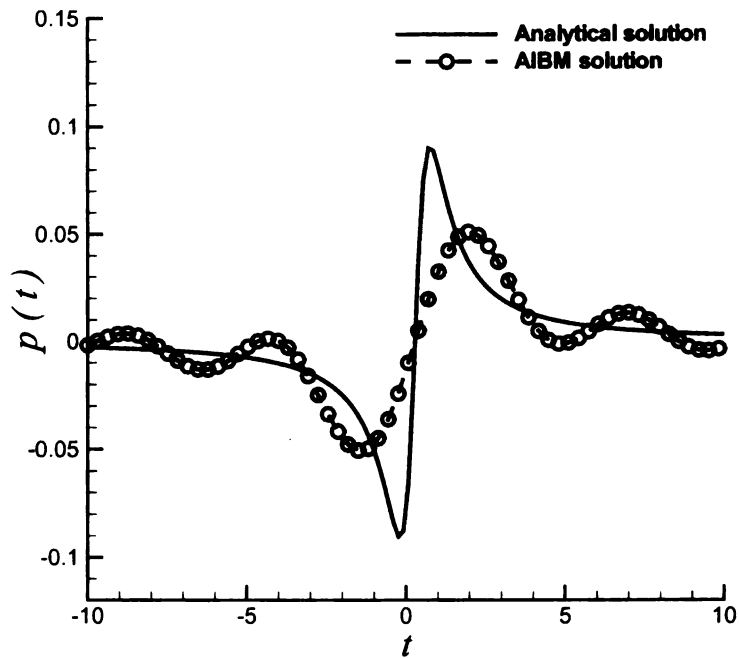


(a) Acoustic pressure time spectrum

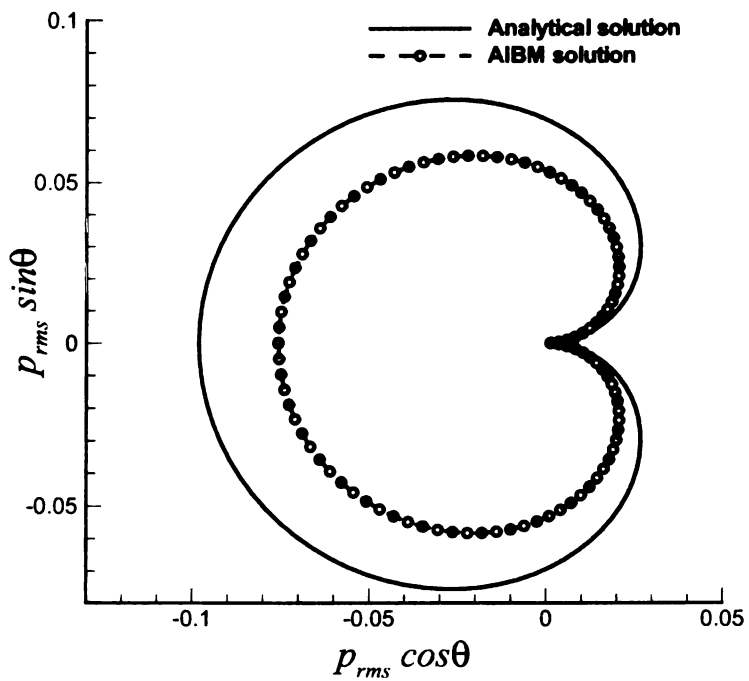


(b) Frequency spectrum

Figure 3.7: Spectrum of acoustic radiation pressure time history of 2D vortex model at $r = 75\text{m}$, $\theta = \pi/4$, $M_a = 0.01$ and $d = 1\text{m}$.

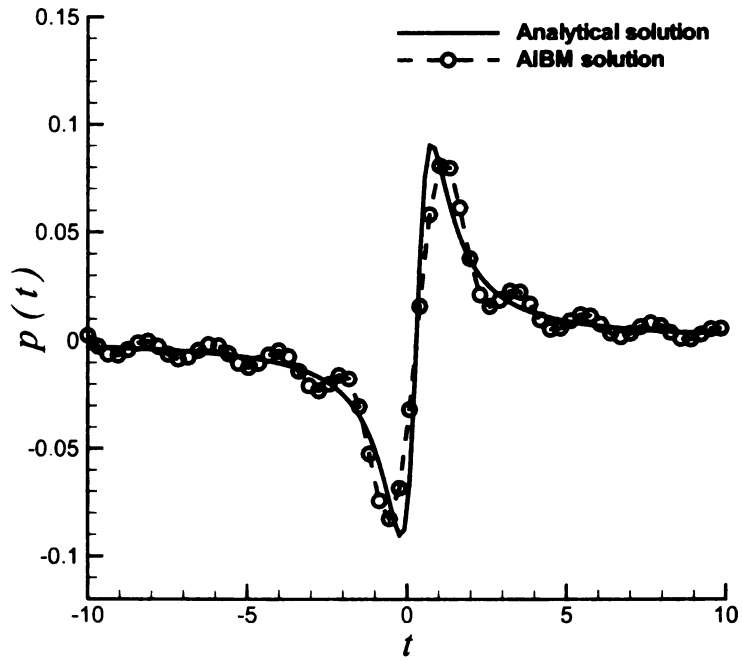


(a) Acoustic pressure time history ($r=100\text{m}$, $\theta = \pi/5$)

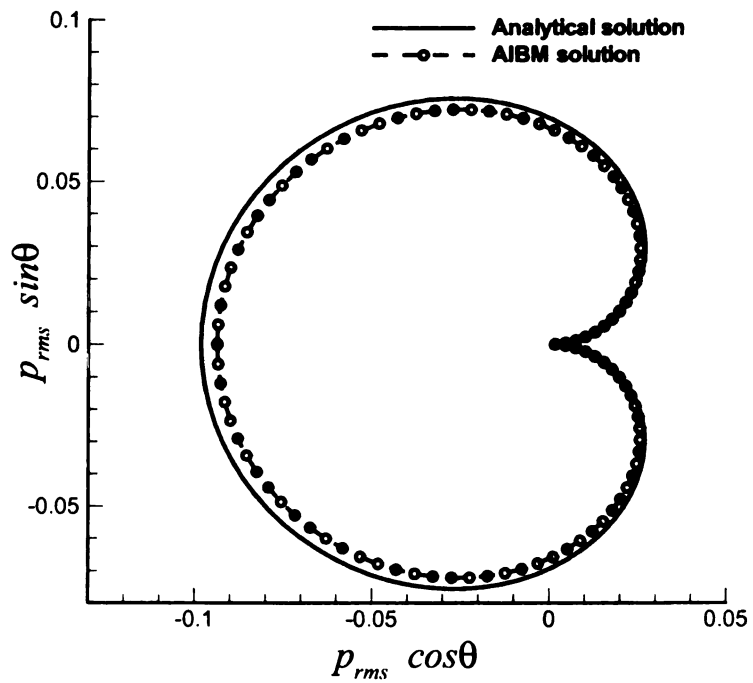


(b) Directivity ($r=100\text{m}$)

Figure 3.8: Acoustic radiation pressure and directivity calculated from the input data with frequency range of 0.05 - 0.2Hz.

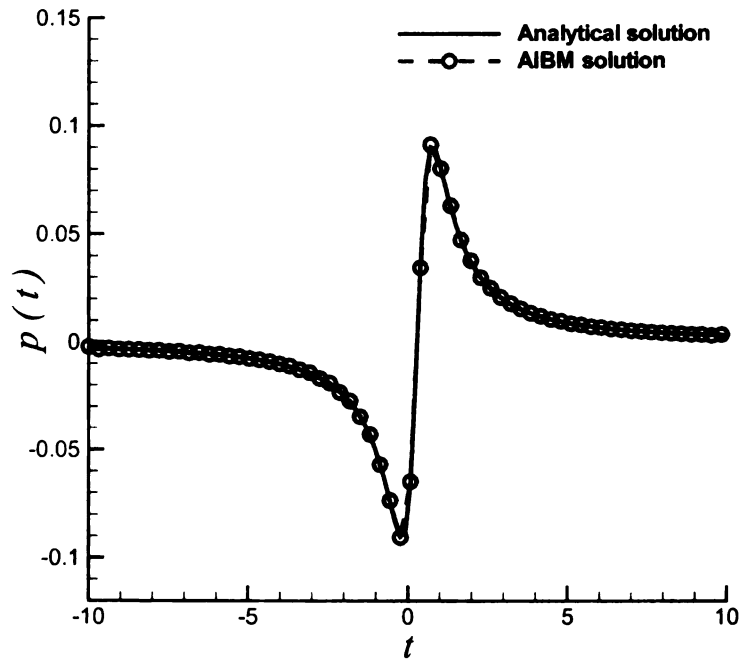


(a) Acoustic pressure time history ($r=100\text{m}$, $\theta = \pi/5$)

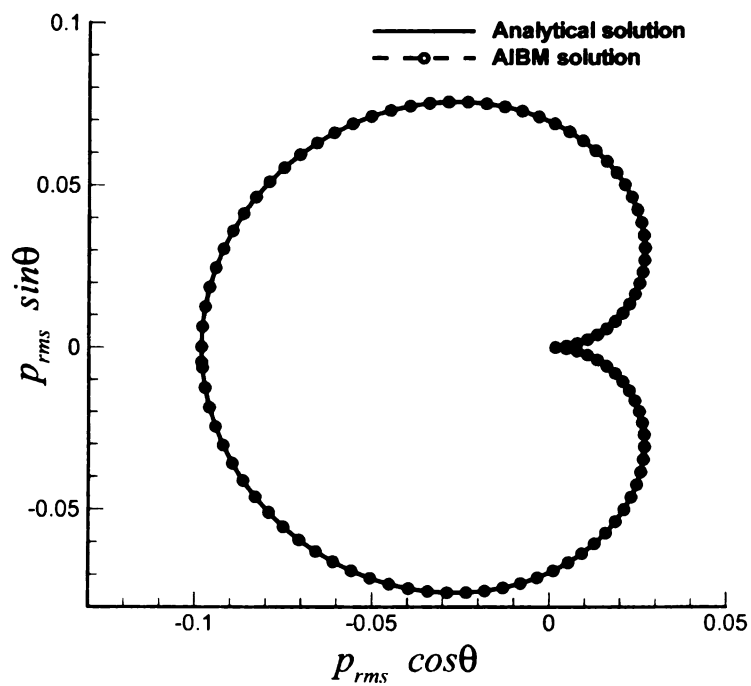


(b) Directivity ($r=100\text{m}$)

Figure 3.9: Acoustic radiation pressure and directivity calculated from the input data with frequency range of 0.05 - 0.45Hz.

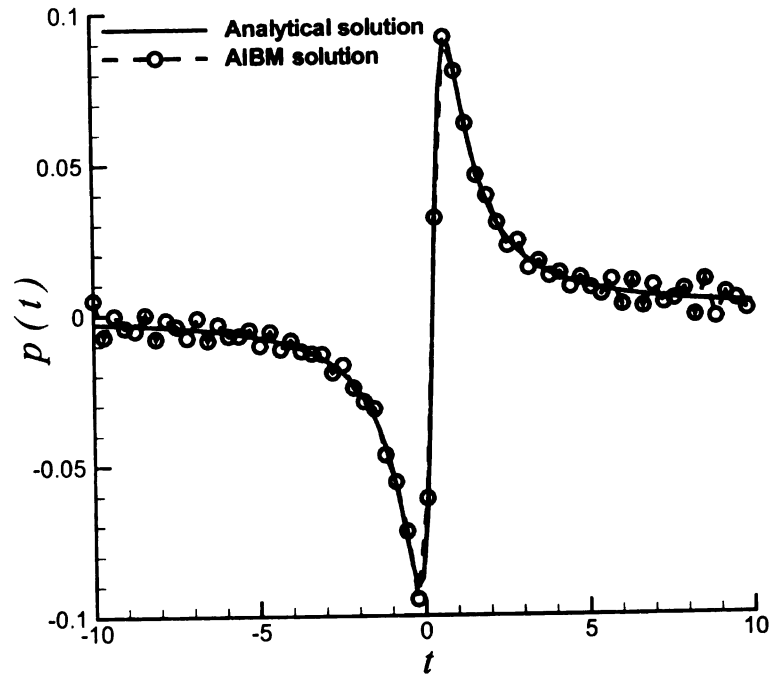


(a) Acoustic pressure time history ($r=100\text{m}$, $\theta = \pi/5$)

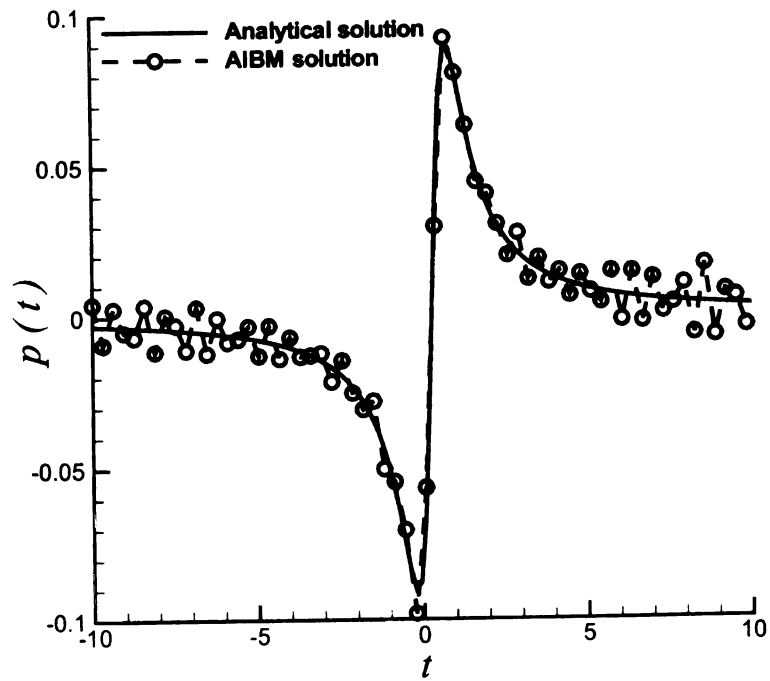


(b) Directivity ($r=100\text{m}$)

Figure 3.10: Acoustic radiation pressure and directivity calculated from the input data with frequency range of 0.05 - 1.45Hz.



(a) SNR=10



(b) SNR=5

Figure 3.11: Acoustic radiation pressure time history ($r = 100\text{m}$, $\theta = \pi/5$).

Chapter 4 2D AIBM with Subsonic Mean Flow

4.1 Introduction

In Chapter 3, an acoustic intensity-based method (AIBM) has been proposed without considering the effects of mean flow. The objectives of this chapter are to extend the AIBM to include sound propagations in uniform flows and demonstrate the capability of the method when coupling with the near-field CFD/CAA methods for the prediction of far-field sound radiations in a two-dimensional configuration.

First of all, the mathematical formulation and numerical implementation of the AIBM for sound propagations in uniform flows is described in Section 4.2. In Section 4.3, The method is then coupled with the near-field CFD/CAA methods for the prediction of sound radiations in the far field. An example of sound radiation from monopole in a uniform flow is solved for the verification. Two aeroacoustic problems, sound radiation by a flow around a NACA airfoil and sound scattering by a cylinder, are solved in the following sections to demonstrate the effectiveness of the CFD/AIBM and CAA/AIBM hybrid techniques. At the same time, the sound radiation field obtained from the AIBM and the FW-H integral method are compared. The effects of input locations and the signal-to-noise ratio (SNR) on the accuracy of the AIBM solution are examined. Conclusions are drawn in Section 4.4.

4.2 Mathematical Formulations

In this section the formulation of the AIBM [38] is extended to include sound propagations in uniform flows. Without loss of generality, we assume the uniform mean velocity is in x -direction $\mathbf{u}_0 = u_0\mathbf{i}$. Let Ω_{in} be a bounded domain in R^2 containing all acoustic sources in this mean flow (see Figure 4.1), and c be the speed of sound, it is well-known that the acoustic pressure $p(x, y, t)$ is governed by the following homogeneous wave equation

$$\nabla^2 p - \frac{1}{c^2}(\partial_t + \mathbf{u}_0 \cdot \nabla)^2 p = 0. \quad (4.1)$$

Two cases will be considered in this paper. One is the problem with a single frequency, the other is with multiple frequencies.

4.2.1 A Single Frequency

Assume that $p = e^{i\omega t} P(x, y)$ with angular frequency ω , $P(x, y)$ satisfies

$$\nabla^2 P - M_a^2 P_{xx} - 2ikM_a P_x + k^2 P = 0, \quad (4.2)$$

where $k = \omega/c$ is the wave number. $M_a = u_0/c$ represents the Mach number, which is assumed to be less than 1 in the current study. In order to get the solution of Equation (4.2), we want to convert this equation to the standard Helmholtz equation.

Set $W(\hat{x}, \hat{y}) = P(x, y)$ with $(\hat{x}, \hat{y}) = (x/\beta, y)$ and $\beta = \sqrt{1 - M_a^2}$, the governing equation of P , Equation (4.2), can be rewritten as

$$\nabla^2 W - \frac{2ikM_a}{\beta} W_{\hat{x}} + k^2 W = 0. \quad (4.3)$$

To eliminate the first order term $W_{\hat{x}}$, we define the function $S(\hat{x}, \hat{y})$ as

$$S(\hat{x}, \hat{y}) = \exp[-ikM_a\hat{x}/\beta]W(\hat{x}, \hat{y}). \quad (4.4)$$

The equation for S is therefore expressed as

$$\nabla^2 S + \frac{k^2}{\beta^2} S = 0. \quad (4.5)$$

In terms of the polar coordinates for $\hat{x}\hat{y}$ -plane, $\hat{x} = \hat{r} \cos \hat{\theta}$, $\hat{y} = \hat{r} \sin \hat{\theta}$ and $\hat{r} = \sqrt{\hat{x}^2 + \hat{y}^2}$. the general solution for S on or outside a control surface, which encloses all the sound sources under consideration, is given by

$$S(\hat{x}, \hat{y}) = \sum_{n=0}^{\infty} (a_n \cos n\hat{\theta} + b_n \sin n\hat{\theta}) H_n(k\hat{r}/\beta), \quad (4.6)$$

where H_n is the n th-order Hankel function of the second kind. Combining these equations yields

$$P(x, y) = \exp(ikMx\beta^{-2}) \sum_{n=0}^{\infty} (a_n \cos n\hat{\theta} + b_n \sin n\hat{\theta}) H_n(k\hat{r}/\beta). \quad (4.7)$$

Note that x is scaled by the factor $\beta = \sqrt{1 - M_a^2}$, \hat{r} is not the usual $\sqrt{x^2 + y^2}$, and $\hat{\theta}$ are also different from the usual angle θ in the polar coordinates for xy -plane.

In order to obtain the solution of Equation (4.7), it is necessary to determine the coefficients a_n and b_n . These coefficients are determined by matching the assumed form of the solution to the measured acoustic pressure and its normal derivative over the input surface segments. Once these coefficients are determined, the solution can be quickly evaluated at any field point on or outside the control surface. In the AIBM, both the acoustic pressures and its simultaneous, co-located derivative (in out normal direction) on the boundary Γ_1 are given as the input for the reconstruction of the acoustic field in the domain Ω (see Figure 4.1). With the pressure derivative boundary condition as an additional input, the uniqueness of

the reconstructed solution is guaranteed from the unique continuation theory of elliptical equations [35–37]. The method also yields a consistent and accurate solution on and outside of the control surface. When using the AIBM, it is assumed that the control surface is known although the exact locations of sound sources may not be available.

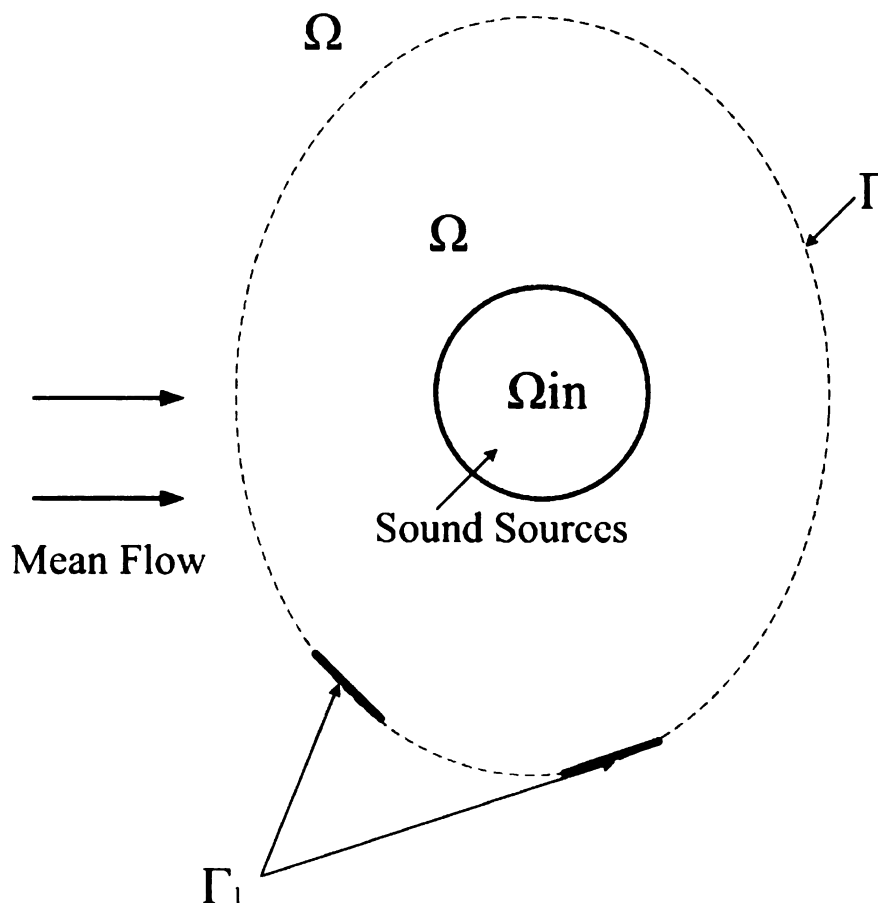


Figure 4.1: Schematic diagram of sound propagation field and locations of acoustic measurements.

With the consideration of sound propagations in uniform flows, the partial boundary value problem is defined as

$$\begin{cases} \nabla^2 P - M_a^2 P_{,xx} - 2ikM_a P_x + k^2 P = 0 & \text{in } \Omega = R^2 \setminus \Omega_{in}, \\ P|_{\Gamma_1} = P, \quad \partial_{\mathbf{n}} P|_{\Gamma_1} = P_{\mathbf{n}}, \end{cases} \quad (4.8)$$

where \mathbf{n} is the outward normal to Γ_1 . Similar to the procedures given in our earlier work

[38], the following three steps are used to solve Equation (4.8) in the solution form given by Equation (4.7).

Step 1: The infinite summation in Equation (4.7) is replaced by a finite summation, i.e.,

$$P(x, y) \sim \exp(ikM\hat{x}/\beta) \left[a_0 H_0(k\hat{r}/\beta) + \sum_{n=1}^N (a_n \cos n\hat{\theta} + b_n \sin n\hat{\theta}) H_n(k\hat{r}/\beta) \right], \quad (4.9)$$

where N is a suitable integer. The choice for N will be discussed later in the section. Obviously, one restriction is that the number of coefficients ($2N + 1$) to be determined must be less than the number of the measurement or input points.

Step 2: An accurate and efficient method must be developed to evaluate each H_n . When $k\hat{r}/\beta$ is relatively large, the first Q terms in the asymptotic expansion of $H_n(r)$, namely $H_n(r) \sim H_{n,Q}(r)$, are used in the current numerical study. For the completeness, we derive the expression for $H_{n,Q}$ here. Even though the asymptotic expansion for Bessel functions are well documented, it seems that the expansion for H_n cannot be found easily.

It is known that H_n has the following explicit integral expression [52]

$$H_n(r) = -\frac{r^n}{2^{n-1}\Gamma(n+1/2)\sqrt{\pi}} \int_{-1+i\infty}^{-1} e^{irt} (1-t^2)^{n-1/2} dt. \quad (4.10)$$

By the change of variable for integration, $t = -1 + i\eta$, we have

$$H_n(r) = i \frac{e^{(n-1/2)\pi i/2} r^n e^{-ir}}{\Gamma(n+1/2)} \sqrt{\frac{2}{\pi}} \int_0^\infty e^{-r\eta} \left(\eta - \frac{i\eta^2}{2}\right)^{n-1/2} d\eta. \quad (4.11)$$

Furthermore by letting $\tau = r\eta$, the asymptotic expansion of H_n for $r \rightarrow \infty$ is derived as

$$H_n(r) = \sqrt{\frac{2}{\pi r}} e^{-i(r-n\pi/2-\pi/4)} \left[1 + \sum_{j=1}^Q \frac{(-i)^j (n-1/2)_j \Gamma(n+j+1/2)}{j! 2^j r^j \Gamma(n+1/2)} \right] = H_{n,Q} \quad (4.12)$$

It is easy to see that the order of error established in the above approximation is

$$E(n, Q)(r) = \frac{1}{Q!(2r)^j} \prod_{j=1}^Q (n - j + 1/2)(n + j - 1/2), \quad (4.13)$$

which tends to ∞ when $N \rightarrow \infty$ or $Q \rightarrow \infty$. Hence the asymptotic expansion is not convergent, it is necessary to choose N and Q carefully. For fixed r and n , the error $E(n, Q)(r)$ is roughly $\frac{Q!}{(2r)^Q}$, the restriction of $Q \leq 2r$ should be used to control the approximation errors. Furthermore, for fixed r and Q , N (the maximum of n) must also be controlled from $E(N, Q)(r) \sim \frac{N^Q}{(2r)^Q}$, which requires that N cannot be larger than $2r$ as well. In this study, we will restrict our choice so that $Q \leq 1.5k\hat{r}/\beta$ and $N \leq 1.5k\hat{r}/\beta$.

Step 3: Suitable optimization method is used to determine the coefficients a_n and b_n . For the partial boundary value problem, Equation (4.8), the simplest method is the least squares technique because the resulting equations for a_n and b_n are linear. If g_1 and g_2 are known at M discrete points, $(r_1, \theta_1), \dots, (r_M, \theta_M)$, the linear system for the coefficients a_n and b_n is given by the following $2M$ equations

$$e^{ikMa\hat{x}_j/\beta} \left(a_0 H_{0,Q} + \sum_{n=1}^N (a_n \cos n\hat{\theta}_j + b_n \sin n\hat{\theta}_j) H_{n,Q} \right) = P(x_j, y_j), \quad (4.14)$$

$$\partial_{\mathbf{n}} \left[e^{ikMa\hat{x}_j/\beta} \left(a_0 H_{0,Q} + \sum_{n=1}^N (a_n \cos n\hat{\theta}_j + b_n \sin n\hat{\theta}_j) H_{n,Q} \right) \right] = P_{\mathbf{n}}(x_j, y_j), \quad (4.15)$$

where $j = 1, \dots, M$. It is noted that in order to solve the above linear system, the terms H'_n , $\partial\hat{r}/\partial\mathbf{n}$ and $\partial\hat{\theta}/\partial\mathbf{n}$ need to be evaluated first.

The linear system can be expressed in a matrix form as $AX = B$, where

$$X = [a_0, \dots, a_N, b_1, \dots, b_N]^T, \quad (4.16)$$

$$B = [P(x_1, y_1), \dots, P(x_M, y_M), P_{\mathbf{n}}(x_1, y_1), \dots, P_{\mathbf{n}}(x_M, y_M)]^T, \quad (4.17)$$

and $A = (A_1, A_2)^T$, A_1 corresponds to P and A_2 corresponds to normal derivative $P_{\mathbf{n}}$. One could find X by minimizing $\|AX - B\|^2$, where $\|\cdot\|$ is the standard L^2 norm. During the numerical study, it is observed that although some regularization methods may be needed to improve the stability of the system for large N , they are not necessary for relatively small N . In the current work, N is initialized within a given range of 0 – 20. The reconstructed solutions for various N are compared with the input acoustic solutions of the inverse problem. The total error at all the input points is then computed for each N . The optimum N within the given range is determined from the minimum overall error. Finally, the reconstruction of the entire acoustic field is carried out using the optimum N .

It is worth a mention that without the inclusion of the pressure gradient to the input of the inverse methods the reconstructed solution cannot be unique if only $P|_{\Gamma_1}$ is specified. For example, if Ω_{in} is the unit disk centered at the origin, we assume that all the acoustic sources are enclosed by the unit circle, and the boundary Γ_1 is defined as $\Gamma_1 = \{(x, y) \mid \hat{x}^2 + \hat{y}^2 = \hat{r}^2, \hat{y} > 0\}$. That is, Γ_1 is the upper half boundary of an ellipse, \hat{r} is chosen large enough so that the ellipse will include all the acoustic sources. The acoustic pressure for $\hat{\theta} \in [0, \pi]$ should satisfy Equation (4.7). It is well known that a_n and b_n are not unique from Fourier analysis. Especially P always has Fourier cosine expansion for $\hat{\theta} \in [0, \pi]$, namely one can set $b_1 = b_2 = \dots = 0$. In any case, it is impossible to predict solutions for $\hat{\theta} \in (\pi, 2\pi)$.

Furthermore, it should be pointed out that even though our formula are derived for the uniform flow $\mathbf{u}_0 = u_0 \mathbf{i} = (u_0, 0)$, it is very easy to modify it for a general case $\mathbf{u}_0 = (u_0, v_0)$. In that case, by rotating the coordinates for an angle α , where α in the range of $(0, 2\pi)$ is given by $(u_0, v_0) = \sqrt{u_0^2 + v_0^2}(\cos \alpha, \sin \alpha)$, the pressure $P(x, y)$ in the frequency domain with angular frequency ω can then be calculated by

$$P(x, y) = \exp(ikM\hat{x}\beta^{-2}) \sum_{n=0}^{\infty} (a_n \cos n\hat{\theta} + b_n \sin n\hat{\theta}) H_n(k\hat{r}/\beta), \quad (4.18)$$

where

$$\begin{cases} M_a &= \sqrt{u_0^2 + v_0^2}/c, \\ \hat{x} &= (x \cos \alpha + y \sin \alpha)/\beta = \hat{r} \cos \hat{\theta}, \\ \hat{y} &= -x \sin \alpha + y \cos \alpha = \hat{r} \sin \hat{\theta}, \\ \hat{r} &= \sqrt{\hat{x}^2 + \hat{y}^2}. \end{cases} \quad (4.19)$$

4.2.2 Multiple Frequencies

When the scattering problem involves multiple frequencies, the FFT can be used to decompose the problem into the linear combinations of several dominant frequencies. Since the AIBM is a frequency domain method, the reconstruction of the sound pressure for each frequency component needs to be individually calculated. A superposition of the contribution from each frequency gives the total sound pressure in the frequency domain. The reconstructed sound pressure field in the time domain is obtained by an inverse FFT. The details of the solution of the AIBM are explained in the following steps:

Step 1: Input Acoustic Data.

The input acoustic data are obtained from measurements, or from numerical solutions of CAA calculation on a circle with radius r_0 for $0 \leq t \leq t_0$, where t_0 is large enough so that the solution asymptotically decays at large t . Assuming the dimensionless speed of sound $c = 1$, then the wave number for each frequency $k_j = \omega_j$. The fast Fourier transform is then used to decompose the solution in terms of its frequencies ω_j , *i.e.*,

$$p(x, y, t) = \sum_{j=1}^J \exp(i\omega_j t) P_j(x, y) \quad (4.20)$$

with $P_j(x, y)$ satisfies the Helmholtz equation

$$\nabla^2 P_j + \omega_j^2 P_j = 0, \quad x \in \Omega = R^2 \setminus B(0, r_1) \quad (4.21)$$

where $B(0, r_1)$ is a circle of radius r_1 , centered at the origin. The boundary condition P_j on the circle of r is given as the input acoustic data for the AIBM. If the polar coordinates are used in a two-dimensional configuration, the solution of Equation (4.21), which also satisfies the radiation condition, can be written as

$$P_j(x, y) = \sum_{l=0}^{\infty} (a_{j,n} \cos n\theta + b_{j,n} \sin n\theta) H_n(\omega_j r) \quad (4.22)$$

where H_n is the n th-order Hankel function of the second kind.

Step 2: Determination of the coefficients $a_{j,n}$ and $b_{j,n}$.

The numerical solution of Equation (4.22) is obtained by replacing infinite summation in Equation (4.22) by a finite summation, *i.e.*,

$$P(x, y) \approx a_{j,0} H_0(\omega_j r) + \sum_{n=1}^{N_j} (a_{j,n} \cos n\theta + b_{j,n} \sin n\theta) H_n(\omega_j r) \quad (4.23)$$

where N_j is a suitable integer for each frequency component. Because of the broadband nature of the problem, it is necessary to accurately determine the coefficients $a_{j,n}$ and $b_{j,n}$ for each frequency ω_j . As in the case for single frequency, these coefficients are determined by matching the assumed form of the solution to the input acoustic data in the frequency domain, *i.e.*, $P(x, y)$ and $P_{\mathbf{n}}$, on the circle of radius r_0 . The choice for N_j must be carefully chosen to ensure both the accuracy and stability as discussed in [38]. Apparently, the accuracy of the solution naturally requires a large value of N_j . However, a large N_j can also result in computational instability. For any given ω_j , a mathematical analysis yields

$$H_n(\omega_j r) = \left(\frac{2n}{e\omega_j r} \right)^n, \quad n \rightarrow \infty \quad (4.24)$$

When $\omega_j r$ is small, $H_n(\omega_j r)$ is very large when $n \approx (e\omega_j r/2)$. A small perturbation in the input acoustic data may result in large variations in $a_{j,n}$ and $b_{j,n}$. Hence the value for

N_j has to be restricted for the stability of the numerical solution. In the current study, the restriction is given as $N_j \leq [\omega_j r_0] + 1$, where $[z]$ is the greatest integer less than or equal to z . In the current work, the value of N_j is chosen as

$$N_j = \min\{N_j \leq [\omega_j r_0] + 1, 30\} \quad (4.25)$$

with considerations of numerical stability and computational efficiency.

For any given ω_j and N_j , the coefficients $a_{j,n}$ and $b_{j,n}$ are determined for each frequency component of $1 \leq j \leq J$ and $0 \leq n \leq N_j$ based on the acoustic input provided on the circle of r .

Step 3: Prediction of sound radiation $p(r, \theta, t)$.

For any given $x \in B(0, r_2)$ with polar coordinate (r, θ) , and $t \in [0, t_0]$, with r_2 not far away from r_1 ,

$$p(r, \theta, t) \sim \sum_{j=1}^J \sum_{l=0}^{N_j(x)} (a_{j,l} \cos l\theta + b_{j,l} \sin l\theta) e^{i\omega_j t} H_l(\omega_j |x|), \quad (4.26)$$

where the upper limit $N_j(x)$ is chosen as

$$N_j(x) = \min\{[\omega_j |x|] + 1, [\omega_j r_0] + 1, 30\}. \quad (4.27)$$

It is noticed that $N_j(x)$ can't be larger than $([\omega_j r_0] + 1, 30)$ due to the value of $N_j(x)$ used in determining the coefficients $a_{j,n}$ and $b_{j,n}$. The additional restriction $[\omega_j r] + 1$ is added for a similar reason mentioned earlier in the discussion of Equation (4.24). Without the additional restriction on N_j , the solution $p(r, \theta, t)$ may become unstable.

4.3 Numerical Examples and Discussions

In this section, the AIBM is first verified for sound source propagations in a uniform flow. The method's effectiveness and capability for aeroacoustic applications are then demonstrated by airfoil noise and sound scattering problems.

4.3.1 Monopole in a Uniform Flow

The AIBM is first applied to a stationary monopole source placed in a uniform flow. A schematic diagram of the source in a uniform flow of $M_a = 0.5$ in the $+x$ direction is shown in Figure 4.2. The two circular arc segments are the locations of the acoustic input and the angle γ is a measure of the dimensionless distance between the two segments, with $\gamma = \pi$ being the farthest, *i.e.*, the segments are at the opposite sides of the control surface. The units used for r and θ are the meter and the radian, respectively. The monopole is placed at $(1\text{m}, 0.2\pi)$ in the polar coordinates. The wavenumber and intensity of the monopole is given as $k = 2\text{m}^{-1}$ and $A_0 = 0.001\text{m}^2/\text{s}$. The control surface is considered here as the circle of radius $r = 2\text{m}$. The analytical complex potential for the monopole is given by Dowling and Ffowcs Williams [53] as

$$\Phi(x, y, t) = A_0 \frac{i}{4\beta} \exp[i(\omega t + M_a k x / \beta^2)] H_0 \left(\frac{k}{\beta} \sqrt{\frac{x^2}{\beta^2} + y^2} \right) \quad (4.28)$$

The analytical acoustic pressure and its normal derivative, over the two circular arc segments, can be derived from Equation (4.28) and are used as the input for the inverse calculation. The polar coordinates of the starting and ending points of the two segments are $(10\text{m}, 0)$, $(10\text{m}, 0.1\pi)$ and $(10\text{m}, \gamma)$, $(10\text{m}, 0.1\pi + \gamma)$, respectively. Ten uniformly spaced grid points are used on each of the segments. With $\beta = \pi$, the far-field directivity from

the AIBM is calculated and compared with those from the analytical solution and the FW-H integral equation in Figure 4.3. The results show excellent agreement among the three methods. It is important to point out that the arc length of the each input segment for the AIBM is only about 1/20 of the circumference of the circle ($r = 10\text{m}$), that is used as the FW-H surface. The reconstructed acoustic pressure contours from the AIBM and the analytical solution are shown in Figure 4.4. As it is indicated, an accurate reconstruction of the radiated field is achieved on and outside the control surface using the AIBM.

As it has been shown in the work of Yu *et al.* [39,40], though an accurate reconstruction can be obtained from the input given over an open surface, the AIBM becomes less effective when the input segments become clustered. As a general rule, the more scattered the input segments around a sound source, the more accurate the reconstructed acoustic solution. Since the choices of the input segments are limited by the accessibility and practicality of the acoustic measurement in the radiated field, some regularization techniques may be needed to improve the effectiveness of the AIBM when the input locations are not scattered far enough around the sound source.

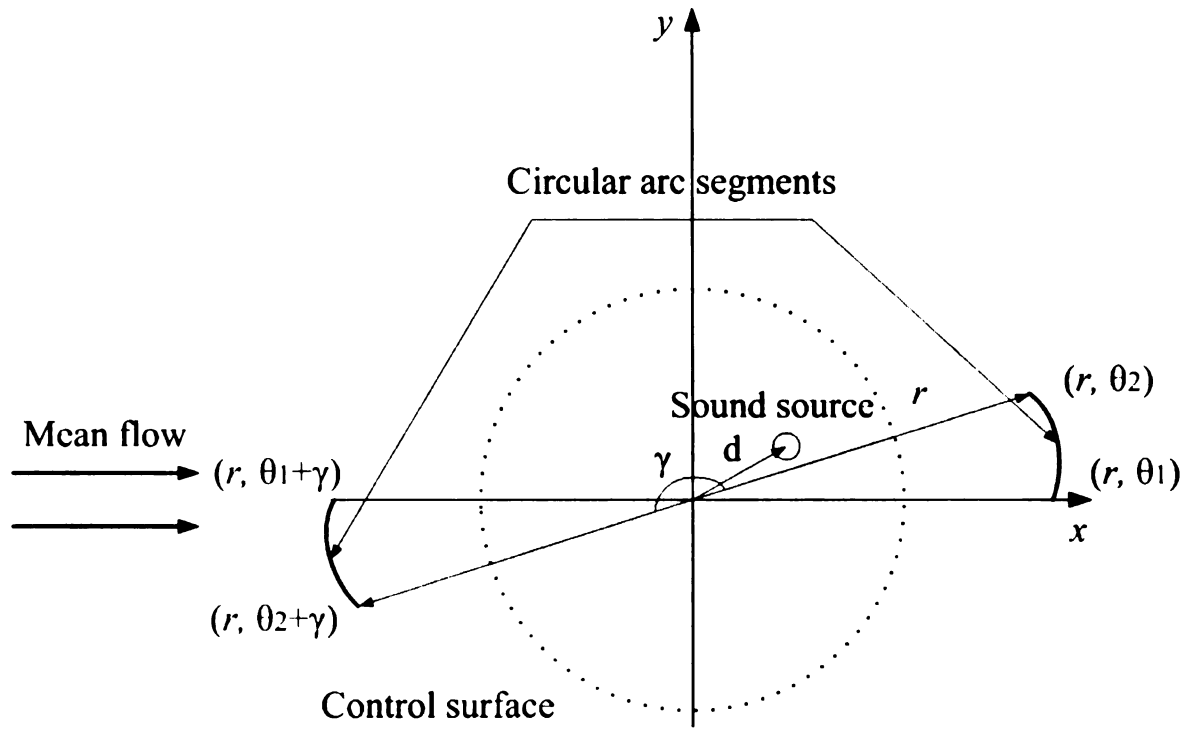


Figure 4.2: Schematic diagram of a monopole radiation in a uniform flow and locations of acoustic measurements.

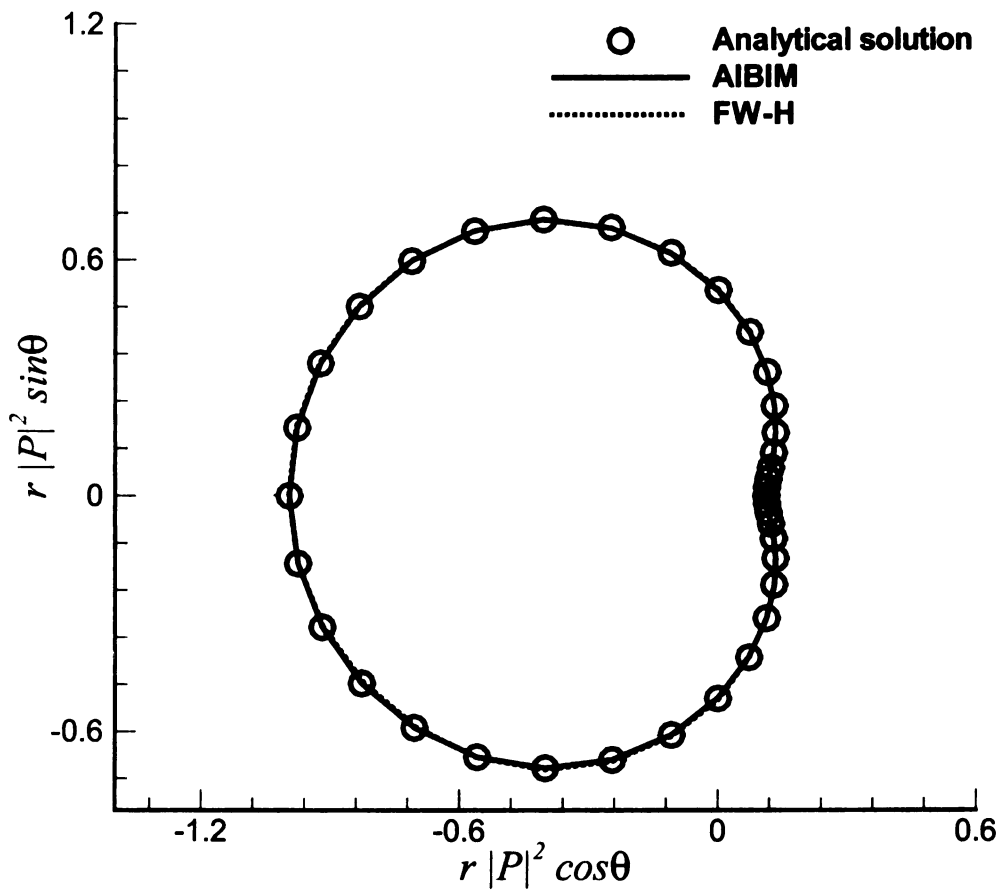
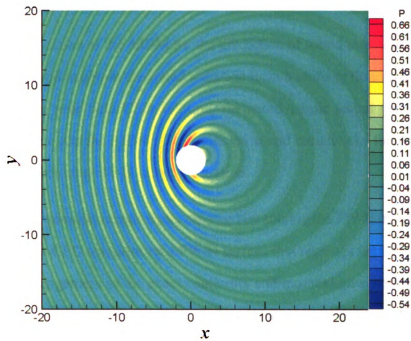
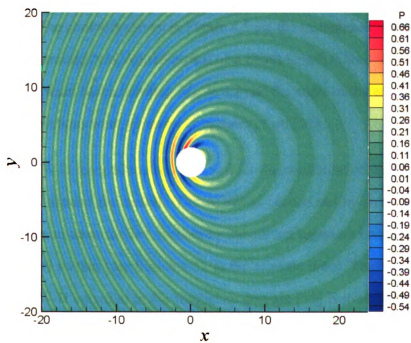


Figure 4.3: Far-field directivity ($r = 100\text{m}$) comparison of a monopole radiation in a $M_a = 0.5$ flow.



(a) Analytical solution



(b) AIBM

Figure 4.4: Pressure contours of a monopole radiation in a $M_a = 0.5$ flow.

4.3.2 Sound Radiation by a Flow Around a NACA Airfoil

After the above verification of the AIBM for the prediction of sound radiation in a uniform flow, the method is used to obtain the sound radiation from a uniform flow around a NACA airfoil. Based on the near field CFD solution, the aerodynamic sound generated in the far-field is calculated using the AIBM. The predicted sound radiation of the AIBM is then compared with that from the FW-H integral equation.

The far-field acoustic solution is commonly obtained by solving the FW-H integral equation based on the unsteady CFD solutions on a FW-H surface that encloses the airfoil. The FW-H equation is a rearrangement of the exact continuity and momentum equations to a wave equation with source contributions from the monopole, dipole and quadrupole terms. The contribution of the quadrupole term, the Lighthill stress tensor, is neglected since the FW-H surface, as indicated in Figure 5 for the current study, is placed outside of all regions where the stress tensor is significant. The quadrupole contribution is in fact included by the surface sources. The contours shown in Figure 4.5 are the instantaneous sound pressure contours of the flow around NACA0018 airfoil of a chord length 0.3m. As also shown in Figure 4.5, the free-stream Mach number, M_a , is 0.2 and the angle of the attack is 20° . The details of the CFD solutions were given by Greschner *et al.* [54].

The AIBM and the FW-H integral method are used for the prediction of the far-field sound radiation by the flow around the airfoil. The AIBM is carried out by using the unsteady pressure solution over an open surface, formed by the curved segments I and II or segments III and IV of the FW-H surface (see Figure 4.5), as the acoustic input. The two-dimensional formulation of the FW-H equation in the frequency-domain [55] is used with the input of the unsteady pressure and velocity solutions over the entire FW-H surface.

The comparison of the far-field directivity obtained from the AIBM and the FW-H integral method is shown in Figure 4.6. As can be seen in Figure 4.6, the results of the AIBM based

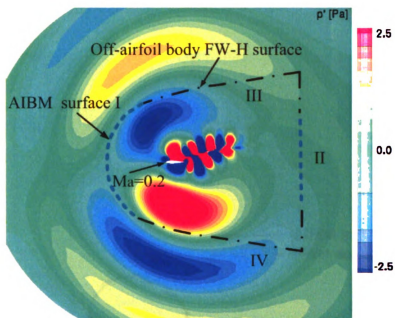


Figure 4.5: Instantaneous pressure perturbations of the flow around the NACA 0018 airfoil along with the location of the FW-H surface.

on the inputs of two chosen open surfaces agree reasonably well with that of the FW-H integral method.

In order to have an overview of the sound propagation in the far-field, the sound pressure contour plots from the AIBM and the FW-H method are shown in Figure 4.7. It is noted that the radius of the control surface used for this problem is $r = 3\text{m}$, which is ten times of the chord of the airfoil. It should also be pointed out that the FW-H surface used in the study, though not a circular shape, is enclosed in the control surface. The close agreement among the three contour plots indicates that the AIBM is capable to effectively obtain the radiated sound field based on the acoustic input from an open surface. The method, therefore, has a potential application for the far-field sound reconstruction for problems where a closed FW-H surface is not possible.

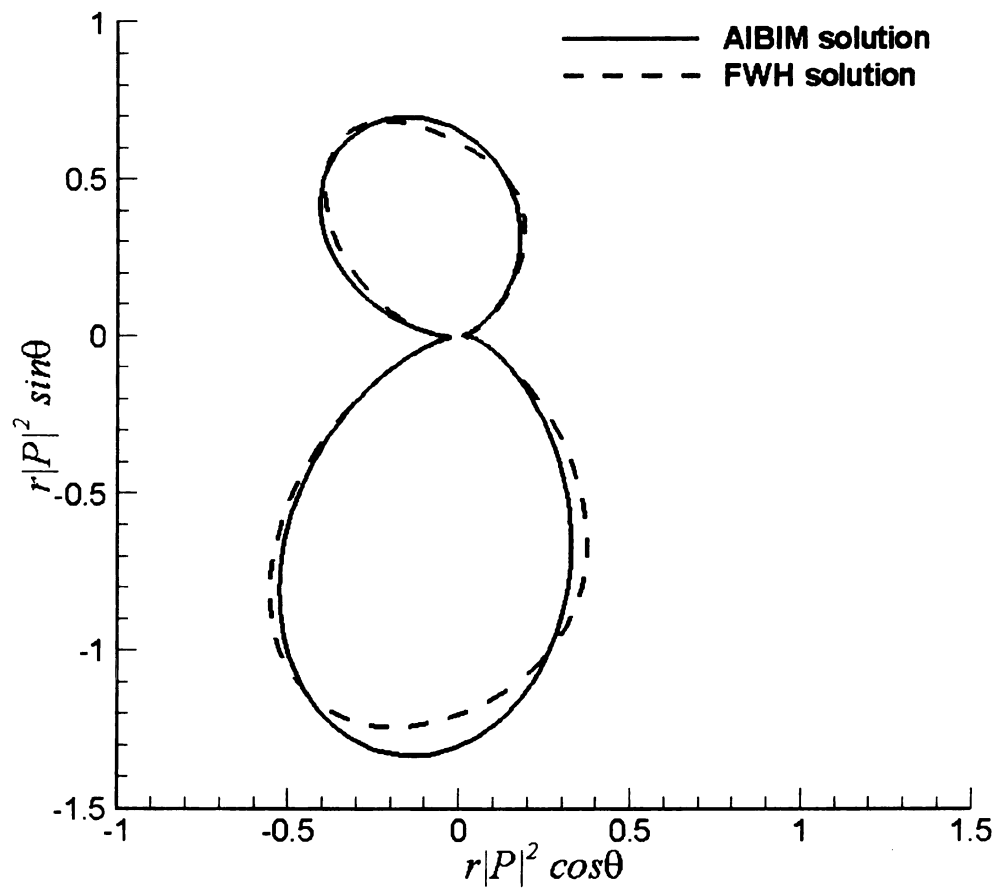
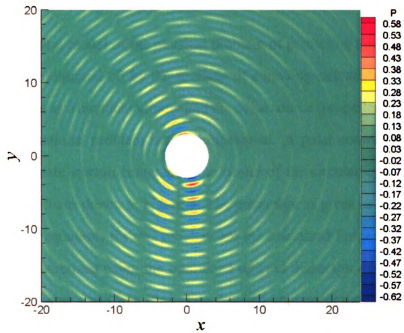
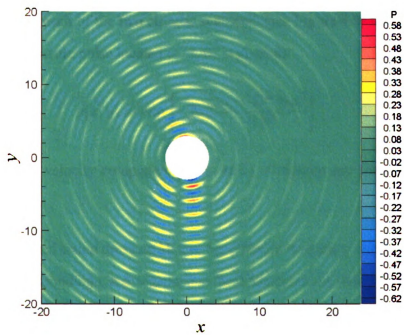


Figure 4.6: Far-field directivity ($r = 100\text{m}$) of the flow around the NACA 0018 airfoil.



(a) FW-H



(b) AIBM

Figure 4.7: Pressure contours of the sound propagation generated by the flow around the NACA 0018 airfoil.

4.3.3 Sound Scattering

This example is an ideal model of the physical problem of predicting the sound field generated by a propeller scattered off by the fuselage of a moving aircraft. In the model, the fuselage is considered as a circular cylinder and the noise source (propeller) as a line source such that the computational problem is two-dimensional. A polar coordinate system and the Cartesian coordinate system centered at the center of the circular cylinder of the dimensionless radius 0.5 are shown in Figure 8. The mean flow is given as Mach number of zero. The governing equations for this problem are the linearized Euler equations (LEE). The equations are discretized using the optimized upwind dispersion-relation-preserving scheme (DRP) of Zhuang and Chen [56]. The detailed implementations of the boundary and initial conditions are given by Chen and Zhuang [57], in which the numerical solution (CAA solution) was also verified by the analytical solution. In the current study, the CAA solution is used as the acoustic input for the AIBM. The input is given at forty uniformly distributed points on each of the two circular segments (see Figure 4.8) with the radius of 6.125. The initial pressure pulse located at (4, 0) is given as

$$p(x, y) = \exp \left[-\ln 2 \frac{(x-4)^2 + y^2}{0.2^2} \right] \quad (4.29)$$

and the perturbation velocity components in x - and y -directions are considered as zero, $u = v = 0$.

The results of predicted sound pressure history for different frequency ranges are also compared with the corresponding CAA solutions at three locations are shown in Figures 4.10-4.12, respectively. As it is indicated that the accuracy of the predicted solution improves significantly as all the dominant frequencies are included in the AIBM calculation. In terms of peak pressure values and locations of the incident and reflected waves, excellent agreements between the two methods, AIBM and CAA, are demonstrated. The oscillations at

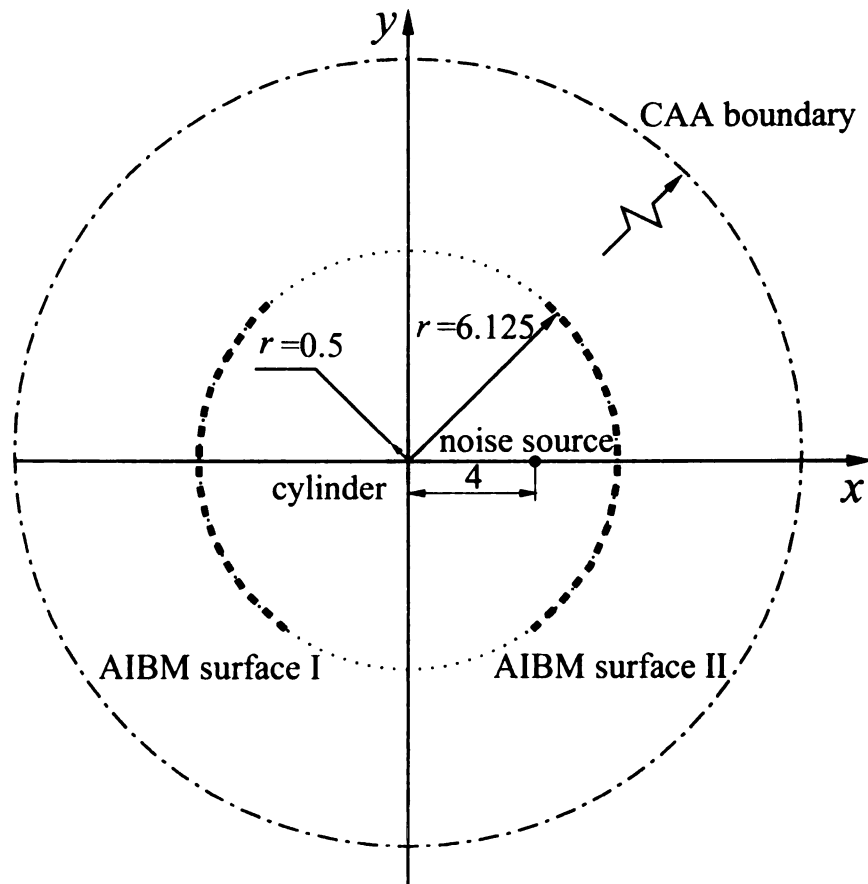


Figure 4.8: Schematic diagram of the sound scattering by a cylinder.

the lower amplitudes are due to a relatively large value of N . As it is discussed in Section II, the number of summations, N (Equation (4.8)), needs to be reduced as the radius r decreases to provide a converged solution. The pressure contour plots from the CAA calculation and the AIBM are compared in Figures 4.13-4.15 for various times. The results of these contour plots demonstrate that the AIBM can effectively predict the propagations of both the incident and reflected sound waves.

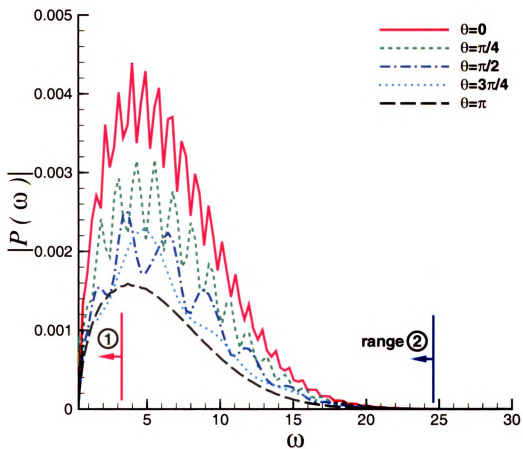
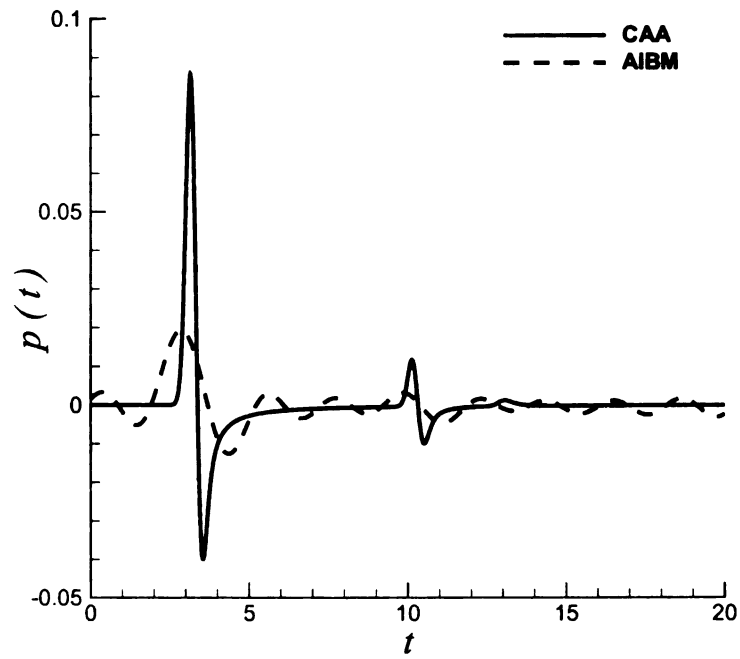
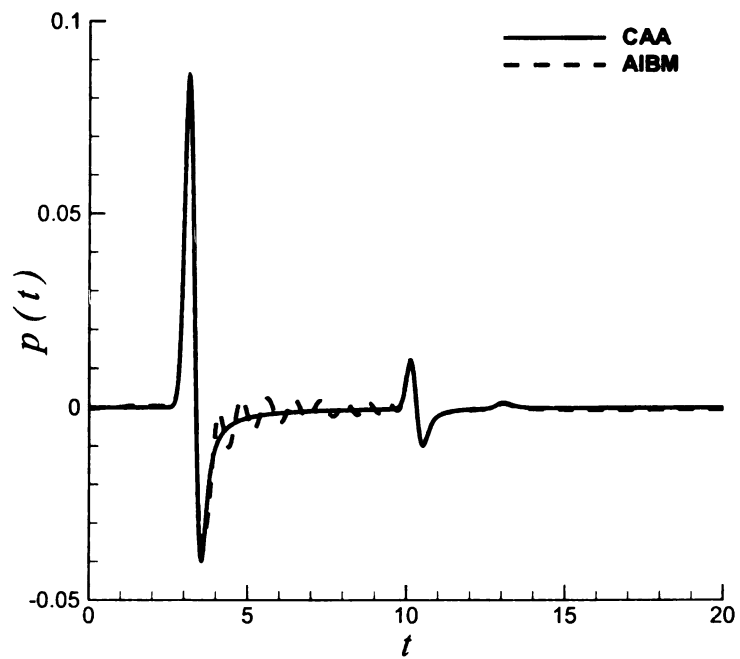


Figure 4.9: Frequency spectrum for the sound scattering, $r = 6.125$.

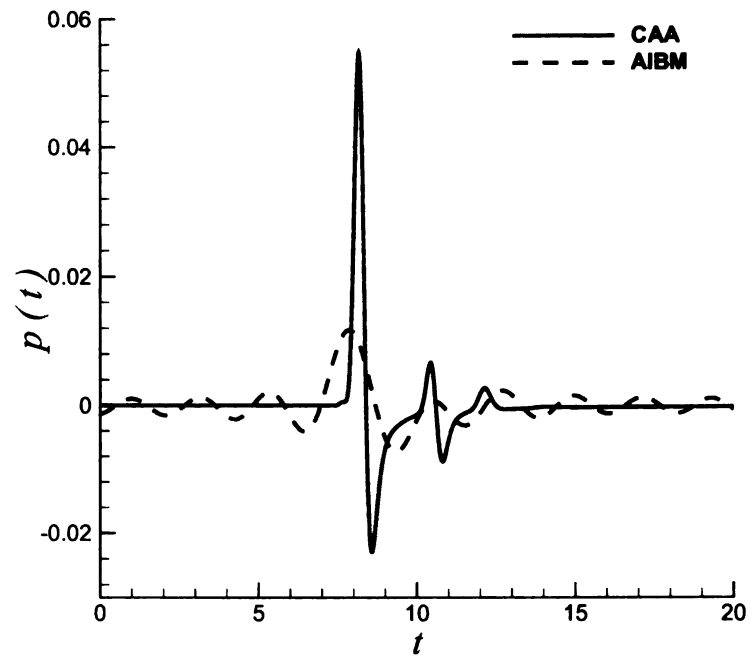


(a) $\omega = 0.307 - 3.07$

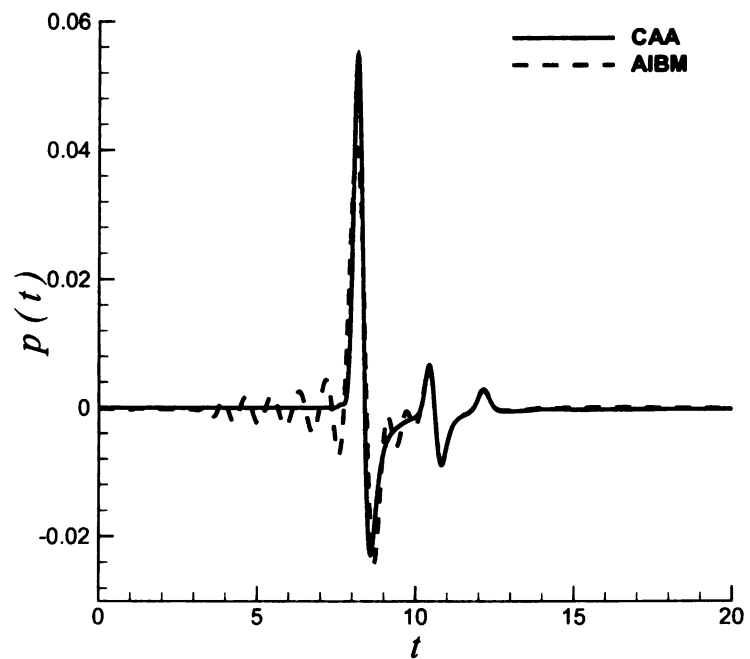


(b) $\omega = 0.307 - 24.56$

Figure 4.10: Pressure time history reconstruction with different frequency range at $r = 7.25$ and $\theta = 0^\circ$.

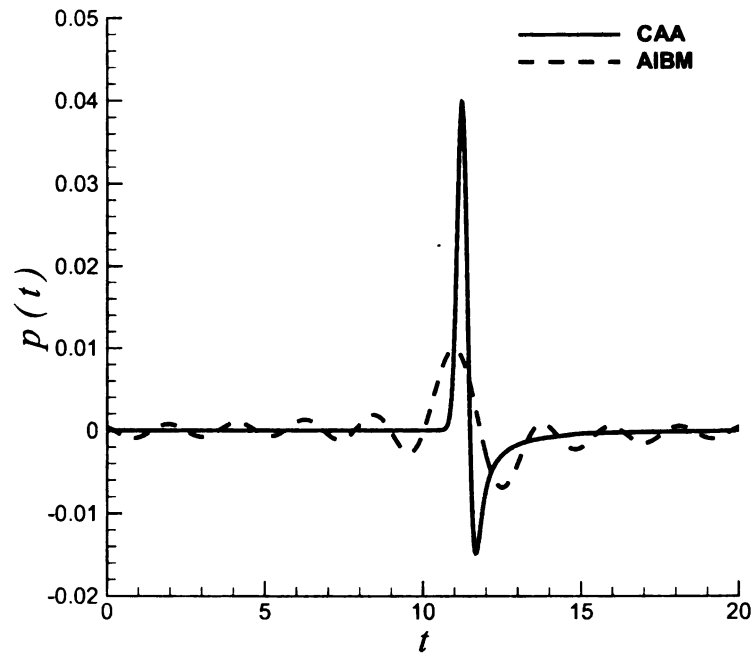


(a) $\omega = 0.307 - 3.07$

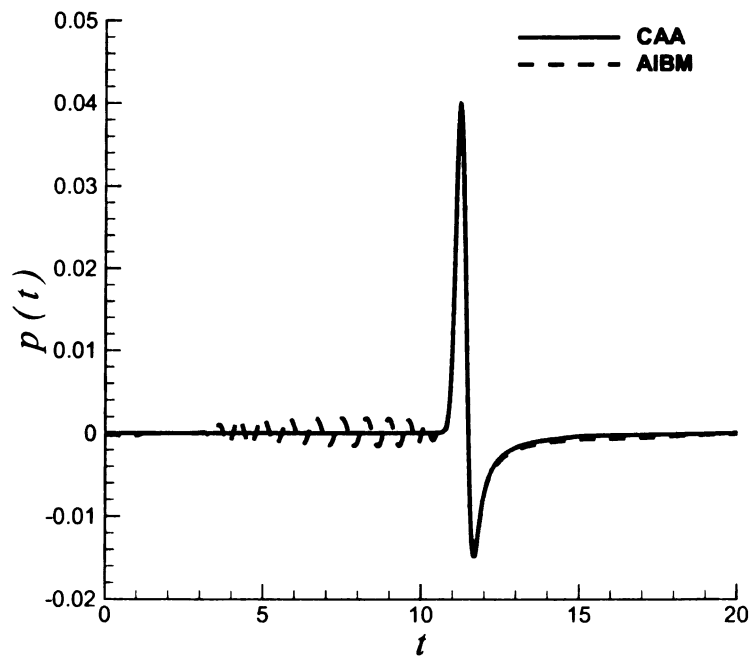


(b) $\omega = 0.307 - 24.56$

Figure 4.11: Pressure time history reconstruction with different frequency range at $r = 7.25$ and $\theta = 90^\circ$.



(a) $\omega = 0.307 - 3.07$



(b) $\omega = 0.307 - 24.56$

Figure 4.12: Pressure time history reconstruction with different frequency range at $r = 7.25$ and $\theta = 180^\circ$.

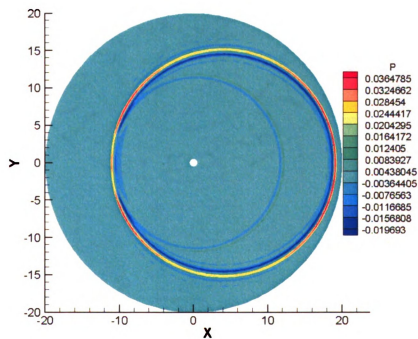
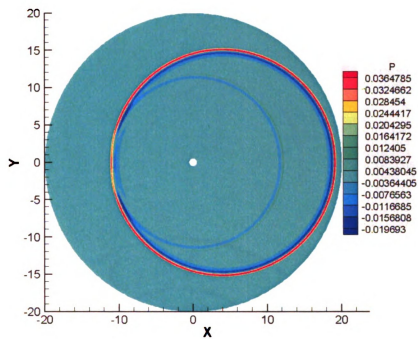


Figure 4.13: Instantaneous pressure contours of the sound scattering at $t=15$: CAA (top), AIBM (bottom).

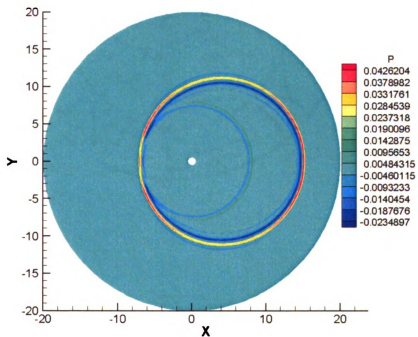
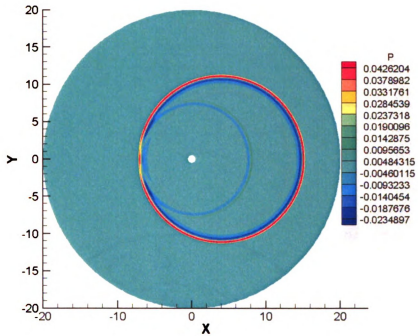


Figure 4.14: Instantaneous pressure contours of the sound scattering at $t=11$: CAA (top), AIBM (bottom).

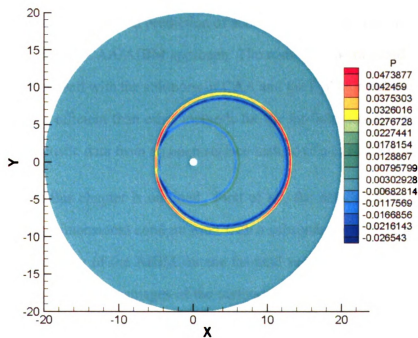
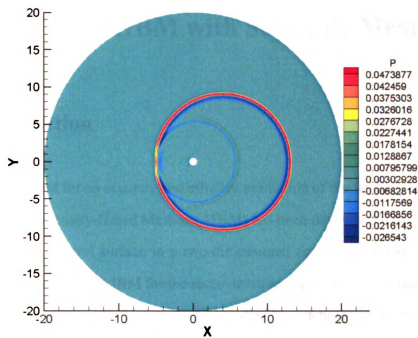


Figure 4.15: Instantaneous pressure contours of the sound scattering at $t=9$: CAA (top), AIBM (bottom).

Chapter 5 3D AIBM with Subsonic Mean Flow

5.1 Introduction

Motivated by the need for an accurate and efficient prediction of the far-field acoustic radiation, an Acoustic Intensity-Based Method (AIBM) has been developed based on acoustic input from an open control surface in a two-dimensional configuration [38–40]. In this chapter, a three-dimensional AIBM for the reconstruction and prediction of radiated acoustic fields is developed [41–43]. The method is verified by examples of the propagation of multiple acoustic sources in a uniform flow and the acoustic scattering of a time dependent source by a sphere. The effectiveness of AIBM in aeroacoustic applications is demonstrated by the accurate and efficient prediction of acoustic radiations from an axisymmetric duct intake using a hybrid CAA/AIBM approach. The results of the radiated acoustic field from the AIBM agree well with the solutions of CAA and the FW-H integral equation. The AIBM is much more efficient than other methods for the far-field acoustic prediction and can use the input acoustic data from an open surface instead of a closed FW-H surface.

The organization of this chapter is outlined. First of all, the details on the extension of the AIBM to a three-dimensional configuration with a subsonic uniform flow are derived. Furthermore, the accuracy of the AIBM for the far-field acoustic prediction is shown by numerical examples and the advantages of the method with respect to both efficiency and choice of locations for the acoustic input are demonstrated.

5.2 Mathematical Formulations

Let Γ be the boundary of a sphere containing all acoustic sources, and Γ_1 be a (usually very small) part of Γ . In the AIBM, both the acoustic pressure P and its collocated normal derivative $\partial P/\partial \mathbf{n}$ on Γ_1 are considered as the input acoustic data. In practice, P and $\partial P/\partial \mathbf{n}$ are given at a finite number of points $(x_j, y_j, z_j) \in \Gamma_1, j = 1, M$.

5.2.1 Basic Formulation for AIBM

Assuming that the mean flow is in z direction and employing the standard separation of variables in terms of spherical coordinates, the general solution for the Helmholtz equation can be approximated by a linear combination of basis functions

$$P(r, \theta, \phi) = \exp(ikM_a \hat{r} \cos \hat{\phi} \beta^{-2}) \sum_{n=0}^{\infty} \sum_{m=0}^n (a_{nm} \cos m\hat{\theta} + b_{nm} \sin m\hat{\theta}) P_n^m G_n(k\hat{r} \beta^{-2}), \quad (5.1)$$

where M_a is the free-stream Mach number, $\beta = \sqrt{1 - M_a^2}$, k is the wave number, $P_n^m = P_n^m(\cos \hat{\phi})$ is the associated Legendre polynomial and G_n represents the generalized Hankel function or spherical Hankel function. The coordinates $(\hat{r}, \hat{\theta}, \hat{\phi})$ are defined as the modified spherical coordinates from Cartesian coordinates (x, y, z) in the physical domain.

Let $(\hat{x}, \hat{y}, \hat{z}) = (\beta x, \beta y, z)$, then

$$\hat{x} = \hat{r} \sin \hat{\phi} \cos \hat{\theta}, \quad \hat{y} = \hat{r} \sin \hat{\phi} \sin \hat{\theta}, \quad \hat{z} = \hat{r} \cos \hat{\phi}, \quad \hat{r} = \sqrt{\hat{x}^2 + \hat{y}^2 + \hat{z}^2}. \quad (5.2)$$

Differentiating both sides of Equation (5.1) with respect to the unit normal $\mathbf{n} = (n_x, n_y, n_z)$ and using the chain rule, we have the formula for normal derivative of P ,

$$\frac{\partial P}{\partial \mathbf{n}}(r, \theta, \phi) = \frac{\partial P}{\partial \hat{r}} \frac{\partial \hat{r}}{\partial \mathbf{n}} + \frac{\partial P}{\partial \hat{\theta}} \frac{\partial \hat{\theta}}{\partial \mathbf{n}} + \frac{\partial P}{\partial \hat{\phi}} \frac{\partial \hat{\phi}}{\partial \mathbf{n}}. \quad (5.3)$$

Note that

$$\frac{\partial \hat{\theta}}{\partial \mathbf{n}} = \frac{1}{\hat{r} \sin \hat{\phi} \cos \hat{\theta}} \left(\beta n_y - \hat{r} \cos \hat{\phi} \sin \hat{\theta} \frac{\partial \hat{\phi}}{\partial \mathbf{n}} - \sin \hat{\phi} \sin \hat{\theta} \frac{\partial \hat{r}}{\partial \mathbf{n}} \right) \quad (5.4)$$

and

$$\frac{\partial \hat{\phi}}{\partial \mathbf{n}} = \frac{1}{\hat{r} \sin \hat{\phi}} \left(\cos \hat{\phi} \frac{\partial \hat{r}}{\partial \mathbf{n}} - n_z \right). \quad (5.5)$$

As it is shown in the above two equations, there are singularities when $\hat{\phi} = 0$ and π or $\hat{\theta} = \pi/2$ and $3\pi/2$. These singularities lead to computational difficulties. To eliminate these poles, an improved formulation is derived in the next section.

5.2.2 Improved Formulation for AIBM

In this section, the coordinate system will be converted from spherical coordinates to Cartesian coordinates, and the singularity terms will be eliminated after the multiplication of suitable trigonometric functions.

First, $\cos m\hat{\theta}$ and $\sin m\hat{\theta}$ can be expressed as

$$\begin{cases} \cos m\hat{\theta} = \frac{1}{2}(e^{im\hat{\theta}} + e^{-im\hat{\theta}}) = \frac{1}{2\hat{r}^m \sin^m \hat{\phi}} [(\hat{x} + i\hat{y})^m + (\hat{x} - i\hat{y})^m], \\ \sin m\hat{\theta} = \frac{1}{2i}(e^{im\hat{\theta}} - e^{-im\hat{\theta}}) = \frac{1}{2i\hat{r}^m \sin^m \hat{\phi}} [(\hat{x} + i\hat{y})^m - (\hat{x} - i\hat{y})^m]. \end{cases} \quad (5.6)$$

Substituting the above equations into Equation (5.1), we have

$$P(x, y, z) = \exp(ikM_a \hat{z} \beta^{-2}) \sum_{n=0}^{\infty} \sum_{m=0}^n [a_{nm} \xi_m - ib_{nm} \eta_m] Q_n^m(\hat{z} \hat{r}^{-1}) G_n(k\hat{r} \beta^{-2}) / (2\hat{r}^m), \quad (5.7)$$

where

$$\xi_m = (\hat{x} + i\hat{y})^m + (\hat{x} - i\hat{y})^m, \quad \eta_m = (\hat{x} + i\hat{y})^m - (\hat{x} - i\hat{y})^m, \quad (5.8)$$

and $Q_n^m = P_n^m / \sin^m \hat{\phi}$. From the expression for P_n^m , we note that

$$Q_n^m(w) = \frac{(-1)^{m+n}}{2^n n!} \frac{d^{m+n}}{dw^{n+m}} (1-w^2)^n \Big|_{w=\hat{z}/\hat{r}},$$

which has no singularity. Therefore, Equation (5.7) is an improved form of the general solution of the Helmholtz equation. The corresponding normal pressure derivative can be derived as

$$\frac{\partial P}{\partial \mathbf{n}}(x, y, z) = \frac{\partial P}{\partial \hat{x}} \beta n_x + \frac{\partial P}{\partial \hat{y}} \beta n_y + \frac{\partial P}{\partial \hat{z}} n_z. \quad (5.9)$$

5.2.3 Simplified 2.5D Formulation for AIBM

Axisymmetric problems are sometimes considered as 2.5D problems, *e.g.*, acoustic modes propagation in an axisymmetric duct intake with an axisymmetric mean flow. In this section, we are going to simplify the 3D improved formulation into a 2.5D formulation. Let m be the azimuthal mode, and assume that the mean flow is along the z direction. If θ is specified in Equation (5.7), for example $\theta = 0$ ($\xi_m = 2\hat{x}^m, \eta_m = 0$), the equation can be simplified on $x - z$ plane as

$$P(x, 0, z) = \exp(ikM_a \hat{z} \beta^{-2}) \sum_{n=0}^{\infty} \sum_{m=0}^n a_{nm} \hat{x}^m Q_n^m(\hat{z} \hat{r}^{-1}) G_n(k \hat{r} \beta^{-2}) / \hat{r}^m. \quad (5.10)$$

Especially, if the mode m is known in advance, the formula can be further simplified as

$$P(x, 0, z) = \exp(ikM_a \hat{z} \beta^{-2}) \sum_{n=m}^{\infty} a_{nm} \hat{x}^m Q_n^m(\hat{z} \hat{r}^{-1}) G_n(k \hat{r} \beta^{-2}) / \hat{r}^m. \quad (5.11)$$

This is the simplified 2.5D solution of the Helmholtz equation for axisymmetric propagation problems. The normal derivative can be derived based on the above simplified solution as

$$\frac{\partial P}{\partial \mathbf{n}}(x, 0, z) = \frac{\partial P}{\partial \hat{x}} \beta n_x + \frac{\partial P}{\partial \hat{z}} n_z. \quad (5.12)$$

5.2.4 Numerical Implementation

The numerical solutions for Equations (5.1), (5.7), (5.10) and (5.11) are obtained from the following three steps.

Step 1: Instead of using the infinite summation in these equations, the solutions are approximated by a finite summation. Namely, the size of n is suitably restricted. For example, Equation (5.7) is approximated by

$$P_N = \exp(ikM_a \hat{z} \beta^{-2}) \sum_{n=0}^N \sum_{m=0}^n [a_{nm} \xi_m - ib_{nm} \eta_m] Q_n^m(\hat{z} \hat{r}^{-1}) G_n(k \hat{r} \beta^{-2}) / (2 \hat{r}^m). \quad (5.13)$$

The upper limit N must be chosen large enough to accurately reconstruct the acoustic data on the input surface and in the field, but the number should be minimized to reduce the computational costs. N is initialized within a given range of 1-40. The optimum N is determined from the minimum overall error [38].

Step 2: The coefficients a_{nm} and b_{nm} , $0 \leq m \leq n \leq N$ are numerically determined by matching the assumed form of the solution to the input data $P(x_j, y_j, z_j)$ and $\partial P / \partial \mathbf{n}$, $1 \leq j \leq M$. Namely, a linear system of $2M$ equations with a_{nm} and b_{nm} as unknowns must be solved. One obvious requirement is that this system must be overdetermined, which also restricts the size of N . In the paper, the least squares method is used to solve this linear system.

Step 3: For any given field point, including the input points, in a radiated acoustic field, the acoustic pressure can be approximated by Equation (5.13) using the coefficients a_{nm} and b_{nm} obtained from the previous steps. Detailed numerical techniques are described in the earlier publication [38, 39].

5.3 Results and Discussions

5.3.1 Multiple Sources in a Uniform Flow

To verify the accuracy of AIBM in a three-dimensional configuration, acoustic radiation of multiple sources in a uniform flow are studied. A schematic diagram of the sources and their locations is shown in Figure 5.1. The mean flow is in the x -direction with a Mach number of 0.5. The density and the speed of sound of the ambient medium are given as 1.21kg/m^3 and 344m/s , respectively. All the multiple sources radiate with the same angular frequency, $\omega=200\text{Hz}$. The analytical solution for the multiple sources can be obtained by the summation of each point source solution as

$$p(t, x, y, z) = \sum_{j=1}^J p_j(t, x, y, z) \quad (5.14)$$

where p is the acoustic pressure of the radiated field from the multiple sources and p_j is the solution of each point source. The analytical solution of a monopole in a uniform flow is given as [53]

$$p_j = -\rho_0 \left(\frac{\partial \Phi}{\partial t} + u_0 \frac{\partial \Phi}{\partial x} \right) \quad (5.15)$$

with Φ , the velocity potential function, expressed as

$$\Phi(t, x, y, z) = \frac{A_0}{4\pi\hat{r}} \exp[i(\omega t - k(\hat{r} - M_a x)\beta^{-2})] \quad (5.16)$$

where $\beta = \sqrt{1 - M_a^2}$, $\hat{r} = \sqrt{x^2 + \beta^2(y^2 + z^2)}$ and A_0, ω are the strength and the angular frequency of the monopole, respectively.

In the current study, the multiple sources, consisting of two quadrupoles, two dipoles (formed by superposing monopoles) and one monopole, are distributed inside a control

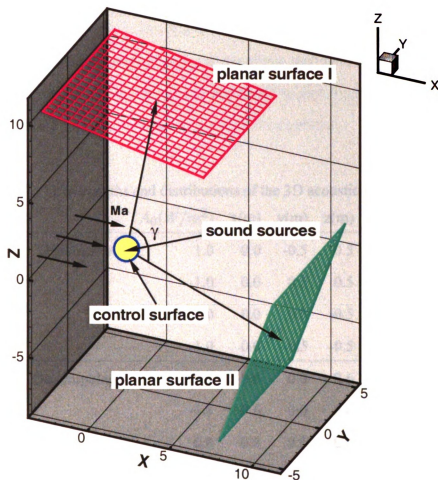


Figure 5.1: Schematic diagram of multiple sources in a uniform flow.

surface of $r = 1\text{m}$. The coordinates and strengths of the sources are given in Table 5.1.

The acoustic pressure and its normal derivative on the two planar surfaces are considered as the input for AIBM (see Figure 5.1) and obtained by using the FFT of the analytical solution of Eq. (5.14). In the current implementation, the distance of each planar surface to the origin is given as 10m and the size of the each surface is 4m by 4m. The angle γ between the surfaces is 120° . Each surface was discretized into 10 by 10 uniform grid lines. The radiated acoustic field for the range of $4\text{m} \leq r \leq 40\text{m}$ is then predicted by AIBM.

Quantitative comparisons of the predicted pressure with the analytical pressure are shown

Table 5.1: The strengths and distributions of the 3D acoustic sources

	$A_0(W/m^2)$	x(m)	y(m)	z(m)
Quadrupole I	1.0	0.0	-0.5	0.5
	-1.0	0.0	0.5	0.5
	1.0	0.0	0.5	-0.5
	-1.0	0.0	-0.5	-0.5
Quadrupole II	0.8	-0.6	0.0	0.6
	-0.8	0.6	0.0	0.6
	0.8	0.6	0.0	-0.6
	-0.8	-0.6	0.0	-0.6
Dipole I	1.1	0.4	0.3	0.1
	-1.1	0.7	-0.1	0.5
Dipole II	0.9	0.3	0.2	-0.2
	-0.9	-0.2	0.5	-0.3
Monopole	1.0	-0.5	-0.5	-0.1

in Figure 5.2 along the x -axis and the y -axis. Excellent agreement of the radiated pressure solutions from the near-field to the far-field is demonstrated in the figure. Contours of the instantaneous pressure are compared with the respective analytical solutions in Figures 5.3. These pressure contour results substantiate that AIBM accurately predicts the radiated acoustic field in a uniform flow of a three-dimensional configuration.

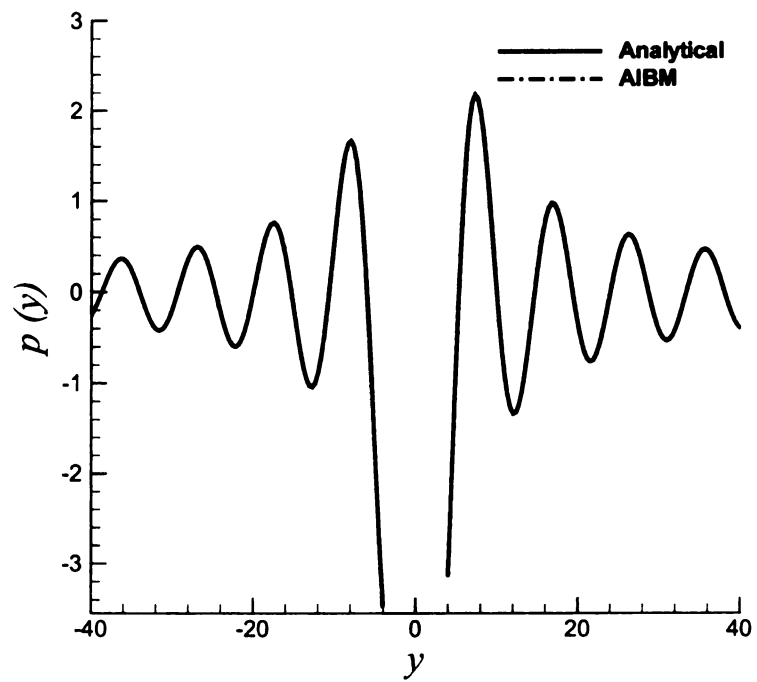
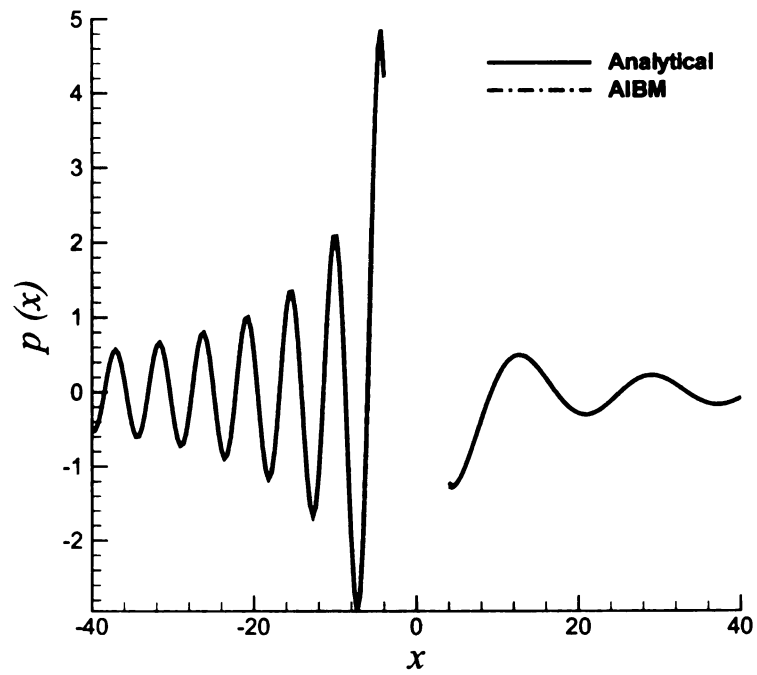


Figure 5.2: Comparisons of the predicted pressure solutions with the analytical solutions: along x-axis (top), along y-axis(bottom).

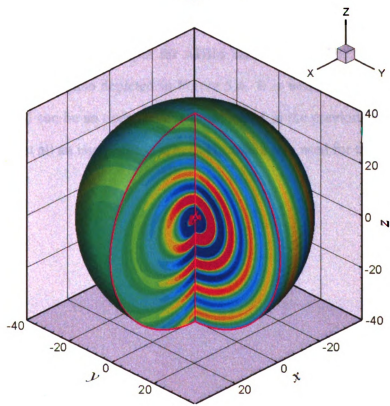
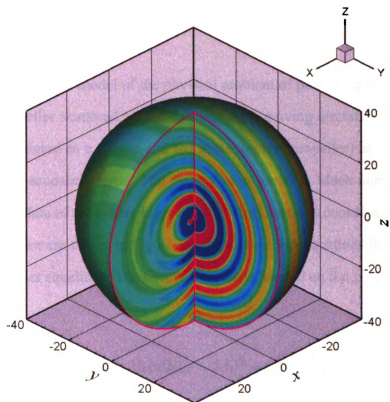


Figure 5.3: 3D instantaneous pressure contours for the sound radiation of multiple sources: Analytical (top), AIBM (bottom).

5.3.2 Acoustic Scattering

This example is an ideal model of the physical problem of predicting the sound field generated by a propeller scattered by the fuselage of a moving aircraft. In the model, the fuselage is considered as a sphere and the noise source (propeller) as a time-dependent, single frequency acoustic source. The mean flow is given as Mach number of zero. The dimensionless radius of the sphere is given as 1. The Cartesian coordinates centered at the center of the sphere are shown in Figure 5.4. The governing equations for this problem are the linearized Euler equations. The acoustic source is located on the x -axis at $x = 1.5$ and expressed as

$$S = 0.01 \exp[-16 \ln 2((x - 1.5)^2 + y^2 + z^2)] \cos(2\pi t) \quad (5.17)$$

The CAA solution [56] verified by the analytical solution of the scattering by a sphere [58] was used as the acoustic input for AIBM calculations. The input surface of $r = \sqrt{x^2 + y^2 + z^2} = 4$ is also depicted in Figure 5.4. It is worth mentioning that the input surface for AIBM can be an open surface as indicated in the previous example. Since the CPU time is not at all an issue here, a spherical surface was used for the sake of simplicity.

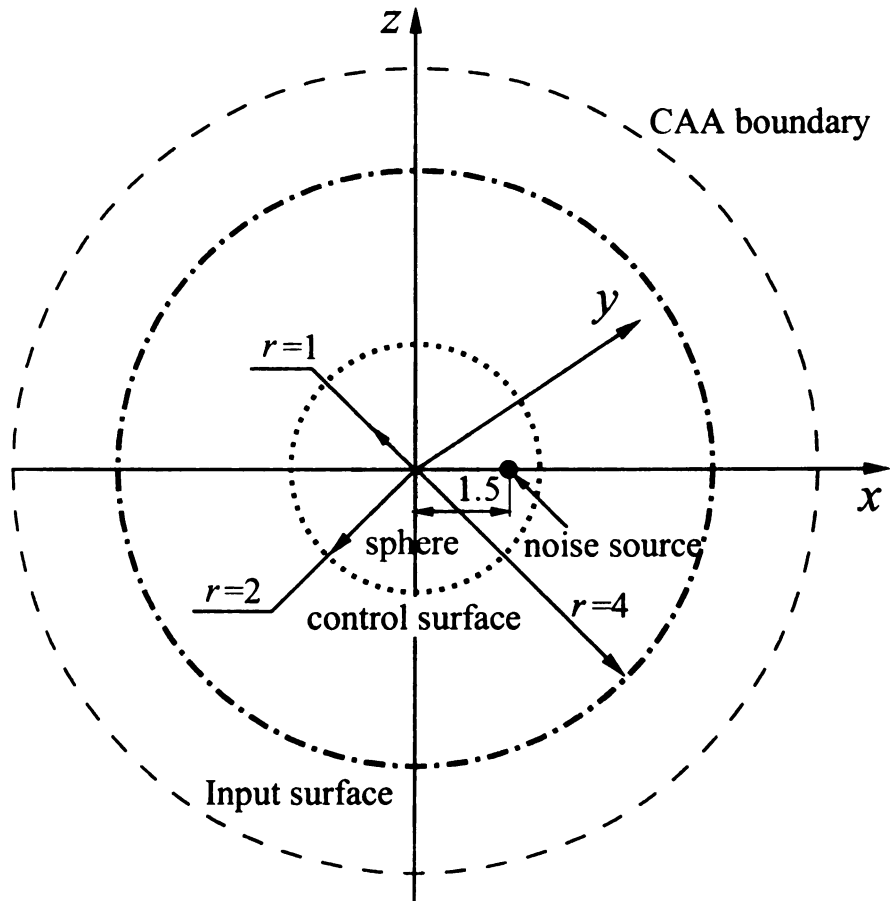


Figure 5.4: Schematic diagram of acoustic scattering by a sphere.

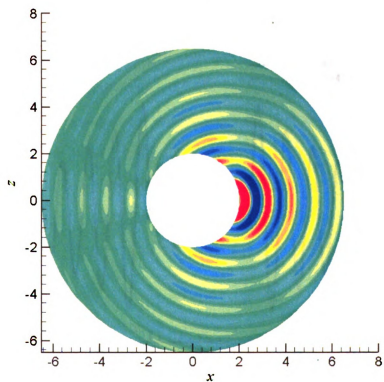
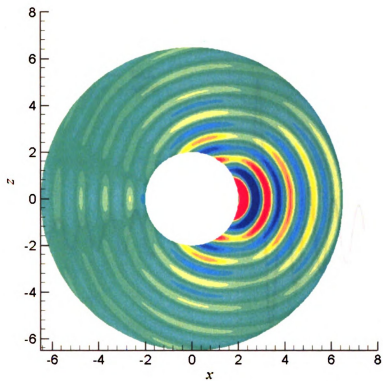


Figure 5.5: Instantaneous pressure contours of the sound scattering in the plane $y = 0$: CAA (top), AIBM (bottom).

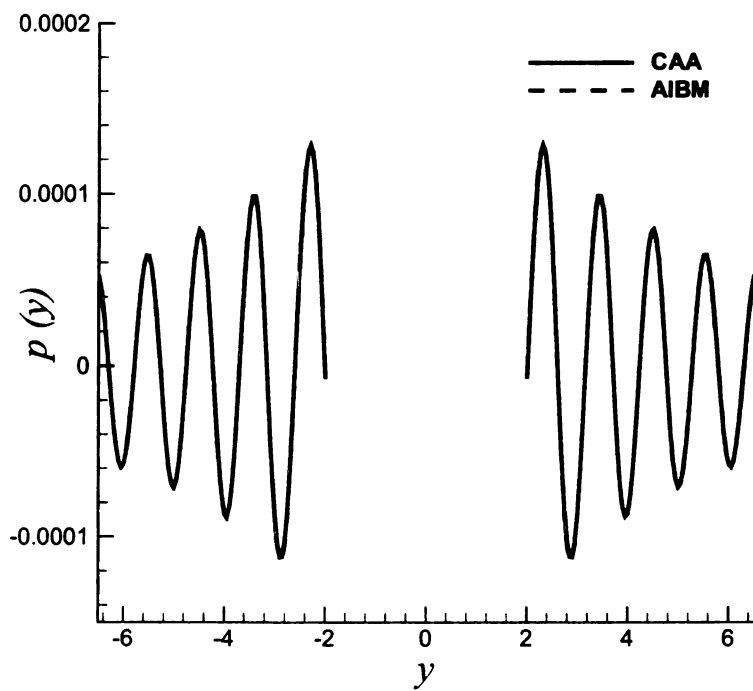
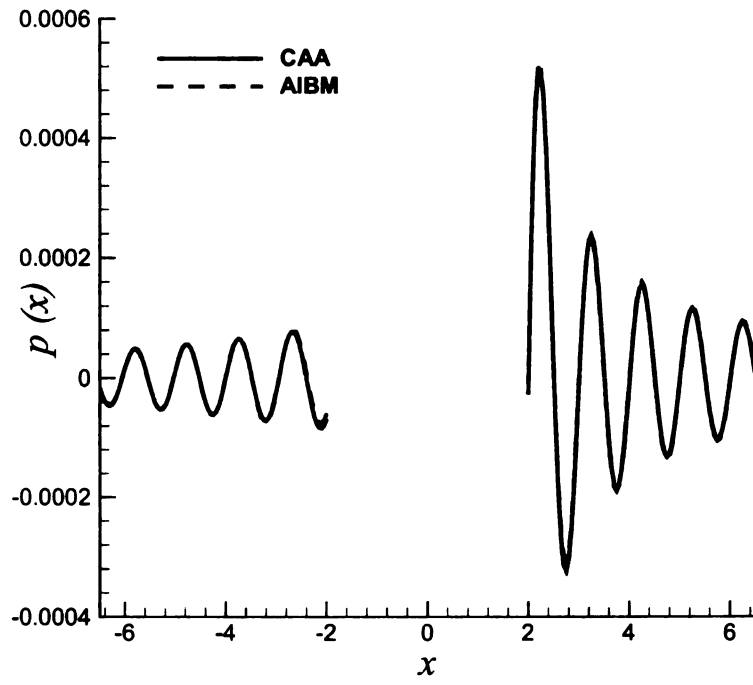


Figure 5.6: Comparisons of the predicted pressure solutions with the CAA solutions: along x-axis (top), along y-axis (bottom).

The predicted instantaneous pressure contours by AIBM are compared with the CAA solution in Figure 5.5 for the plane of $y = 0$. As it is noted from the figure, the predicted radiated acoustic field agrees very well with the CAA solutions outside a minimum sphere ($r = 2$) that encloses the acoustic sources. The proper size of a minimum sphere was discussed in our previous work [38]. Quantitative comparisons of the perturbation pressure along the x -axis and the y -axis are shown in Figure 5.6. Again an excellent agreement is achieved.

5.3.3 Acoustic Radiation from an Axisymmetric Duct Intake

Both CAA methods [19, 20, 59] and the FW-H integral method coupled with CAA methods [21] were used in the past for the prediction of acoustic propagation and radiation from an engine inlet. In the current study, an axisymmetric geometric model of a duct intake is considered with a uniform subsonic flow. Small acoustic perturbations are propagating upstream through the axisymmetric duct flow and radiating to the far field. A schematic of the duct intake configuration along with the Cartesian and the spherical coordinates and the domain of acoustic propagation and radiation is shown in Figure 5.7. The far field flow pressure, density, Mach number and the speed of sound are given as $P_\infty = 101.325kPa$, $\rho_\infty = 1.249kg/m^3$, $M_{a_\infty} = 0.19$ (in negative z -direction) and $c_\infty = 337m/s$, respectively. A single frequency sound source with the non-dimensional angular frequency of 14.2567 is considered. The azimuthal and radial modes used in the CAA calculations are $(m, n) = (2, 1), (3, 1)$ and $(4, 1)$.

The FW-H integral method is the most commonly used method for the far-field acoustic prediction. The method is based on the N-S equations and therefore is valid in both the near field and the far field. The AIBM, on the other hand, is based on the linearized Euler's equations and developed for the effective prediction of the far-field acoustic radiation. To show the capability and effectiveness of AIBM in a far-field prediction, the method is

coupled with CAA methods for the prediction of the acoustic radiation from the duct intake. The results of AIBM are compared to CAA solutions as well as the solution from the FW-H integral method. Since the acoustic wave is radiating in a 3D configuration, Farassat's 3D Formulation 1A [15] with the quadruple term neglected was used in the FW-H integral method. The FW-H surface is depicted in Figure 5.7, and the input surface used for AIBM is 1/9 of the FW-H surface, with θ from 0° to 40° . The input acoustic data is provided by CAA solutions, and the number of grid points used for the input is 57,960 for the FW-H method and 6,440 for the AIBM method. The input data consists of the unsteady pressure and its normal derivative to the input surface for AIBM, and the unsteady pressure and velocity for FW-H, respectively. Since the mean flow and the duct intake geometry are both axisymmetric, the simplified 2.5D formulation for AIBM is also used. The input data for 2.5D AIBM is given on a number of line segments in the plane of $\theta = 0$ (see Figure 5.7).

The acoustic pressure is predicted by AIBM, FW-H and 2.5D AIBM at 136 grid points in the range of $0 \leq x \leq 6.5\text{m}$ with $z = 6.5\text{m}$ and $y = 0$. The results from these methods are compared to the CAA solution in Figure 5.8. It is shown that the results from both AIBM and FW-H agree reasonably well with the CAA solution. The computation was performed on a personal computer of Pentium (R) 4CPU at 3.2GHz and memory of 1GB. In general, the computational time for AIBM is directly related to the number of input points and the number of coefficients, a_{nm} and b_{nm} . The CPU time will quadruple as the number of input points doubles and be increased by eight times if the number of coefficients doubles. For this single frequency radiation problem, the CPU times used for 3D AIBM and 2.5D AIBM are 5 minutes and 4 seconds, respectively. The total CPU time for FW-H is 16 hours. However, the time-domain formulation of FW-H is used and 64 time increments were considered in the period. The equivalent CPU time for FW-H is 15 minutes if the frequency-domain formulation of FW-H would be considered. Furthermore, in AIBM the acoustic pressure in a radiated field is calculated analytically after the coefficients of the

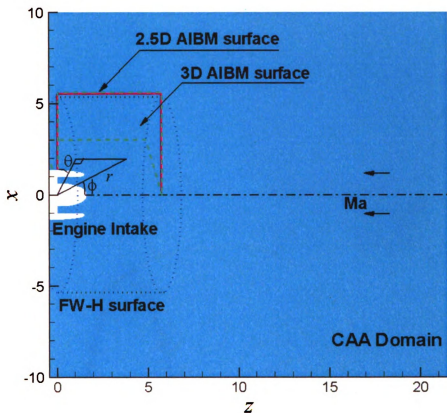


Figure 5.7: Schematic diagram of acoustic radiation through an axisymmetric duct intake.

basis functions are determined. In FW-H, on the other hand, the surface integration has to be carried out for each far-field location. Therefore, AIBM is much more efficient than FW-H and can lead to a significant CPU time reduction if the entire acoustic far field shown in Figure 7 is to be determined. Furthermore, it is noted from Figure 5.8 that the solution by 2.5D AIBM agrees very well with the CAA solution. The better agreement can be attributed to a relatively more complete input surface.

Since the problem considered here is axisymmetric, in the following studies, the radiated acoustic field is calculated based on the 2.5D AIBM formulation. The instantaneous pressure contours and the pressure amplitude contours obtained by 2.5D AIBM are compared to the CAA solutions in Figures 5.9 and 5.10 for the duct modes of (2, 1) and (3, 1), re-

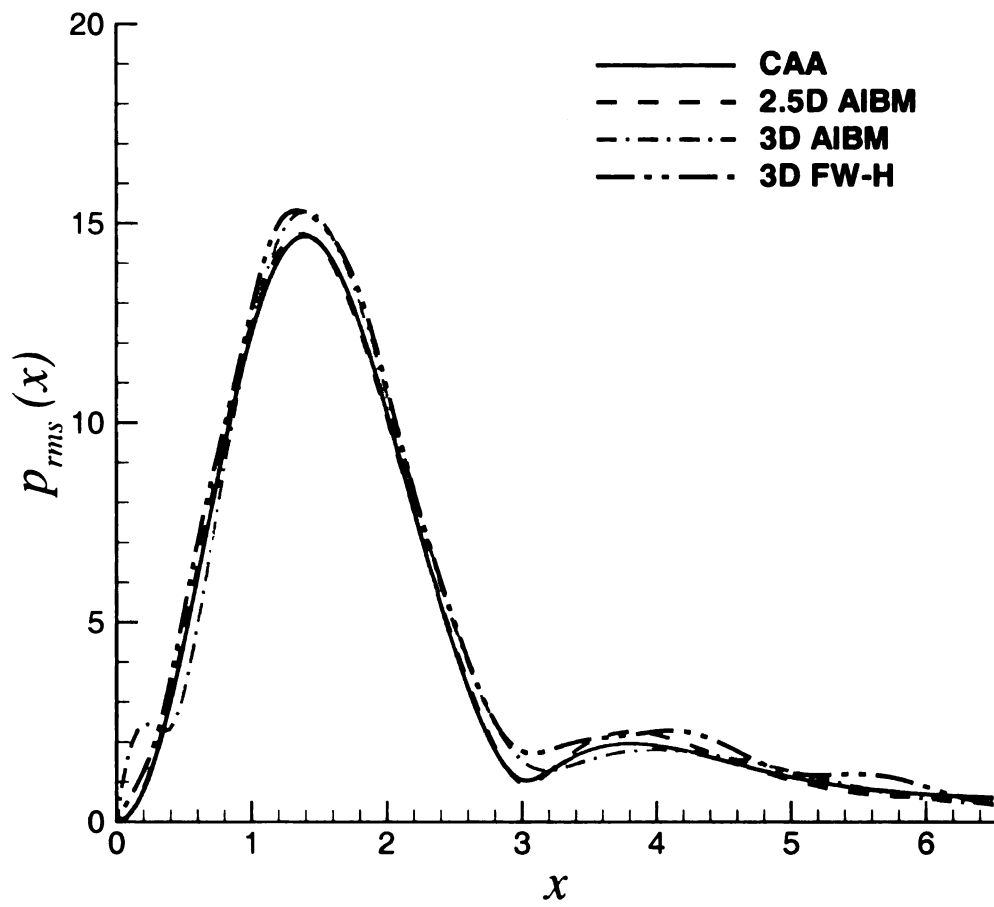


Figure 5.8: A comparison of the directivity along the x-direction with $z = 6.5\text{m}$ and $y = 0$ for the duct mode of $m=2$ and $n=1$.

spectively. In addition, the quantitative comparisons of the acoustic pressure for the (2, 1) mode and the directivity for the (3, 1) mode are given in Figures 5.11 and 5.12, respectively. The results shown in these figures clearly demonstrate the effectiveness of AIBM for the prediction of far-field acoustic radiation. It is noted that the solution inside and in the vicinity of intake although not valid was kept in the contour plots for convenience. In addition, the input acoustic data for AIBM should be given away from aerodynamic noise sources in order to guarantee the accuracy of the predicted acoustic solution in radiated fields. The reconstructed 3D instantaneous pressure contours by AIBM are compared to the CAA solution in Figure 5.13 for the duct mode of (4, 1). The capability and the overall effectiveness of AIBM for aeroacoustic applications are demonstrated by the example.

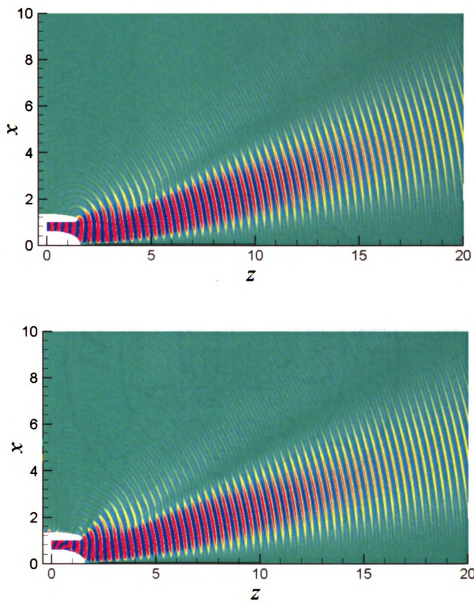


Figure 5.9: Instantaneous pressure contours in the plane $\theta = 0$ for the duct mode of $m=2$ and $n=1$: CAA (top), AIBM (bottom).

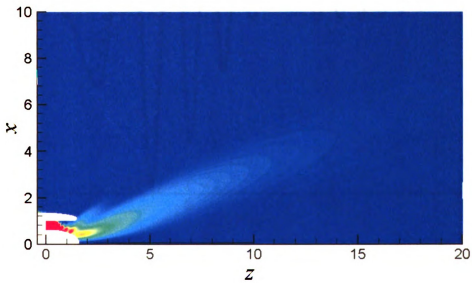
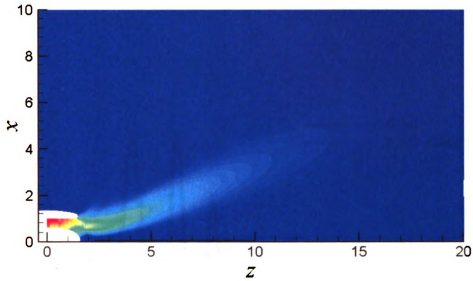


Figure 5.10: Pressure amplitude contours in the plane $\theta = 0$ for the duct mode of $m=3$ and $n=1$: CAA (top), AIBM (bottom).

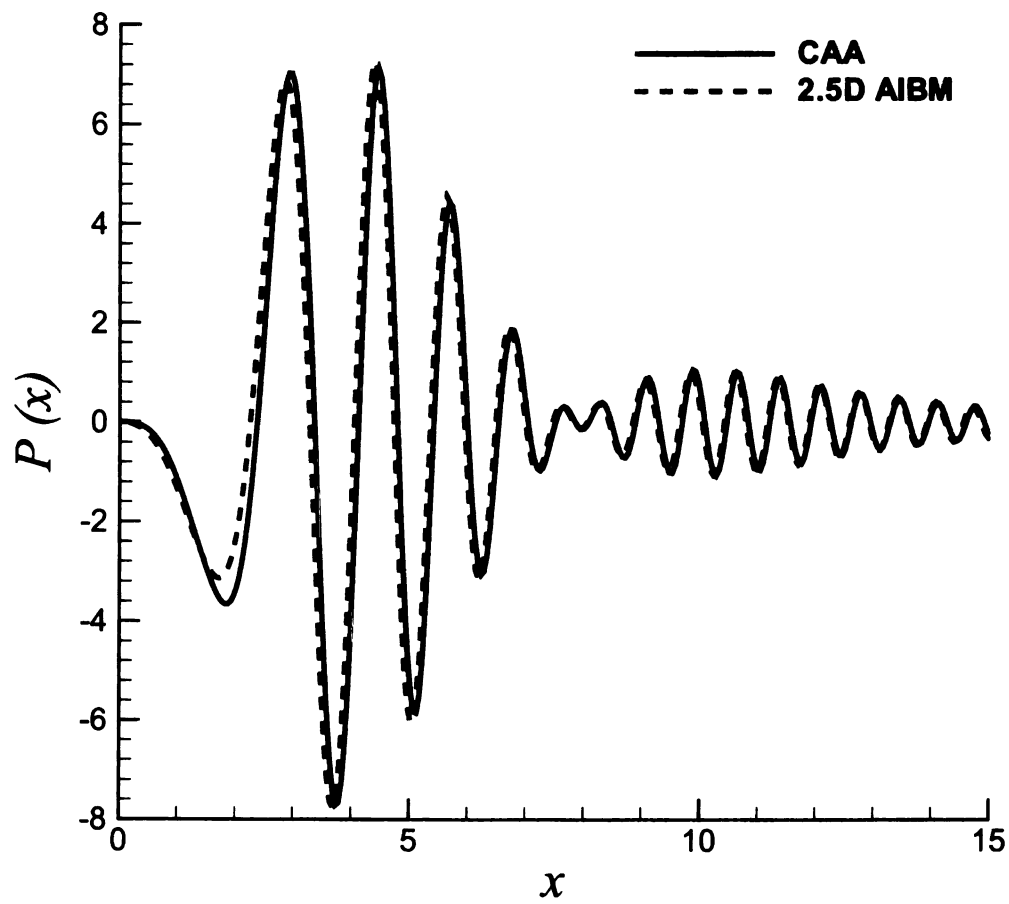


Figure 5.11: Comparison of the predicted pressure solution with the CAA solution at $z = 15m$ and $y = 0$ for the duct mode of $m = 2$ and $n = 1$.

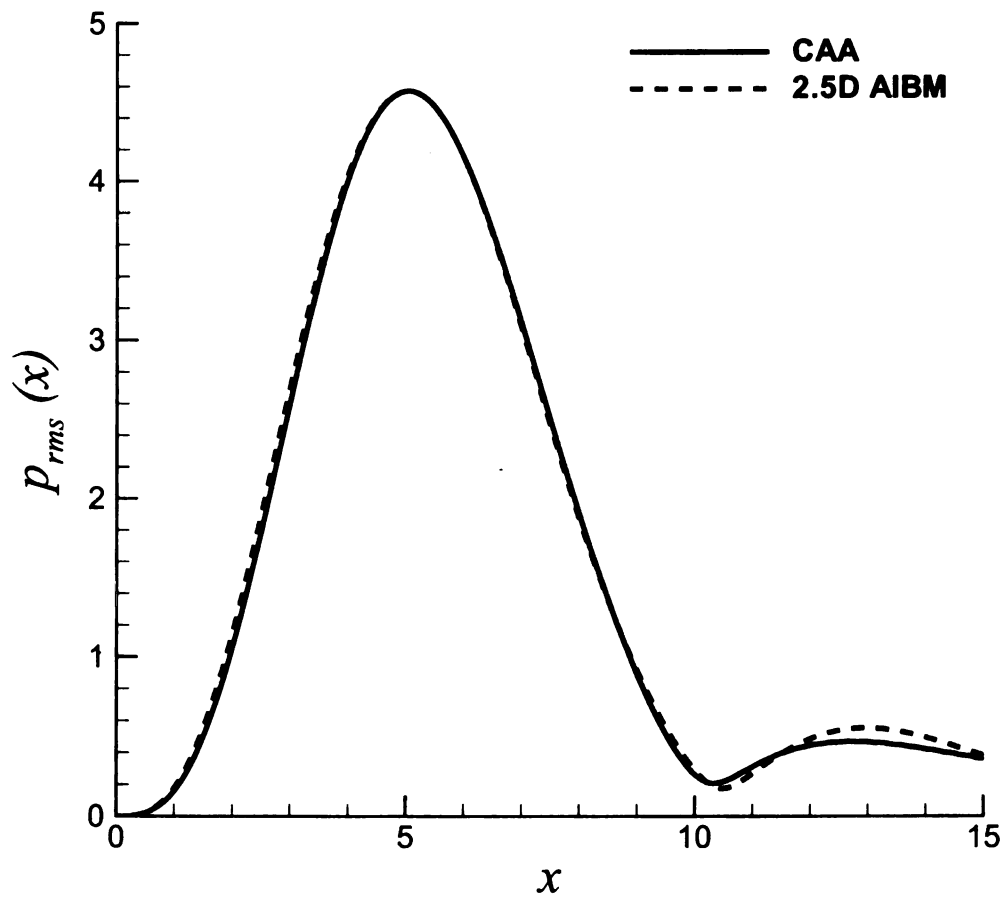


Figure 5.12: Comparison of the predicted directivity with the CAA solution at $z = 15\text{m}$ and $y = 0$ for the duct mode of $m = 3$ and $n = 1$.

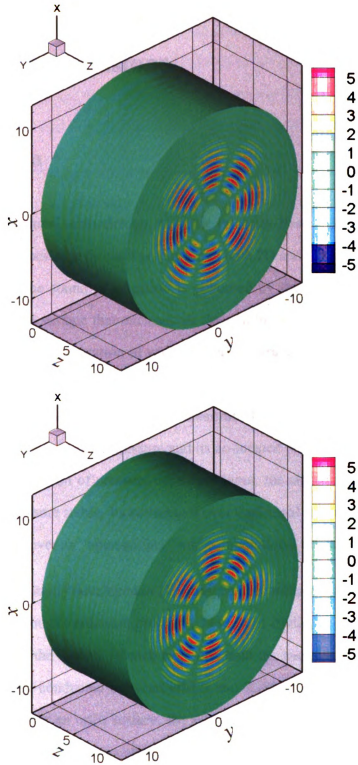


Figure 5.13: 3D reconstructed pressure contours for the duct mode of $m=4$ and $n=1$: CAA (top), AIBM (bottom).

Chapter 6 Conclusions

6.1 Conclusion

An advanced computational methodology, Acoustic Intensity-Based Method (AIBM), has been developed for the acoustic far-field prediction in both 2D and 3D configurations. This method assumes that the sound propagation is governed by the Helmholtz equation on and outside of a control surface that encloses all the nonlinear effects and noise sources. By employing the standard separation of variables, the general solution for the Helmholtz equation can be approximated by finite linear combinations of basis functions. The coefficients in the general solution are numerically determined by matching the assumed form of the solution to the input acoustic pressure and its co-located pressure derivative at measurements. With the addition of pressure derivative input, the solution of the Helmholtz equation is unique and more stable. Its advantages over traditional methods can be summarized as less input data over an “open surface” and computational efficiency.

The AIBM method is initially developed in 2D configuration without considering the mean flow effect. Several acoustic radiation problems have been studied to showcase the reliability and accuracy of the AIBM. In each example, both the qualitative and quantitative comparisons have been conducted between HELS and AIBM. When the input acoustic data is only provided over an open surface, the AIBM improves the accuracy, reliability, and consistency of reconstructed acoustic radiation pressure. The improvement, however, becomes less significant when the input segments are clustered. The AIBM is especially effective when random noises are added in the input acoustic data. The results indicate that the reconstruction of HELS method, i.e, without the addition of the pressure gradient to the

input acoustic data, starts to deteriorate even with 1% of random noise in the input from an open surface. The AIBM, on the other hand, can give reasonably accurate reconstructed acoustic pressure from the input acoustic data with up to 20% random noise. In addition, the capability and efficiency of the AIBM for multi-frequency (broadband) acoustic radiation have been demonstrated through a vortex/trailing edge interaction noise problem.

Accurate and efficient noise prediction plays a very important role in the aircraft design. The current far-field acoustic prediction technique, FW-H equation method, needs the input acoustic data on a closed surface, which encloses all the noise sources. Clearly, it is not possible for most aerospace application cases. Another important drawback of FW-H method is that the surface integration has to be carried out for each far-field location. Hence, it is very time consuming for FW-H method in a 3D acoustic simulation. Motivated by the strong need for an efficient open surface method in aircraft noise prediction, the AIBM is successfully extended for predicting sound propagations in a uniform flow. By coupling with the CFD/CAA numerical techniques, the extended AIBM has been verified in various acoustic propagation and radiation problems, such as flows around the airfoil, the scattering of a time-dependent acoustic source and the radiation of duct acoustic modes from an axisymmetric duct intake. The predicted acoustic fields by AIBM for all the cases agree very well with the respective CAA and the FW-H solutions. On the other hand, the AIBM only requires partial input data of FW-H and costs less computation time than FW-H. The overall effectiveness of the AIBM indicates that the method has the capability for the prediction of acoustic radiations encountered in engineering applications. In addition, relying on the advantage of computation efficiency, the AIBM has the potential to become a part of an integrated computational or design optimization procedure for evaluation of far-field acoustic propagations. Furthermore, the accurate prediction of the sound propagation and reflection of the scattering problem demonstrates that the AIBM can be used for both the near-field and far-field acoustic reconstruction and prediction. However the accuracy of the near-field reconstruction has been sacrificed to increase the reconstruction availability.

As pointed out by Ffowcs Williams (1993), the nature of aeroacoustics fields “permits many different, but equally exact, computational procedures for evaluation both the sound and its source field.” The results in the current study demonstrate that the AIBM could be used for the far-field sound prediction for aeroacoustic problems when a closed FW-H control surface is not possible. In general, the AIBM provides an effective alternative for the far-field acoustic prediction of practical aeroacoustic problems.

6.2 Suggestions for Future Work

AIBM method is a newly developed technique extended from HELS. We first published it in the AIAA/CEAS Aeroacoustics Conference in 2007, later in the Journal of the Acoustical Society of America in 2008. There could be several interesting possibilities in methodology extension and applications for the future study.

First, in dealing with practical problems, usually lots of measurements are needed as input data for AIBM. The inverse problem models are usually ill-posed with huge condition numbers. Also the Cauchy problem for the Helmholtz equation is unstable theoretically. The regularization technique could be considered and introduced to effectively solve the ill-posed problems with our AIBM method.

Second, the AIBM is initially defined as a far-field acoustic prediction method. The near-field (source region) prediction is also of interest by aircraft and automobile manufacturers. The AIBM has a potential for accurate near-field reconstruction with the additional basis functions.

Finally, there is currently no effective way to predict jet noise, which is one of the most challenging tasks in computational aeroacoustics. As our AIBM method was derived based on uniform flow assumption, a new model for dealing with a non-uniform flow is desired

for jet noise assumption. We hope to solve this real-world puzzle with further developments of the AIBM.

We believe the future of AIBM is promising with more exposure and examination of real industrial projects.

Appendix A: Associated Legendre Polynomial

The associated Legendre polynomial is derived in this section following the derivation of Numerical Recipes [63].

With $-1 \leq x \leq 1$, the associated Legendre polynomials are defined in terms of ordinary Legendre polynomials by

$$P_n^m(x) = (-1)^m (1-x^2)^{m/2} \frac{d^m}{dx^m} P_n(x) \quad (\text{A-1})$$

where

$$P_n(x) = P_n^0(x) = \frac{1}{2^n n!} \frac{d^n (x^2-1)^n}{dx^n} \quad (\text{A-2})$$

Introducing the stable recurrence on n presented in [63],

$$(n-m)P_n^m = x(2n-1)P_{n-1}^m - (n+m-1)P_{n-2}^m \quad (\text{A-3})$$

For the starting value, there is a closed-form expression,

$$P_m^m = (-1)^m (2m-1)!! (1-x^2)^{m/2} \quad (\text{A-4})$$

The notation $n!!$ denotes the product of all odd integers less than or equal to n . Using Equation A-3 with $n = m+1$, and setting $P_{m-1}^m = 0$, we can obtain

$$P_{m+1}^m = x(2m+1)P_m^m \quad (\text{A-5})$$

Equation A-4 and A-5 provide the two starting values required for Equation A-3 for general

n . The derivative of P_n^m with $m < n$ can be derived from its definition equation.

$$\frac{\partial P_n^m}{\partial x} = \frac{-mx}{1-x^2} P_n^m - \frac{1}{\sqrt{1-x^2}} P_n^{m+1} \quad (\text{A-6})$$

When $m = n$, the derivative is

$$\frac{\partial P_n^m}{\partial x} = \frac{-mx}{1-x^2} P_n^m \quad (\text{A-7})$$

Let

$$Q_n^m(x) = \frac{P_n^m(x)}{(1-x^2)^{m/2}} = (-1)^m \frac{d^m}{dx^m} P_n(x) \quad (\text{A-8})$$

Then the recurrence for $Q_n^m(x)$ is

$$(n-m)Q_n^m = x(2n-1)Q_{n-1}^m - (n+m-1)Q_{n-2}^m \quad (\text{A-9})$$

$$Q_m^m = (-1)^m (2m-1)!! \quad (\text{A-10})$$

$$Q_{m+1}^m = (-1)^m (2m+1)!! x \quad (\text{A-11})$$

The derivative for $Q_n^m(x)$ when $m < n$ is

$$\frac{\partial Q_n^m}{\partial x} = -Q_n^{m+1} \quad (\text{A-12})$$

When $m = n$, the derivative is

$$\frac{\partial Q_n^m}{\partial x} = 0 \quad (\text{A-13})$$

Appendix B: Spherical Hankel Function

The 0-th order and first order Spherical Hankel functions are [63]

$$G_0(r) = \frac{1}{r} \sqrt{\frac{2}{\pi}} \exp \left[-i \left(r - \frac{\pi}{2} \right) \right] \quad (\text{B-1})$$

$$G_1(r) = \frac{1}{r} \sqrt{\frac{2}{\pi}} \exp[-i(r - \pi)] \left(1 - \frac{i}{r} \right) \quad (\text{B-2})$$

Employing the recurrence formulation, n-th order can be obtained based on the 0-th and first order formulations.

$$G_n(r) = \frac{2n - 1}{r} G_{n-1} - G_{n-2} \quad (\text{B-3})$$

The corresponding derivative formulations for 0-th order is just simply derived from $G_0(r)$.

And the higher orders are obtained by recurrence relations.

$$G'_0(r) = -G_0 \left(\frac{1}{r} + i \right) \quad (\text{B-4})$$

$$G'_n(r) = -\frac{n + 1}{r} G_n + G_{n-1} \quad (\text{B-5})$$

Bibliography

- [1] "Federal Aviation Regulations Part 36 Noise Standards: Aircraft Type and Airworthiness Certification," see <http://www.airweb.faa.gov/>.
- [2] "Noise Standards for Aircraft Type Certification (Modifications to FAR Part 36)," U. S. Environmental Protection Agency, Washington D. C., EPA 550/9-76-013, 197, 1994.
- [3] Gillian, R. E., Brown, C. G., Bartlett, R. W. and Baucom, P. H., "ANOPP Programmers' Reference Manual for the Executive System," *NASA Technical Memorandum*, NASA TM X-74029, 1977.
- [4] "Making Future Commercial Aircraft Quieter," NASA Facts, FS-1997-07-003-LeRC, 1997.
- [5] Fisher, M. J. and Self, R. H. "Aeroacoustics Research in Europe: The CEAS-ASC Report on 2001 Highlights," *Journal of Sound and Vibration*, Vol. 258, No. 1, 2002, pp. 1-30.
- [6] Lighthill, M. J., "On Sound Generated Aerodynamically, I: General Theory," *Proceeding of the Royal Society*, Vol. A211, No. 1107, 1952, pp. 564-587.
- [7] From Wikipedia, <http://en.wikipedia.org/wiki/Directnumericalsimulation>.
- [8] Wang, M., Freund, J. B. and Lele, S. K., "Computational Prediction of Flow-Generated Sound," *Annu. Rev. Fluid Mech.*, Vol. 38, 2006, pp. 483-512.
- [9] Sinha, N., Dash, S. M., Chidambaram, N. and Findlay, D., "A Perspective on the Simulation of Cavity Aeroacoustics," *AIAA Paper* 1998-0286.
- [10] Riestra, S. W. and Hirschberg, A., "An Introduction to Acoustics," *IWDE Report 01-03*, (extended and revised version of IWDE 92-06), May 2001.
- [11] Curle, N., "The Influence of solid boundaries upon aerodynamic sound," *Proceeding of the Royal Society*, Vol. A23, 1955, pp. 505-514.
- [12] Ffowcs Williams, J. E. and Hawking, D. L., "Sound Generated by Turbulence and Surfaces in Arbitrary Motion," *Philosophical Transactions of the Royal Society*, Vol. A264, No. 1151, 1969, pp. 321-342.
- [13] Farassat, F., "Linear Acoustic Formulas for Calculation of Rotating Blade Noise," *AIAA Journal*, Vol. 19, 1981, pp. 1122-1130.
- [14] Farassat, F. and Succi, G. P., "The Prediction of Helicopter Discrete Frequency Noise," *Vertica*, Vol. 7, No. 4, 1983, pp. 309-320.

- [15] Farassat, F., "Derivation of Formulations 1 and 1A of Farassat," *NASA Technical Report*, NASA/TM-2007-214853, March 2007.
- [16] Farassat, F., and Myers, M. K., "Extension of Kirchhoff's Formula to Radiation from Moving Surfaces," *Journal of Sound and Vibration*, Vol. 123, No. 3, 1988, pp. 451-461.
- [17] Grace, S. P. and Atassi, H. M., "Inverse Aeroacoustic Problem for a Streamlined Body, Part 1: Basic Formulation," *AIAA Journal*, Vol. 34, No. 11, 1996, pp. 2233-2240.
- [18] Grace, S. P. and Atassi, H. M., "Inverse Aeroacoustic Problem for a Streamlined Body, Part 2: Accuracy of Solutions," *AIAA Journal*, Vol. 34, No. 11, 1996, pp. 2241-2246.
- [19] Li, X. D. and Zhou, S., "Spatial transformation of the discrete sound field from a propeller," *AIAA Journal*, Vol. 34, No. 6, 1996, pp. 1097-1102.
- [20] Luo, J. and Li. X. D., "An Inverse Aeroacoustic Problem on Rotor Wake Stator Interaction," *Journal of Sound and Vibration*, Vol. 254, No. 2, 2002, pp. 219-229.
- [21] Li, X. D., Luo J. and Yu, C., "An Inverse Aeroacoustic Problem on Gust/Cascade Interaction," *AIAA Paper* 2001-2122.
- [22] Gerrard, A. , Berry, A. and Masson, P., "Control of Tonal Noise From Subsonic Axial Fan. Part 1: Reconstruction of Aeroacoustic Sources From Far-field Sound Pressure," *Journal of Sound and Vibration*, Vol. 288, No. 4-5, 2005, pp. 1049-1075.
- [23] Holland, K. R. and Nelson, P. A., "Applying Inverse Methods to Distributed Aeroacoustic Sources," *AIAA Paper* 2005-3000.
- [24] Nelson, P. A. and Yoon, S. H., "Estimation of Acoustic Source Strength by Inverse Methods: Part I, Conditioning of The Inverse Problem," *Journal of Sound and Vibration*, Vol. 233, No. 4, 2000, pp. 643-668.
- [25] Williams, E. G. and Maynard, J. D., "Holographic Imaging without the Wavelength Resolution Limit," *Physical Review Letters*, Vol. 45, 1980, pp. 554-557.
- [26] Maynard, J. D., Williams, E. G. and Lee, Y., "Nearfield Acoustic Holography: I. Theory of Generalized Holography and the Development of NAH," *J. Acoust. Soc. Am.*, Vol. 78, 1985, pp. 1395-1413.
- [27] Gardner, B. K. and Bernhard, R. J., "A Noise Source Identification Technique Using an Inverse Helmholtz Integral Equation Method," *Trans. ASME, J. Vib., Acoust., Stress, Reliab. Des.*, Vol. 110, 1988, pp. 84-90.
- [28] Bai, M. R., "Application of BEM (boundary element method) - Based Acoustic Holography to Radiation Analysis of Sound Sources with Arbitrarily Shaped Geometries," *J. Acoust. Soc. Am.*, Vol. 92, 1992, 533-549.

- [29] Kim, B. K. and Ih, J. G., "On the Reconstruction of the Vibro-acoustic Field over the Surface Enclosing an Interior Space Using the Boundary Element Method," *J. Acoust. Soc. Am.*, Vol. 100, 1996, pp. 3003-3016.
- [30] Williams, E. G., Houston, B. H., Herdic, P. C., Raveendra, S. T. and Gardner, B., "Interior Near-field Acoustical Holography in Flight," *J. Acoust. Soc. Am.*, Vol. 108, 2000, pp. 1451-1463.
- [31] Zhang, Z., Vlahopoulos, N., Raveendra, S. T., Allen, T. and Zhang, K. Y., "A Computational Acoustic Field Reconstruction Process Based on an Indirect Boundary Element Formulation," *J. Acoust. Soc. Am.*, Vol. 108, 2000, pp. 2167-2178.
- [32] Wang, Z. and Wu, S. F., "Helmholtz Equation Least-Squares (HELs) method for reconstructing the acoustic pressure field," *J. Acoust. Soc. Am.*, Vol. 102, 1997, pp. 2020-2032.
- [33] Wu, S. F., "On Reconstruction of Acoustic Pressure Fields by Using HELs Method," *J. Acoust. Soc. Am.*, Vol. 107, 2000, pp. 2511-2522.
- [34] Isakov, V. and Wu, S. F., "On Theory and Application of the Helmholtz Equation Least Squares Method in Inverse Acoustics," *Inverse Problems*, Vol. 18, 2002, pp. 1147-1159.
- [35] Jerison, D. and Kenig, C. E., "Unique Continuation and Absence of Positive Eigenvalue for Schrodinger Operators," *Analysis of Math*, Vol.121, No. 3, 1985, pp. 463-494.
- [36] Hormander, L., "Uniqueness Theorems for Second Order Elliptic Differential Equations," *Comm. in P.D.E*, Vol. 8, No. 1, 1983, pp. 21-64.
- [37] Schechter, M. and Simon, B., "Unique Continuation for Schrodinger Operators with Unbounded Potential," *J. Math. Anal. Appl.*, Vol. 77, 1980, pp. 482-492.
- [38] Yu, C., Zhou, Z. F. and Zhuang, M., "An Acoustic Intensity-Based Method for Reconstruction of Radiated Fields," *J. Acousti. Soc. Am.*, Vol. 123. No. 4, 2008, pp.1892-1901.
- [39] Yu, C., Zhou, Z. and Zhuang, M., "Improved Inverse Acoustic Methods through Advances in Acoustic Intensity Measurement Techniques," *AIAA Paper* 2007-3563.
- [40] Yu, C., Zhou, Z. and Zhuang, M., "Coupling of Acoustic Intensity-Based Method with Near-field CFD/CAA Techniques for Far-field Sound Radiation Predictions," submitted for publication to *J. Acousti. Soc. Am.*, 2008.
- [41] Yu, C., Zhou, Z., Zhuang, M., Li, X. D. and Thiele, F., "3D Acoustic Intensity-Based Method and Its CAA Applications," *AIAA Paper* 2008-3053.
- [42] Yu, C., Zhou, Z., Zhuang, M., Li, X. D. and Thiele, F., "An Effective Far-field Acoustic Prediction Method and Its CAA Applications," accepted for publication on *AIAA Journal*, 2008.

- [43] Yu, C., Zhou, Z., Zhuang, M., "On a Hybrid Technique of Acoustic Intensity-Based Method and CFD/CAA," *TU-Berlin Technical Report*, IP-10022152, October, 2008.
- [44] Goldstein, M., "Aeroacoustics," *McGraw-Hill Book Company*, 1976.
- [45] Jacobsen, F. and de Bree, H. E., "A comparison of two different sound intensity measurement principles," *J. Acoust. Soc. Am.*, Vol. 118, 2005, pp. 1510-1517.
- [46] Isakov, V., "Inverse problems for partial differential equations," *Birkhaeuser Publishing Ltd.*, 2006.
- [47] Bowman, F., "Introduction to Bessel Functions," *Dover Publications Inc.*, New York, 1958.
- [48] Muller, C. "Spherical Harmonics," *Lectures Notes in Mathematics No.17*, *Springer-Verlag*, 1966.
- [49] Ffowcs Williams, J. E. and Hall, L. H., "Aerodynamic sound generation by turbulent flow in the vicinity of a scattering half plane," *J. Fluid Mech.*, Vol. 40, No. 2, 1970, pp. 657-670.
- [50] Crighton, D. G., "Radiation from vortex filament motion near a half plane," *J. Fluid Mech.*, Vol. 51, No. 2, 1972, pp. 357-362.
- [51] Lockard, D. P., "An Efficient, Two-Dimensional Implementation of The Ffowcs Williams and Hawkins Equation," *J. Sound and Vibration*, Vol. 229, No.4, 2000, pp. 897-911.
- [52] Bowman, F., "Introduction to Bessel Functions," *Dover Publications Inc. New York*, 1958.
- [53] Dowling, A. P. and Ffowcs Williams, J. E., "Sound and Sources of Sound," *Chichester, Sussex: Ellis Horwood*, 1983.
- [54] Greschner, B., Yu, C., Zheng, S., Zhuang, M., Wang, Z. J. and Thiele, F., "Knowledge Based Airfoil Aerodynamic and Aeroacoustic Design," *AIAA Paper 2005-2968*.
- [55] Lockard, D. P., "A Comparison of Ffowcs Williams-Hawkin solvers for Airframe Noise Applications," *AIAA Paper 2002-2580*.
- [56] Zhuang, M. and Chen, R. F., "Applications of High-Order Optimized Upwind Schemes for Computational Aeroacoustics," *AIAA Journal*, Vol. 40, No. 3, 2002, pp. 443-449.
- [57] Chen, R. F. and Zhuang, M., "Application of Dispersion-Relation-Preserving Scheme to the Computation of Acoustic Scattering in Benchmark Problems," *ICASE/LaRC 2nd Workshop on Benchmark Problems in Computational Aeroacoustics*, Tallahassee, FL., Nov., 1996.

- [58] Morris, P. J., "Scattering of Sound from a Spatially Distributed, Spherically Symmetric Source by a Sphere," *J. Acoust. Soc. Am.*, Vol. 98, No. 6, 1995, pp. 3536-3539.
- [59] Özyörük, Y. and Long, L. N., "Computation of Sound Radiating from Engine Inlet," *AIAA Journal*, Vol. 34, No. 5, 1996, pp. 894-901.
- [60] Li, X. D., Schemel, C., Michel, U. and Thiele, F. "Azimuthal Sound Mode Propagation in Axisymmetric Duct Flows," *AIAA Journal*, Vol. 42, No. 10, 2004, pp. 2019-2027.
- [61] Li, X. D., Schoenwald, N., Yan, J. and Thiele, F., "A Numerical Study on The Acoustic Radiation from a Scarfed Intake," *AIAA Paper* 2003-3245.
- [62] Li, X. D., Duan, C. and Yu, C., "On The Matching Technology Between The 3-D FW-H Equation and CAA Numerical Simulations," *Journal of Engineering Thermophysics* (in Chinese), Vol. 26, No. 1, 2005, pp.51-54.
- [63] Press, W. H., Teukolsky, S. A., Vetterling, W. T. and Flannery, B. P., "Numerical Recipes in Fortran 77: The Art of Scientific Computing (Vol 1 of Fortran Numerical Recipes) (Second Edition)", *Press Syndicate of the University of Cambridge*, 2001.
- [64] Anderson, D. A., Tannehill, J. C. and Pletcher, R. H., "Computational Fluid Mechanics and Heat Transfer," *Hemisphere Publishing Corporation*, 1984.

MICHIGAN STATE UNIVERSITY LIBRARIES



3 1293 03062 4450